Potential of the IceTop Enhancement with a Scintillation Detector Array

Zur Erlangung des akademischen Grades einer
Doktorin der Naturwissenschaften
von der KIT-Fakultät für Physik
des Karlsruher Instituts für Technologie (KIT)

genehmigte
Dissertation

von Agnieszka Stanisława Leszczyńska (M.Sc.)
aus Gdynia, Polen

Tag der mündlichen Prüfung:	29.05.2020
Referent:	Prof. Dr. Ralph Engel
Korreferent:	Prof. Dr. Florian Bernlochner
Betreuer:	Dr. Andreas Haungs

The latex template for this thesis is based on: https://www.overleaf.com/latex/templates/caltech-thesis-latex-template-with-logo/kgwqvkbfkwmx. The template is used and modified under Creative Commons BY 4.0 (https://creativecommons.org/licenses/by/4.0/).

ABSTRACT

Potential of the IceTop Enhancement with a Scintillation Detector Array

The energy spectrum of cosmic rays manifests features that prompt studies on their relation to the astrophysical origin of cosmic rays. The sharp steepening around PeV is believed to emerge from a leakage of primary protons out of the Galaxy and/or limitations of the acceleration power of the Galactic sources. To sustain the measured flux at higher energies, another population of astrophysical objects is required, preferred at extragalactic distances. However, it is unclear at which energies extragalactic contribution becomes the dominant cosmic-ray accelerator. Indications can be provided by the measurement of individual primary mass spectra, revealing signatures of different astrophysical scenarios.

The necessary indirect method of cosmic-ray observations at these energies, via extensive air showers, makes it challenging to precisely infer the mass of the individual cosmic-ray primaries. Large uncertainties do not allow for constraining the astrophysical hypothesis efficiently. However, the approach of hybrid measurements with multiple detection channels is improving the sensitivity to different air-shower components and hence, to the determination of the elemental composition as well as the absolute energy of the cosmic rays.

The IceTop experiment, the surface array of the IceCube Neutrino Observatory, measures extensive air showers covering this energy region. Due to its limitations, emerging from the environmental conditions at the South Pole, an enhancement with scintillation detectors is planned.

A detailed simulation study of the performance of this extension, as well as the fundaments of the analysis pipeline are essential for an evaluation of its scientific capabilities. In the scope of this dissertation, scintillator array simulations have been developed and incorporated in the existing IceTop framework. The characteristics of the single detector as well as response of the array to air showers were broadly studied and used for an optimisation of the layout of the detector array. Further, the basis for the future data analysis was established, including the reconstruction procedures adjusted to the particular design. This allowed for an assessment of the reconstruction performance of the fundamental air-shower observables, like direction and shower core location. The scintillator array alone will be able to determine the shower core with an accuracy of 5 m and the direction with an accuracy of less than 0.5° at 10 PeV. The cosmic-ray energy can be estimated with a reference distance, which was found to be nearly independent on the primary mass at high energies. Studies of the dependence of the reconstructed parameters on the primary mass were performed, including γ-ray induced air showers. Combining specific parameters from IceTop and scintillator reconstructions, which found to be sensitive to the cosmic ray's mass, results in an improved discrimination power of light and heavy primaries. They are supposed to be included in the future composition analysis in the primary energy range of 1–100 PeV.

The obtained results have shown that a scintillator array enhancing the ice-Cherenkov tanks of IceTop turns the IceCube surface array into a hybrid detector to observe extensive air showers, boosting the quality and accuracy of the cosmic ray measurements. Moreover, it will enable lowering the energy range by doubling the current sensitive area allowing for a more comprehensive investigation of the energy range of the knee feature in the energy spectrum of primary cosmic rays. The estimated accuracies of the developed analysis chain give confidence that current open questions in the mass composition around the knee and the transition region from Galactic to extragalactic sources of cosmic rays will be addressed.

ZUSAMMENFASSUNG

Potenzial der IceTop-Erweiterung mit einem Szintillations-Detektor-Array

Das Energiespektrum der kosmischen Strahlung weist Eigenschaften auf, die Rückschlüsse auf den astrophysikalischen Ursprung der kosmischen Strahlung erwarten lassen. Es wird vermutet, dass das Knie im Spektrum im PeV Energiebereich durch den Austritt primärer Protonen aus unserer Galaxis und/oder durch die Grenzen der Beschleunigung der galaktischen Quellen hervorgerufen wird. Um den gemessenen Fluss bei höheren Energien zu erklären, wird eine andere Population astrophysikalischer Objekte als Quelle der kosmischen Strahlung benötigt, vorzugsweise in extragalaktischer Entfernung. Es ist jedoch unklar, bei welchen Energien extragalaktische Quellen beginnen das Spektrum der kosmischen Strahlung zu dominieren. Hinweise können durch die Messung der einzelnen primären Massenspektren gegeben werden, die Signaturen verschiedener astrophysikalischer Szenarien reflektieren.

Die bei diesen Energien notwendige indirekte Beobachtungsmethode der kosmischen Strahlung, mittels ausgedehnter Luftschauer, macht es schwierig die Masse der kosmischen Strahlung zu bestimmen. Durch große Unsicherheiten in der Rekonstruktion ist es nicht möglich, bestimmte astrophysikalische Hypothesen effizient auszuschließen. Der Ansatz von Hybridmessungen, indem mehrere Komponenten des Luftschauers parallel gemessen werden, erhöht jedoch die Sensitivität auf Unterschiede in der Luftschauerentwicklung und dadurch auch die Sensitivität auf die Messung der Massenkomposition und der absoluten Energie.

Das IceTop-Experiment, das Oberflächendetektorarray des IceCube Neutrino-Observatoriums, misst ausgedehnte Luftschauer, wobei der Energiebereich von PeV bis EeV abgedeckt wird. Aufgrund der Limitation der Performanz des Arrays, die durch die Umweltbedingungen am Südpol gegeben sind, ist eine Erweiterung mit Szintillationsdetektoren geplant.

Um das wissenschaftliche Potential dieser Erweiterung zu beurteilen, ist es unerlässlich das Verhalten mittels detaillierter Simulationen zu studieren und die Grundlagen der Analyseroutinen festzulegen. Im Rahmen dieser Dissertation wurden die Simulations-Routinen für das Szintillations-Detektor-Array entwickelt und in das existierende IceTop-Programmiergerüst integriert. Die Charakteristiken eines einzelnen Detektors sowie die Antwort des gesamten Arrays auf einen Luftschauer wurden umfassend untersucht und genutzt, um das Layout des Detektorarrays zu optimieren. Zusätzlich wurde die Basis für die zukünftige Datenanalyse geschaffen, einschließlich der auf dieses spezielle Design angepassten Rekonstruktionsprozedur. Dies erlaubt eine Beurteilung der Rekonstruktionsfähigkeiten fundamentaler Luftschauerobservablen wie Einfallsrichtung und Position des Schauerkerns. Das Szintillatorarray wird in der Lage sein, die Position des Schauerkerns mit einer Genauigkeit von 5 m und die Einfallsrichtung mit einer Genauigkeit von weniger als

0.5° bei 10 PeV zu bestimmen. Die Energie der kosmischen Strahlung kann mittels einer Referenzdistanz abgeschätzt werden, wobei gezeigt werden konnte, dass diese eine geringe Abhängigkeit von der Masse des Primärteilchens besitzt. Weiterhin wurden detaillierte Studien über die Abhängigkeit der erhaltenen Parameter von der Art des Primärteilchens durchgeführt, wobei auch γ-induzierte Luftschauer miteinbezogen wurden. Die Kombination spezifischer Parameter des IceTop- und des Szintillatorarrays, die sensitiv auf die Masse der kosmischen Strahlung sind, resultiert in ein verbessertes Diskriminierungsvermögen. Diese Parameter sollen somit in der zukünftigen Analyse der Elementzusammensetzung der kosmischen Strahlung in dem relevantem Energiebereich von 1- 100 PeV einbezogen werden.

Die in dieser Arbeit erzielten Ergebnisse zeigen, dass die zusätzliche Beobachtungsmethode für Luftschauer mit Szintillatoren die Messungen kosmischer Strahlung verbessert, insbesondere durch hybriden Schauernachweis mit verschiedenen Detektortypen. Außerdem verringert sich die Energieschwelle durch Verdoppelung der sensitiven Fläche, wodurch eine umfangreichere Untersuchung des Knies im Spektrum der kosmischen Strahlung möglich wird. Die bestimmten Genauigkeiten der entwickelten Analyse stimmen zuversichtlich, dass die offenen Fragen bezüglich der Massenkomposition in der Knie- und Übergangsregion von galaktischem zu extragalaktischem Ursprung der kosmischen Strahlung mit diesem neuen Detektor beantwortet werden können.

TABLE OF CONTENTS

INTRODUCTION

After the explosive death of a star, the remaining ejecta propagate with high velocity creating a shock wave. Such a violent environment lasts for hundreds, thousands of years, accelerating particles and nuclei to very high energies [1]. After escaping the accelerator some of these cosmic rays reach Earth's atmosphere, creating a spectacular avalanche of particles. Even though scientists developed large experiments and novel methods to relate these cascades with the properties of the incoming cosmic rays, their exact origin leaves room for speculations. A more clear picture only will be available by a better understanding of the processes in these distant accelerators.

Already in the early 1930's, scientists established the first calculations making a link between supernovae and observed intensity of high-energy cosmic rays [2]. Many attempts, theoretical and experimental, have been made to verify this hypothesis. Today, it is commonly accepted that at least up to 100 TeV primary energy, supernovae constitute the main galactic source of cosmic rays [3].

However, an order of magnitude above this energy a very distinct feature has been observed in the cosmic-ray energy spectrum. The sudden drop of the flux, called "the knee", observed already by many different experiments [4, 5, 6], suggests a change in the source object, in the acceleration process or in details of the propagation of the cosmic rays through our Galaxy [7, 8]. A model, assuming dependence of the acceleration and propagation processes in the Galactic magnetic fields, indicates that such feature could be connected to the maximum rigidity of a given cosmic ray type [9]. Experimental efforts have been made to infer the spectral changes with respect to the cosmic ray mass. The KASCADE experiment has shown a significant change in the spectrum for light and heavy elemental groups exactly around the knee [10]. However, the large uncertainties of these measurements require deeper studies in this energy range to disentangle the mass groups with the highest possible accuracy. Moreover, despite big challenges originating from the lack of full understanding of the Galactic magnetic fields, an anisotropy of the cosmic rays in the PeV energy region for different elemental groups would constrain the models.

Going even higher in energy raises more questions. Before reaching the ultra high energies, where anisotropy of arrival direction points outside our Galaxy [11], from PeV to EeV region another source of cosmic rays is needed to sustain the observed flux [12]. The understanding of this transition region is essential to obtain a consistent picture linking the different observed features of cosmic ray spectra of individual masses.

The main challenge for the air shower experiments to measure the cosmic ray composition lies in the precise determination of the cosmic ray mass on event-by-event basis. Large uncertainties, emerging from different models of hadronic interactions needed to interpret the distributions of measured signals as well as determination of the primary energy, result in limited constraints in the astrophysical models. In addition, the intrinsic fluctuations of the air showers diminishes the precision further.

To address these urgent challenges the air-shower observatories undergo broad upgrades [13, 14, 15]. In particular, the surface array of Cherenkov tanks, IceTop, which is the surface component of the IceCube Neutrino Observatory at the South Pole [16], will undergo such an upgrade. This unique location is relevant not only for the neutrino observations but also gives a great advantage for cosmic ray measurements. The high altitude at the South Pole brings the observation level higher, i.e closer to the shower maximum, where observed distributions provide a better insight into the cascade development. Additionally, the large volume of instrumented ice offers a possibility to detect high energy muons coming from the central region of a cascade.

However, due to the Antarctic environment and associated continuous accumulation of snow, signals detected by IceTop are attenuated [17]. This is the main source of the uncertainty in the air shower measurements and limits the possibility for a precise determination of the cosmic ray mass on event-by-event basis. These constraints will be overcome with the enhanced instrument. The scintillation detector response and geometry differs from the Cherenkov tank, giving a complementary sensitivity to the air shower components.

In this work the scientific capabilities of the foreseen enhancement of the IceTop with the scintillation detectors is obtained based on analysis of comprehensive simulations. The proper understanding of the new detector response is essential in context of the sensitivity of the air shower array to the variation of the air shower development due to different cosmic rays masses. After laying the foundations of the classical procedure for the reconstruction of the cosmic ray observables and description of the main characteristic distributions, the key factors determining the scientific capabilities of the new array are presented.

Chapter 1

HIGH-ENERGY COSMIC RAY PHYSICS

1.1 Milestones in cosmic ray research

Deep interests in the extraterrestrial environments have always accompanied scientists. Despite the long journey of discoveries, breakthrough observations and better theoretical understanding of the Universe, still many questions remain open. To pursue the next avenues, different branches of science merged into astroparticle physics. This research field was born in the beginning of the 20th century, during the first observations of, what was at that time concluded to be, cosmic radiation. The observations of Domenico Pacini [18] and later Victor Hess [19], among others, concluded an increase in the measured radiation intensity with increasing altitude. This was a clear indication of the extraterrestrial nature of this emission. After centuries of optical observations, the possibility to detect particles coming from space was a driving force to the rapid development of technology, theoretical explanations of the nature of these cosmic messengers and even to the birth of particle physics.

The next decades brought conclusive evidence about the nature of these particles. Jacob Clay pursued numerous measurements at very different locations, observing lower intensity [20] and higher penetration power of cosmic rays closer to the Earth's equator [21]. It has been explained by the distribution of the geomagnetic field lines, which prevent low-energy particles from entering the atmosphere. Nowadays, it is well established that cosmic rays are charged and undergo deflections in the interstellar magnetic fields. It is remarkable that this simple property is the main reason hiding their astrophysical origin.

In the following years, the attempts to determine the sign of the charge were made [22]. It has been shown by, inter alia, Thomas Johnson in 1933 [23], that cosmic-ray intensity is higher from the west than from the east due to their positive charge, what is know as the East-West effect. Early balloon experiments with coincidence counters provided indications that cosmic rays interacting at high altitudes are mainly protons [24].

Simultaneously, the counters developed by Hans Geiger were employed for the first time in coincident measurements of Compton scattering [25, 26]. After this success, Walter Bothe and Werner Kolhörster attempted to apply this technique in the field of cosmic rays [22]. This idea was later utilised by Bruno Rossi [27], who significantly improved the coincidental device and tested it in different configurations. For the first time, Rossi spanned the modules horizontally, observing multiple coincidences between counters, what is today known as the air-shower phenomenon [28, 29].

Pierre Auger and his group made a great contribution to this discovery by extending the coincidence separation to 300 m and estimating the energy of measured cosmic rays to PeV energy [30, 29]. His work has shed also a new light on the description of air-shower development. The understanding of these atmospheric cascades improved as the knowledge of particle physics developed, including the discovery of, among others, positron [31], muons [32, 33], pions [34, 35] and kaons [36].

The next decades brought many new experiments, distributed over the world and investigating characteristics of the cosmic rays. In parallel, the first theoretical explanation of the nature behind their accelerators appeared. Enrico Fermi proposed a shock front acceleration in the interstellar space [37]. The fundamental analysis can be performed by calculating the energy needed to power the measured flux of cosmic rays at different energies. This directly led to conclusions that up to PeV energies, or even higher, they can be powered by Galactic supernovae [2].

At this time, the first energy spectra of cosmic rays were obtained, based on the estimated number of particles in the air shower. In the PeV region, George Khristiansen and German Kulikov established the, today well-known, feature of spectral softening at 3 PeV, named as the knee [4] of the cosmic ray spectrum, using correlated hodoscopes. This was interpreted as the first hint that the observed feature is correlated to the highest energies of the Galactic sources.

After discovery of the cosmic microwave background (CMB) [38, 39], Kenneth Greisen, Georgiy Zatsepin, and Vadim Kuzmin brought up the conclusion that if the highest-energy cosmic rays are produced at large distances, a suppression of the intensity will be observed at a few tens of EeV due to the interaction with CMB photons [40, 41]. Since then, the search for the maximum energy and indications of the suppression become of even greater relevance.

With constant improvement of the detection methods and extensive work on the new detection channels using Cherenkov and scintillation light produced by secondary particles in the detector, the next ground-based experiments were built. The highly pioneering work was performed by an M.I.T. group led by Bruno Rossi with two experiments based on scintillation detectors, the Agassiz experiment [42] and the Volcano Ranch experiment [43, 44]. The latter was constructed in late 1950's by John Linsley and Livio Scarsi, who have brought an extraordinary contribution to the air shower physics. They established analysis tools for the determination of the cosmic ray observables from the spatial and temporal distributions of the signals. They are still used by many groups today. The Volcano Ranch array detected, at that time, the highest-energy cosmic ray of 100 EeV [45], encouraging even more to find out what powerful objects and mechanism produce these messengers. Other large experimental arrays, like Haverah Park, built from water Cherenkov detectors, or the Yakutsk experiment, built from scintillation detectors, have illuminated the features of the cosmic ray spectrum at the highest energies [46, 47], covering the region between the knee and expected end of the spectrum.

The field was brought forward when another remarkable idea was implemented by the Fly's Eye. This experiment observed air showers via fluorescence emission in the atmosphere [48]. This instrument provided a basis for the technique which nowadays is an important part of hybrid cosmic-ray observations, performed e.g. by the Pierre Auger Observatory [49] and the Telescope Array [50]. Fly's Eye detected to date the highest-energy cosmic ray of energy above 300 EeV [51]. The enormous showers were later confirmed by the array of scintillation and muon detectors in Japan at AGASA experiment [52].

The spectral features raised many discussions about their possible explanations. Theoretical attempts were made to infer the imprints of their astrophysical origin and perhaps changes of this origin at different energies. During this period, the astronomical instrumentations have significantly broadened the wavelength coverage of the observations. It started to be possible to observe objects in radio, UV, X-ray and γ-ray ranges. Space- and ground-based telescopes were observing deeper and better into the Universe. This resulted in numerous discoveries of new classes of objects, improving the understanding of our astrophysical environment, and hence allowed for a better correlation of the cosmic ray properties with the possible astronomical objects [29].

In the meantime, yet another field was born, nowadays known as neutrino astronomy. It started with the first detection of a solar neutrino in an underground detector of the Homestake experiment in the U.S. [53]. With development of our knowledge about particle interactions in the air showers, it became clear that neutrinos are also produced in the atmosphere. The first detection of atmospheric neutrinos was reported by underground experiments in a South African gold mine [54] and in the Kolar Gold Mines in southern India [55], which experimentally supported our understanding of the interactions in air showers. Around two decades later an outstanding event pushed the development of the astrophysics even further — an explosion of a supernova 1987A occurred and was widely observed by astronomical instruments and neutrino experiments [56]. For the first time it was possible to obtain a comprehensive picture of the supernova explosion in a wide electromagnetic range and to observe a neutrino signals from such a distant object. In the following decades, the development of astroparticle physics has been continued and after this long path, the large neutrino detectors were built, obtaining a clear signature of extraterrestrial neutrinos by the IceCube Observatory.

With a better understanding of the surrounding Universe, the possibility to explain the origin of cosmic rays increased. However, the exact answer to an already long-standing question is more challenging than maybe initially thought. Nevertheless, this parallel progress in different fields of research allows today for opening yet another window to the Universe. The real-time observation of signals originating from different astrophysical channels comprised a new goal of today's astroparticle physics, namely multi-messenger astronomy [57, 58]. It became clear that a complete picture of the astrophysical phenomena powering very energetic cosmic-rays can be obtained only via comprehensive synergy of different astrophysical channels: cosmic rays, electromagnetic radiation, neutrinos and gravitational waves. All of them bring to Earth particular signatures of a distant and violent Universe.

This short historical background shows how relevant and up-to-date are the questions about the nature of cosmic rays. It seems that only the observation of different astroparticle channels and merging the data can answer that puzzle. The following work is an attempt to put one piece of this puzzle on place, focusing on the improved detection of high-energy cosmic rays covering the prominent spectral characteristics.

1.2 High-energy cosmic rays

The cosmic rays coming to the Earth are mainly fully ionised nuclei which travel a long distance from different acceleration sites. The energies of these particles cover several orders of magnitude, starting from GeV particles produced in our Solar System to EeV cosmic rays born in extragalactic astrophysical objects, which are far more powerful than any human-made particle accelerator. The measured intensity of cosmic rays steeply drops with energy, generally following a power low behaviour with the spectral index of -2.7 and deviating from it at the higher energies starting from roughly 1 PeV [6]. The known distinct features, power breaks, at these energies are clearly visible in Figure 1.1. The spectrum shown in Figure 1.1 is multiplied by $E^{2.6}$ to magnify the features: the knee at about 3 PeV, the second knee at about 100 PeV and the ankle at 5 EeV.

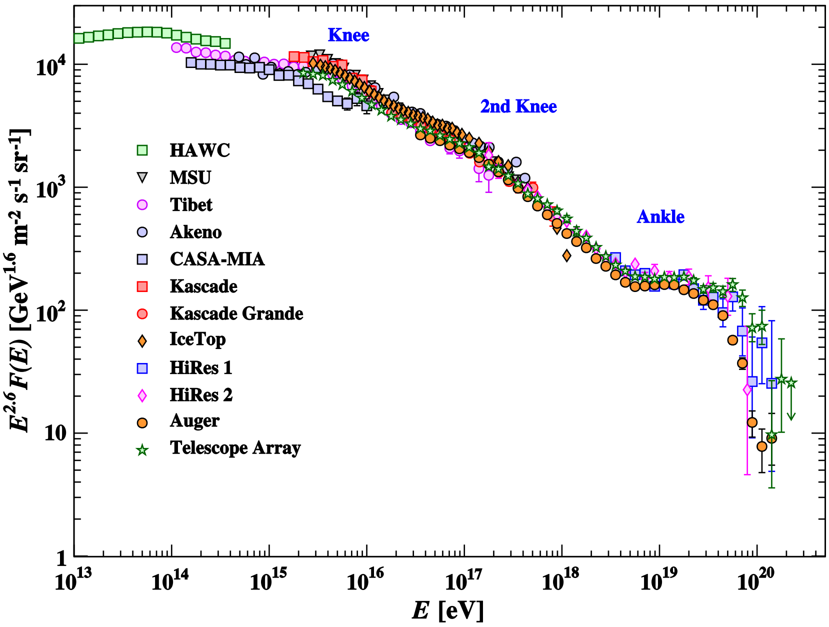

Figure 1.1: The cosmic-ray energy spectrum measured by different ground-based experiments. The three prominent features are marked in blue: a softening at 3 PeV and 100 PeV, and a hardening of the spectrum at 5 EeV. The plot is taken from the latest update of the Particle Data Group [6].

The whole range of energies where the cosmic rays are studied, conventionally is divided into sub-ranges: low energy, high-energy and ultra-high energy regions. The high-energy cosmic rays can be defined in the energy range from 100 TeV to 1 EeV, while the low-energy and ultra-high energies span below and above this region, respectively. The borders of this division are not very well defined and are rather a convention.

As briefly discussed in the previous section, the interest towards high-energy cosmic rays has been driven primarily by the measurements of the spectral breaks. Moreover, convincing experimental evidence of the mass-dependent position of these spectral breaks on the energy scale [10] was found. It has been shown that the knee is caused by the decrease of the contribution from the light mass group, while the second knee is most likely due to the suppression of the heavy component. This will be discussed in more detail in section 1.4.

1.3 Detection methods

From the experimental perspective the measurements of the cosmic rays can be performed in direct and indirect ways [59]. In the first technique, the cosmic ray itself can interact in the detector, which is deployed in Earth's orbit or mounted on a balloon. It can provide highly accurate information about the cosmic ray's energy and mass. These instruments take advantage of the great technological developments of the particle detectors in high-energy physics. However, the steeply falling spectrum limits these experiments to measurements in the TeV range due to their small aperture [60].

In the case of indirect measurements, at higher energies, the phenomenon of extensive air showers is utilised. The cosmic ray first interacts with the Earth's atmosphere, which in this case acts as a large calorimeter, and the secondary particles from the atmospheric cascades can be observed by ground-based detectors. A coincident measurement of the signals from detectors distributed over a large area allows for inferring the information about the primary cosmic ray based on the spatial and temporal distributions of the cascade components.

Details about the extensive air showers and their use for deriving the cosmic ray properties are discussed in the following sections.

Extensive air showers

Extensive air showers are cascades of secondary particles initiated by the cosmic ray interacting in the Earth's atmosphere [61]. In the first interaction, the cosmic ray collides with a nucleus and produces mainly charged and neutral pions and other hadrons. These products propagate further and in the subsequent interactions generate other particles. The process repeats, leading to an avalanche of the particle interactions limited only by the competition between the interaction and decay probabilities.

The neutral pions π^0 generated in the first interaction and in the subsequent interactions decay immediately into photons in the reaction (in brackets the characteristic decay time is given [6]):

$$\pi^0 \rightarrow \gamma + \gamma \qquad\qquad (\tau = 0.85 \times 10^{-16}\,s).$$

The electromagnetic particles develop extensively creating numerous sub-cascades. The energy which is contained in these cascades is then lost through ionisation of the atmosphere.

The charged pions and kaons can start other interactions with nuclei of the atmosphere sustaining the development of the hadronic component of the shower. With decreasing energy probability of their decay increases, leading to a creation of the muonic component (in brackets the characteristic decay time is given [6]):

$$\pi^{\pm} \rightarrow \mu^{\pm} + \nu_{\mu}(\bar{\nu}_{\mu}) \qquad\qquad (\tau = 2.6 \times 10^{-8}\,s).$$

The resulting muons have low energy losses, rarely interact and hence can travel long distances, penetrating even deep into the ground. A substantial fraction of the hadrons on the ground emerge from the interactions in the hadronic core of the shower. Neutrinos produced in the different interactions can reach high energy and carry a significant part of the cascade energy.

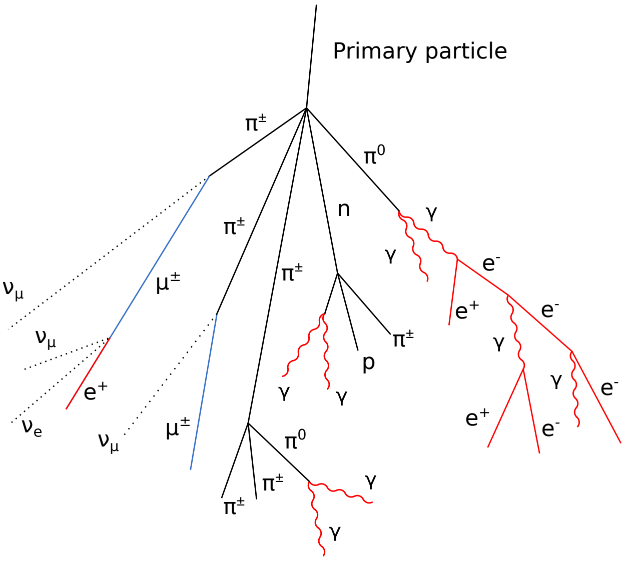

Figure 1.2: Scheme of an air shower induced by a high-energy cosmic ray and generating cascades of different particle components: hadronic (gray), electromagnetic (red), muonic (blue) and neutrino (dotted lines) component. The scheme was inspired by [62].

Due to the kinematics of the collisions, the generated secondary particles propagate mainly forward along the momentum of the primary cosmic ray. However, the transverse momentum and multiple scattering lead to the lateral spread of the shower. The particle cascades continue to increase until the energy contained in the shower cannot sustain further production and the maximum development is reached. The atmospheric depth at which this happens is referred to as the shower maximum, X_{max}. Eventually, the cascades die out and mainly the energetic components survive until the ground. The electromagnetic component decreases very quickly after the maximum, while muons essentially stop their production.

The theory of these electromagnetic cascades has been developed in the 1930s with one of the first works by Homi Bhabha and Walter Heitler [63]. The cascade equations were further studied by Lev Landau and Georg Rumer [64], applying more accurate assumptions. In the next decades, Nishimura and Kamata found new solutions to the theory [65, 66, 67, 68]. Greisen found also a practical approximate form which is still widely used [69, 70].

Walter Heitler provided also a model which is very useful for understanding the basis of the air showers [71]. It assumes that after the interaction of an electromagnetic particle, two secondaries are produced, splitting the initial energy, E_0, equally. After n of such interactions the energy is reduced to $E_0/2^n$. Number of such divisions, n, can be expressed as $n = X/\lambda$, where X is a thickness of the passing medium, in this case atmospheric depth X, and λ the mean free path of electromagnetic particles, both given in g/cm^2. From this, a dependence of X_{max} on primary energy can be deduced, which shows that higher energy cosmic-rays generally manifest a bigger X_{max} since the cascade is sustained longer.

James Matthews extended this model to hadronic showers [72], assuming similarly that n hadron interactions are generated. This time, the energy is divided in a different way due to existence of 3 types of pions: 2/3 of initial energy goes to charged pions and 1/3 to neutral. As already mentioned, neutral pions generate further electromagnetic cascades which determine the X_{max} position which depends on the primary energy and number of subsequently generated secondaries. An important implication of the aforementioned assumptions is a superposition model. Namely, the cosmic ray being a nucleus of A nucleons and given energy E, can be represented as A individual nucleons with energy E/A. This can simply explain the higher number of muons for heavier nuclei and lower value of X_{max} at a given energy: $N_{\mu}^{A} = N_{\mu}^{p} A^{\alpha}$ and $X_{\max}^{A} = X_{\max}^{p} - \lambda \ln(A)$ [72].

These rather basic assumptions are a great tool to explain fundamental features of air showers. However, in the case of hadronic cascades in particular, there is far more complexity in their interactions. In very energetic air showers, a significant number of the hadronic interactions occur with a low momentum transfer. This causes a divergence of the solutions in perturbative QCD [73]. Due to a lack of exact descriptions or good approximations, there are many phenomenological models attempting to describe hadronic interactions and are extensively used in the simulations. Hence, at present they constitute the main uncertainties across different high-energy cosmic ray measurements. With a bulk of data from particle accelerators they are constantly being tuned to describe the observed collisions, and at the same time agree with the measurements from the air showers. However, cosmic rays interactions happen at higher energies and in more extreme forward direction than available in accelerators. Thus, hadronic models apply extrapolations of the cross sections, from available data to the required phase space.

Detection channels

When these secondary particles and radiation come to the ground, they leave signals in the detectors spanned across hundreds of metres to several kilometres depending on the energy of the primary particle. The size of the emerging footprints essentially determines the scale of the instruments that should be used for their detection, which can be realised with different detector types [61], briefly described in the following section.

Particle detectors

The secondary particles of the air showers can be detected on the ground with particle detectors consisting of a scintillation material [61]. The passage of particles in this material ionises it, creating a light with respective light yield. By collecting and measuring the intensity of this light one can estimate the energy deposited in the material by the crossing particles. More details are given in the next chapter. Cherenkov detectors work in a similar way. In this case, relativistic particles traversing a dense and optically transparent medium (water or ice) generate Cherenkov radiation which again can be measured by optical sensors. The technique of the particle detectors is very reliable and does not depend on the external conditions and effectively detect various shower components. Utilising different particle detectors, which respond differently to these components, increases the capabilities of the cosmic ray's mass discrimination.

Radio emission detection

Air showers can be also observed via detection of radio emission [74]. The electric field is generated when air-shower particles are separated in the Earth's magnetic field [75] or due to the differences in their movement [76, 77]. Since this emission is mainly driven by the electromagnetic component, it carries a large fraction of the initial cosmic-ray energy. Thus, on one hand the radio array can provide a good estimation of the cosmic ray energy and on the other hand, in combination with other methods, which are sensitive to different components, it can enhance the mass composition sensitivity [78].

Fluorescence detection

During the propagation in the atmosphere, the air shower excites the air molecules, mainly nitrogen. Release of such excitation causes an emission of fluorescence light [79]. Through this effect, the atmospheric cascades can be seen by fluorescence telescopes. This method provides the most precise measurements of the longitudinal profile of the air shower and hence the shower maximum and the cosmic ray energy. A good understanding of the atmosphere profile is however required to correctly analyse the measurements, which has been overcome in the recent experiments by precise atmospheric monitoring [80]. Unfortunately, the energy threshold for air shower detection using this technique is high.

Air-Cherenkov-light detectors

Due to high kinetic energy, many of air shower particles exceeds the speed of light in the air, causing an emission of the Cherenkov light. This emission comprises another detection channel for air showers which is highly sensitive to the electromagnetic component, providing a better determination of the primary energy. However, such measurement can be performed only during clear and moonless nights, which limits the operation time and hence the exposure of the Cherenkov detectors.

1.4 Important results of studies of high-energy cosmic rays

Our current knowledge about cosmic rays and their related phenomena is very broad. Besides new ground-based experiments, space and balloon borne missions significantly contributed over the years to the current understanding of these messengers. However, in the following, only important and rather recent results from high-energy cosmic rays will be discussed.

Energy spectrum

A compilation of the differential cosmic-ray spectrum measured by many different indirect and direct experiments was recently combined into one global spline fit [81]. The results are presented in Figure 1.3. The method estimates the position of the actual flux based on the large set of the cosmic ray data and systematically accounting for the experimental statistical and systematic uncertainties. Since the direct observations are the most accurate, they drive the correction. This data-driven approach provides the most accurate estimation of the cosmic ray's flux to date. In contrast to other models the global spline fit parametrisation does not rely on theoretical assumptions. However, comparison of this result with other models like H4a [82], that assume particular classes of the sources can provide new insights. In addition to the all-particle spectrum, the global spline fit parametrisation provides estimations of the elemental groups from proton to nickel for the whole energy range of the observed cosmic ray data.

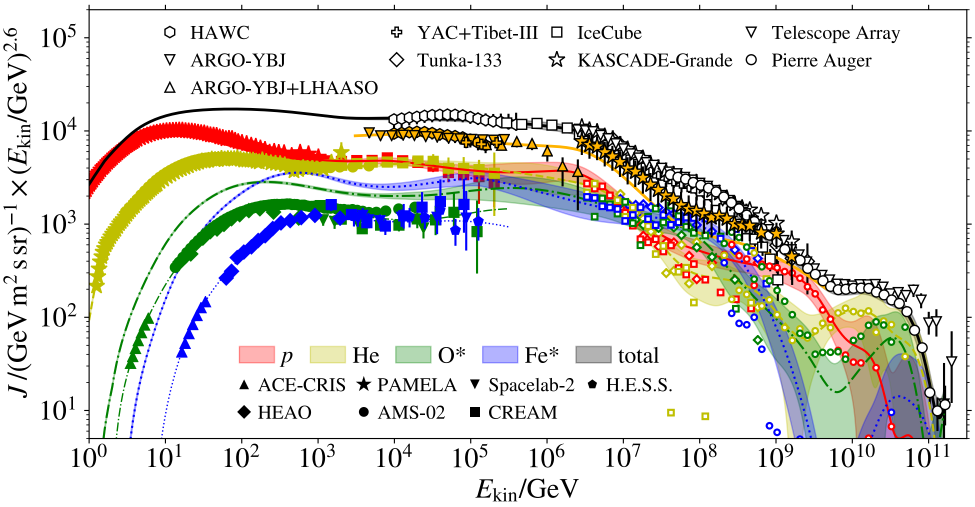

Figure 1.3: Compilation of differential cosmic-ray flux measurements from modern direct (filled markers) and indirect experiments (open markers). The all-particle flux is presented in black and individual elements and elemental groups in different colors. Global Spline Fit to the combined measurements was performed. Figure is taken from [81].

In this combined picture, the prominent spectral features are even more visible. The features are also observed in the individual spectra at shifted energies. Despite these clear characteristics, their nature remains not fully understood. There exist several interpretations which can be constrained with more precise measurements.

Mass composition

The mass or elemental composition is one of the key measurements that can be performed in the field of the cosmic ray astrophysics. It traces the information from the source, the acceleration as well as the effects associated with the propagation. Highly accurate measurements of the composition can provide insights into these complex and not fully understood processes.

The main challenge, however, lies in the indirect nature of the mass composition studies at high energies. The information is convoluted in the air shower development and detector response. Nevertheless, it has been shown that some characteristics of the air showers are correlated to the primary cosmic-ray mass. Commonly used observables are the shower maximum or the relative number of muons and electrons [83].

One of the best measurements in this context were performed by KASCADE and its extension, the KASCADE-Grande experiment. With detection of different air shower components, the effective separation of different elemental groups was achieved [10, 84]. The results are depicted in Figure 1.4. At PeV energies, the abundance of the light elements is higher and starts to decrease at the end of the knee. A drop of the light component causes a softening of the knee and the heavier elemental group becomes dominant. The measurement of KASCADE-Grande (Figure 1.5) further support this argument showing the ankle-like structure for light primaries and a significant contribution of the heavy cosmic-rays to the second knee [85, 86].

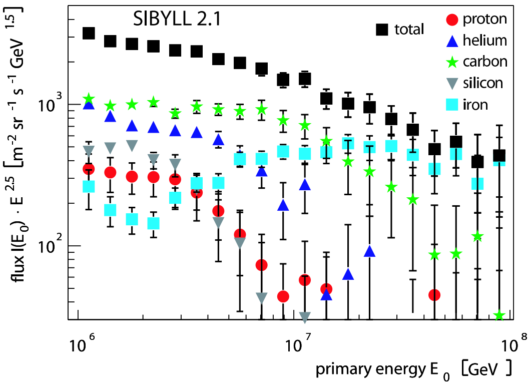

Figure 1.4: Differential flux of cosmic rays: total (black) and elemental groups (colors) measured by the KASCADE-Grande experiment. Figure is taken from [10].

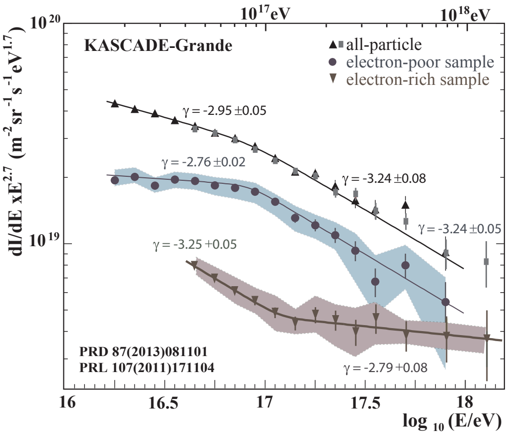

Figure 1.5: The cosmic ray spectrum measured by KASCADE-Grande, indicating light-mass enriched (H-like) and heavy-mass enriched (Fe-like) contributions. Figure is taken from [86].

The observed dependence is probably the first observation of the so called Peters cycle — gradually shifting the position of the spectral break with the charge of the primary cosmic ray [9]. This emerges from the rigidity dependence of the strength of the particle interaction with the magnetic fields for the accelerating source and the interstellar medium. The relative abundance of the elements changing over this cycle traces astrophysical processes both in the source and during the propagation to the observer. Despite this pivotal evidence, more precise measurements are essential to understand details of this behaviour. Recently, also IceTop results confirmed these features, but due to large uncertainties the fine details can not be resolved.

After the second knee, the cosmic ray flux continues until energies of 100 EeV where a suppression is observed. Nuclei of such high energy cannot be confined in our galaxy and they will escape indicating their extragalactic origin. Moreover, the lack of the local anisotropy and significant observation of a dipole structure pointing outside of the galaxy support this hypothesis [11]. It is unclear at which energy the galactic contribution is surpassed by the extragalactic accelerators. The big question about the transition is also on the existence of an additional component of the galactic cosmic rays [12, 3] which fills the gap between the contribution from supernovae and from the extragalactic sources.

Anisotropy

The presence of galactic and extragalactic magnetic fields perturbs initial trajectories of the cosmic rays and changes the overall picture of their propagation. The values of the fields affect the paths of the cosmic rays, in the way that at Earth they are almost fully isotropised. This means they propagate in a diffuse motion. Indications of some asymmetries in this context are a hint of the nearby sources.

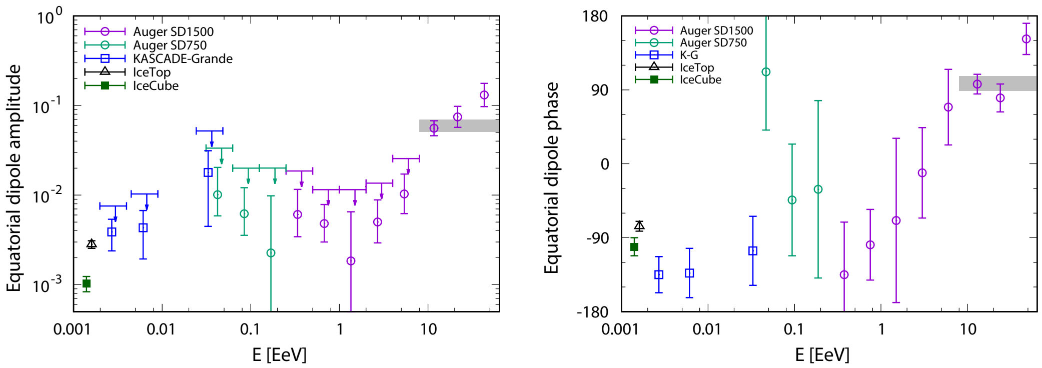

Figure 1.6: Parameters of the dipole anisotropy analysis in high-energy range obtained by different ground based experiments. The amplitude and phase of a dipole changes with energy. Figure is taken from [87].

Recently several research groups reported about an observation of an anisotropy of the incoming directions of the cosmic rays in the energy range of the transition and also below [87, 88, 89, 90, 91]. An anisotropy at lower energies seems to be consistent between various observatories, and points close to the direction of the Galactic Centre. The parameters of the dipole anisotropy are shown in Figure 1.6 for three experiments covering different energy ranges. The dipole amplitude increases at higher energies while the phase changes the direction to the opposite one at EeV energy. However, further investigation needs to be made, correlating anisotropy with spectral features of the individual spectra of different cosmic-ray species.

Attempts to identify sources

Based on the significant progress in the understanding of the characteristics of the astrophysical objects, many attempts have been made to identify where cosmic rays come from and how they are accelerated. The current interpretation states that up to PeV energies, or even higher, the cosmic rays are powered mainly by Galactic supernovae.

Further insights can be obtained by observations of the electromagnetic counterpart from a given cosmic-ray source [93]. If a given object produces neutral pions decaying to gamma rays, it indicates that there are hadronic processes occurring in the source. This in turn means that such object can accelerate cosmic rays. The observations of high-energy gamma rays from the Galactic supernova remnants, performed by Fermi-LAT satelite [94], gave evidence that the supernovae are in fact Galactic cosmic-ray sources [95]. A picture of this particular Fermi source is presented in Figure 1.7. In this context, the softening of the spectrum at

PeV energies has multiple interpretations. The main ones point that either the softening is connected to the particles escaping from the Galaxy or the main Galactic components, i.e. supernovae, are running out of the acceleration power. Both conclusions lead to a dependence of the spectral feature on the cosmic-ray mass.

The measurements of gamma-rays in the context of understanding the cosmic-ray origin is limited by the interactions of photons with the interstellar medium. Photons of around 1 PeV energy can travel roughly a radius of the Milky Way and hence at these energies one can observe only Galactic sources. Neutrinos are another messengers which can point back to the cosmic-ray sources, since they are produced, among others, in the decay of charged pions [96]. They are characterised by low cross-section, which together with neutral charge, makes them difficult to measure. Nevertheless, astrophysical neutrino search has been particularly successful after installation of the IceCube Neutrino Observatory at the South Pole (see Chapter 2). Neutrinos together with GeV photons significantly contribute to search for cosmic-ray sources.

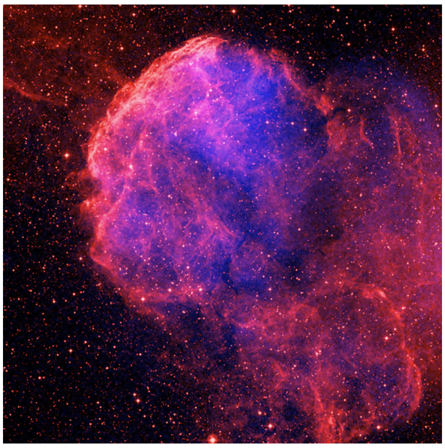

Figure 1.7: The picture of IC 443 supernova remnant in optical (red) and X-ray (blue) ranges. Figure is taken from [92].

Therefore, a parallel development in cosmic-ray, gamma-ray and neutrino observations in a realm of multi-messenger astronomy at different energies is crucial to address the problem of the cosmic-ray origin.

1.5 Remaining challenges

Despite significant progress in high-energy cosmic rays, the evidence for a particular source of cosmic rays with energies above PeV is not very strong, especially in the region where extragalactic sources are expected to overcome the contribution of the Galactic cosmic-ray flux. Currently, the uncertainties across different experiments in the determination of individual mass spectra are large and do not allow for definite conclusions. In Figure 1.8 current uncertainties on the measurements of the mass composition are presented together with possible astrophysical models. To constrain these models, more precise measurements are needed. For further details see [81].

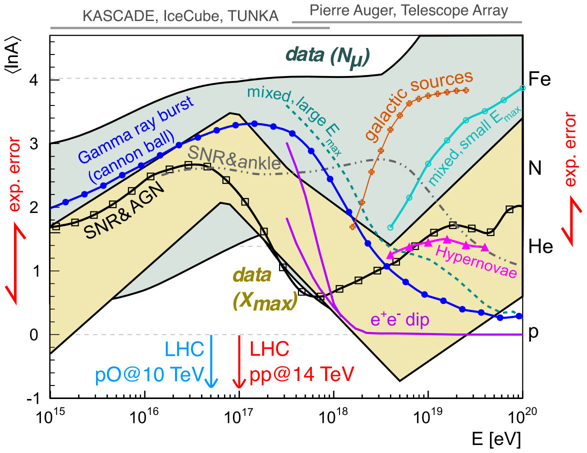

Figure 1.8: The experimental and model uncertainties on the mass composition of the cosmic-rays over the transition region and above. The figure is taken from [81].

Besides difficulties in mass estimation, the reconstruction of the primary energy still carry large uncertainties. Many experiments in the high-energy range rely on simulations, which in turn depend on the phenomenological models of hadronic interactions. Because these hadronic models are used to interpret the observed air-shower measurements, it can lead to discrepancies in the estimation of the absolute value of the cosmic-ray spectrum observed by different experiments, in particular particle detectors. The attempt to achieve an overlap in energy range with direct measurements will help to understand some of the resulting uncertainties from less accurate air-shower measurements.

Deeper and better astrophysical searches keep opening in front of the scientists new windows on the Universe. Like Rossi and Auger to cosmic rays, now IceCube together with many other detectors open the next one by identifying sources of high-energy neutrinos. The field currently enters a new era of multi-messenger astronomy and large multi-wavelength campaigns to seek for remaining unanswered questions, and perhaps even beyond them.

Chapter 2

ICECUBE AS COSMIC-RAY DETECTOR

2.1 IceCube

The IceCube Neutrino Observatory, hereafter IceCube, is located at the geographical South Pole [97]. Its primary goal is the detection of sources of cosmic-ray acceleration via the observation of high-energy astrophysical neutrinos from 10 TeV to a few PeV. IceCube consists of more than 5000 digital optical modules with photomultiplier tubes, attached to 86 strings installed around 2.5 km deep in the Antarctic ice. The scheme of the detector is depicted in Figure 2.1.

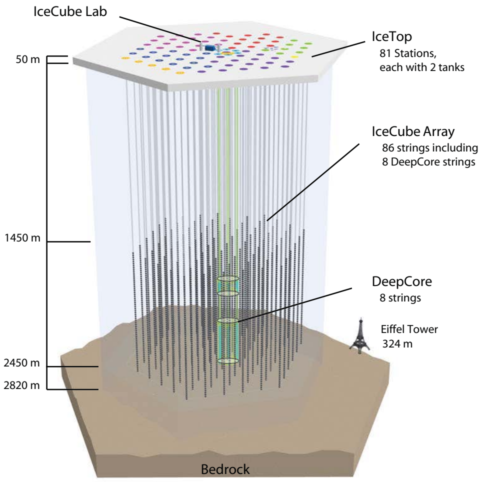

Figure 2.1: A scheme of the IceCube detector. Vertical lines show positions of the strings with optical modules. The DeepCore, a denser region inside the centre of the IceCube is also indicated, as well as the positions of the IceTop stations at the ice's surface. The scheme is taken from the IceCube collaboration.

When a high-energy neutrino travels through ice, it can interact leaving a high-energy muon, electron or tau depending on its flavour, or a hadronic cascade. The secondary charged particles produce Cherenkov emission which can be then observed in coincidence by optical modules. Analysis of the signals and timestamps allows for reconstruction of the direction and energy of the incoming neutrino. The topology of the deposited signals indicates in addition the flavour of the neutrino.

The inner part of IceCube, where strings are installed denser, referred to as DeepCore, serves as a unique low-energy neutrino detector, observing GeV neutrino oscillations [98]. These neutrinos are not of astrophysical origin but come from air showers, as described in Chapter 1.

Latest results

Measurements of high-energy muon tracks in IceCube allow for cosmic-ray anisotropy studies, by assuming that these tracks follow the primary cosmic-ray direction. In collaboration with the HAWC experiment the map of cosmic-ray arrival directions has been obtained at energy of 10 Tev, showing large and small anisotropic structures [99]. The map with a multipole fit is shown in Figure 2.2, confirming that the large-scale anisotropy is aligned with the Local Interstellar Magnetic Fields. This feature could be explained by the rotation of the Solar System. However, conclusions, in particular based on small structures, are highly non-trivial due to the large uncertainty in the strength and directions of the Galactic magnetic fields.

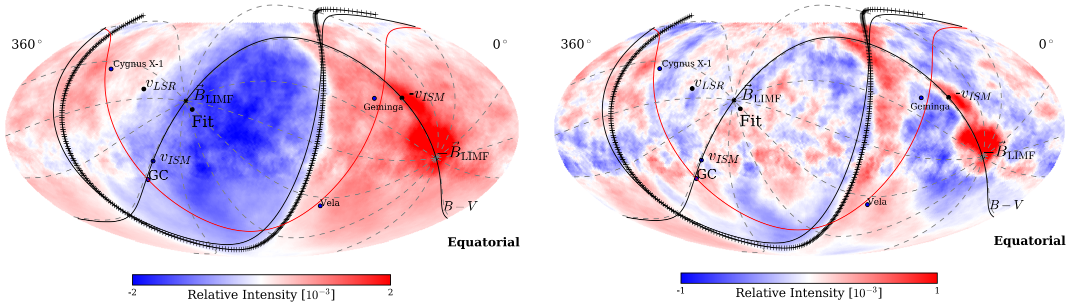

Figure 2.2: Relative intensity before (*left*) and after (*right*) subtracting the multipole fit from the large-scale map. Fit and Local Interstellar Magnetic Fields line are marked in black. Figure is taken from [99].

In the context of cosmic-ray research, the most prominent recent IceCube result has been done in a very different direction. In 2017 IceCube detected a high-energy neutrino in coincidence with other observatories detecting electromagnetic radiation [100]. The results from Fermi-LAT revealed an activity of a blazar — an active galactic nuclei pointing towards Earth [57]. The simultaneous observation of neutrino and gamma rays is an indication that such an object is probably a cosmic-ray accelerator. There are many theoretical approaches discussing this possibility [101, 102, 103]. This boosted a large campaign of real-time alerts between different observatories distributed over the globe and in the orbit, creating for the first time multi-messenger realm of astroparticle physics.

To discover even more, IceCube is currently undergoing an upgrade phase. New solutions for optical modules are being tested and will be deployed in the next years to increase the sensitivity to low-energy neutrinos. They will be also tested in terms of the next generation of IceCube. IceCube-Gen2 is expected to cover 10 km^3. Such extension will essentially allow for increased statistics and better measurement of the spectral features in the high-energy, astrophysical neutrino flux, as well as enhanced sensitivity for point source studies.

2.2 IceTop

The surface array of the IceCube Neutrino Observatory, called IceTop, is a cosmic-ray detector measuring extensive air showers initiated by primaries with energies from PeV to EeV. This covers the very interesting range where transition from cosmic-ray energies dominated by Galactic sources to extragalactic sources is expected to happen [104]. It comprises of 81 pairs of ice Cherenkov tanks located close to the IceCube strings. A photo of such a pair of IceTop tanks is shown in Figure 2.3.

Due to the rather high altitude of 2835 m, which corresponds to 680 g/cm^2 (vertical atmospheric depth), the air showers seen by IceTop have their maximum of development very close to the detection level or even below. This is an advantage, since it provides a higher sensitivity to the cosmic-ray mass than the measurements taken at sea level due to less fluctuations in the signatures. IceTop provides very accurate measurements of the air-shower lateral and time distributions. Due to the good response of the tanks to muons, it can distinguish the

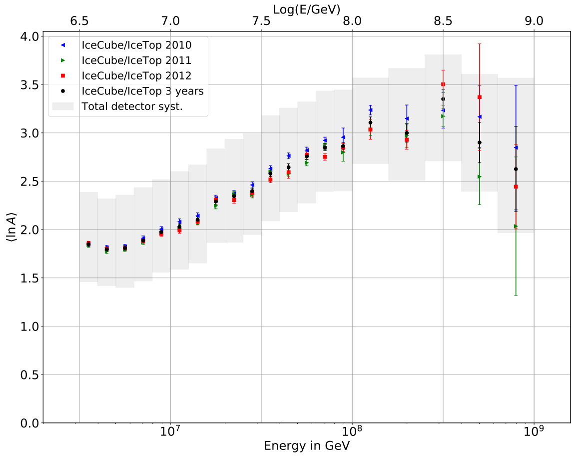

Figure 2.4: The average natural logarithm of the cosmic-ray atomic number as a function of energy. Despite large uncertainties, the increased contribution for heavy nuclei is observed towards the second knee. Figure is taken from [104].

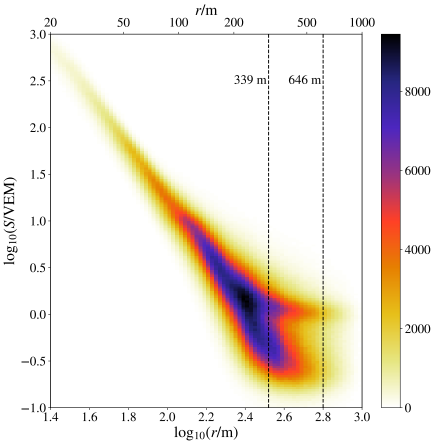

Figure 2.5: The lateral distribution of IceTop hits for proton induced air showers of PeV primary energy. The distinct, thumb-like feature corresponds to muons arriving far away from the shower axis. The plot is taken from [105].

muonic contribution at larger distances from the shower axis [105]. The signal of muons is visible as a distinct feature in the lateral distribution depicted in Figure 2.5. However, due to the accumulation of snow on top of the tanks, around 20 cm/year on average [17], the energy and mass determination from IceTop data suffers from increased uncertainties. Nevertheless, large efforts have been made to understand and account for this effect [17].

The remarkable benefit of IceTop is the unique location above the in-ice array. The air showers produce, besides a bulk of secondary particles of different and relatively low energies, also high-energy muons. They will penetrate deep into the ice, leaving a track correlated in time and space. This signal of the shower core can be later reconstructed in coincidence with the surface measurements, making IceCube a 3D cosmic-ray detector. This idea was employed in a recent analysis of cosmic-ray mass composition [104]. The results are presented in Figure 2.4. Clearly, the heavy composition at the position of the second knee can be observed. However, large systematic and still statistical uncertainties limit further conclusions.

Figure 2.3: The IceTop ice Cherenkov tanks during deployment at the South Pole. Two detector placed next to each other comprise a station. The IceTop tank is equipped with two optical modules collecting the Cherenkov light. The photo is taken from IceCube Collaboration.

2.3 Surface enhancement

The further improvement of IceTop as a cosmic-ray detector requires a new approach which can boost the measurements, but at the same time enables easier and more cost-effective deployment [106]. As a solution, detectors of new types were proposed to be installed, namely, a surface enhancement with scintillation detectors and radio antennas distributed across the IceTop footprint [107].

The planned array will comprise of a large number of detectors, providing more points to sample air-shower footprint and fit the underlying distributions. The choice of the detector layout is discussed within this dissertation in Chapter 4. The particular chosen layout for the time being is planned to consist of 32 stations of 8 detectors each, where 2 detectors are placed close to each others in pairs. This particular design was optimized for trenching-length reduction and a uniform distribution of the scintillator panels among the IceTop tanks.

Motivation

The scintillation modules were chosen due to their different response to the air-shower components emerging not only from different light emission mechanism, but also from their very different geometries. Both detectors are sensitive to muons and electromagnetic particles, however in the IceTop tanks muons can generate a larger signal amplitude than in scintillators. This means that at some lateral distance the difference between two responses can be maximised. Moreover, the energy deposit in tanks from air-shower photons is limited due to the overburden by snow, introducing a bias in the signal measurements.

The plastic modules are also significantly easier to deploy due to their light weight. This is a reason why they can be elevated above the snow, avoiding accumulation. Keeping scintillators snow-free will allow for improvements in non-trivial calibration of the tank signals with respect to their snow heights.

The larger number of detectors, by almost doubling the sensitive area (currently: $405\,\mathrm{m}^2$, after enhancement: $789\,\mathrm{m}^2$), effectively lowers the detection threshold of IceTop. Enabling detection below the knee of the cosmic-ray spectrum can give better understanding of the transitions between different mass groups. Going closer towards energies covered by the direct measurements allows also for a comparison of the absolute energy scale, which is far more accurate with direct instrumentations. The increase of the sensitive area will also rise the capabilities for the in-ice measurements. Due to the large atmospheric background, most neutrino tracks coming from southern sky need to be rejected. While the IceTop detection threshold is currently high, it cannot efficiently veto low-energy air showers which can still produce high-energy muons in the first stage of the shower development. More sampling points at the surface simply increase the probability of their detection. However, these studies are complicated and include considerations of the very rare deep air-showers. Such cascades exhibit a higher probability to produce a high-energy accompanying neutrino or muon, while remaining undetectable at the surface. Therefore a detailed analysis needs to be performed to account for actual veto capabilities. Nevertheless, it can be improved as indicated by this simple geometrical considerations.

In this context, scintillator detectors and radio antennas will serve in the upcoming years also as a test for future solutions for the next generation of IceCube. It is planned to employ one of these techniques as a large-scale veto array to increase the coverage of the southern sky. This coverage does not only increase the statistics but it includes the region of the emission from the Galactic Center. As it was discussed in other studies [108], it is a possible source of PeV photons, which were so far not detected, making it even more interesting direction.

The planned installation of the radio antennas gives a bulk of new scientific cases and advantages, which are broadly discussed in [106]. Mentioning only few of them, installation of the radio array together with scintillation modules will make IceTop a unique, hybrid detector. Such solutions are not new [109, 110], but at the moment are explored also by other experiments [111]. The radio detection provides an independent and accurate measure of the electromagnetic, thus leading component of the shower. Merged with other techniques it enhances the mass separation capability of the array. Finally, due to the larger aperture it enables measurements of very inclined air shower. They leave large footprint in the radio signal [112] and manifest properties which are highly enhanced by their increased trajectory in the atmosphere. In this case, scintillators can be considered as 2D detectors, which are not capable of an effective air-shower detection at high inclination.

Prototype deployment

The first two prototype stations, consisting together of 14 detectors, with little different designs in mechanical structure and the read out electronics, were deployed at the South Pole in the Antarctic summer of 2018/19 for on-site testing. The detectors have successfully taken data, enabling detailed studies of their response and, in particular, behaviour of the data acquisition system. The calibration using minimum ionising particles was possible and compared later with the simulation results described in Chapter 3. The station was also observing coincident signals from air showers. An example of a 7-fold-coincidence event detected by station is presented in Figure 2.6. By finding the coincidence time window between the IceTop and the scintillator stations offline, the detected air show-

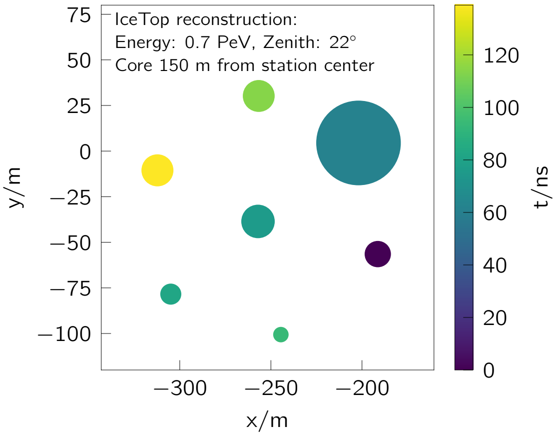

Figure 2.6: An air shower recorded by the prototype station. The circles indicate detector positions and their size is correlated with the signal amplitude. Colours represent the trigger times. The event was detected in coincidence with IceTop, which reconstructed its energy as 0.7 PeV with the shower core 150 m away from the station center.

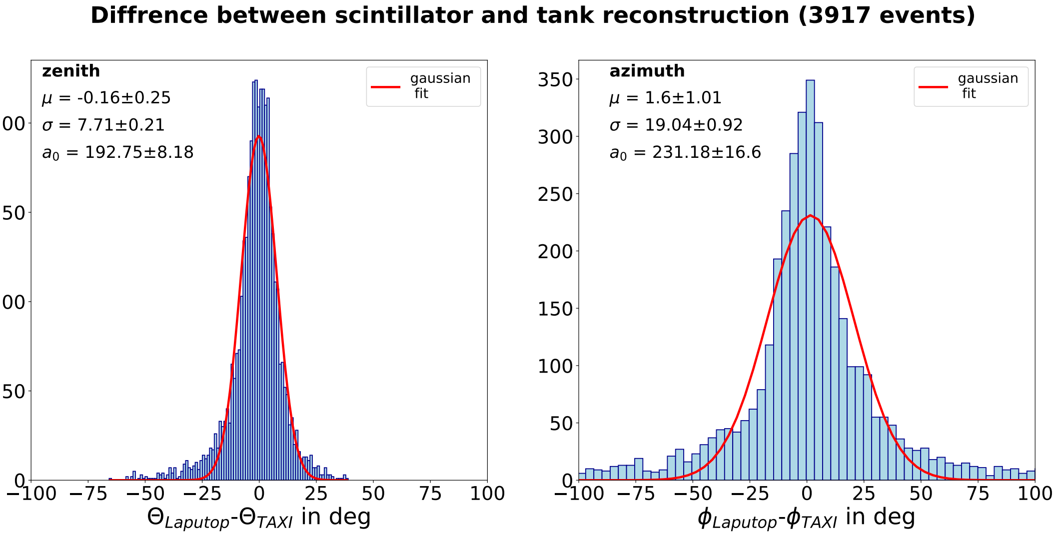

Figure 2.7: A comparison of reconstructed zenith (*left*) and azimuth (*right*) angle by scintillator station and the IceTop array for events measured in coincidence. Figure is taken from [113].

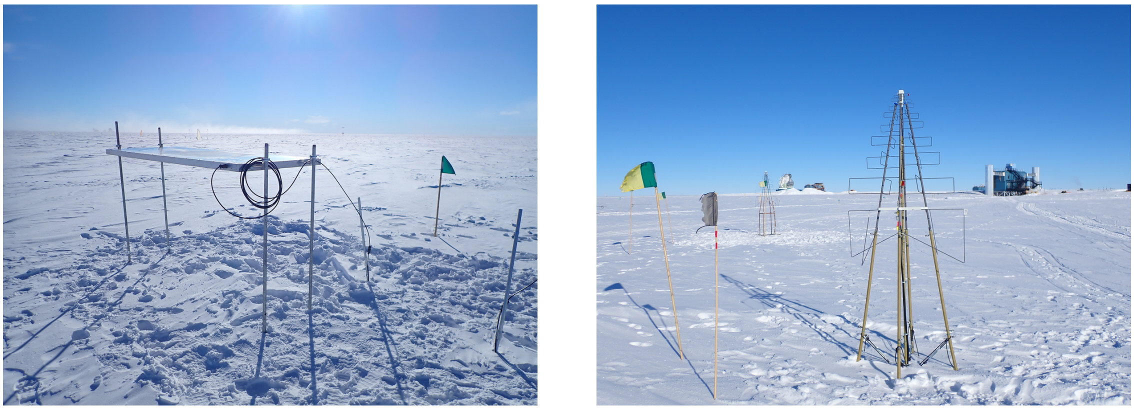

Figure 2.8: Scintillator module (*left*) and radio antenna (*right*) deployed at the South Pole in the austral summer of 2019/2020 and 2018/2019. Photos are taken from the IceCube Collaboration.

ers could be reconstructed using simple algorithms and then compared to the more refined and accurate IceTop reconstruction [113, 16]. The comparison between zenith and azimuth angles of the incoming cosmic rays reconstructed by the scintillator station and the full IceTop array is shown in Figure 2.7. The small differences on the level of tens of degree indicate a good time resolution of the deployed station and proves the capability of this instrument to detect air showers. In the following deployment seasons also prototype radio antennas were installed at the South Pole. In the austral summer of 2019/2020 one full station of the enhancement, 8 scintillation modules and 3 radio antennas, was deployed including the new hybrid electronic system. The photos of the latest installed scintillation modules and radio antennas are presented in Figure 2.8. The aspect of optimised data acquisition system is crucial for coincident measurement of the air showers, but also for providing an external trigger for the radio antennas, which cannot use a self-triggering system yet.

Scintillation detector module

The prototype design was inherited from AugerPrime [13]. The decision of a particular detector design and materials are strongly dictated by the analysis and measurements performed by collaborations from other experiments like the MINOS Experiment [114, 115] and the Pierre Auger Observatory [13, 116].

The scintillation detector consists of 16 extruded polystyrene bars with dimensions of $5\,\mathrm{cm} \times 1\,\mathrm{cm} \times 187.5\,\mathrm{cm}$, giving $1.5\,\mathrm{m}^2$ of sensitive area. The plastic material is doped with 1% PPO and 0.03% POPOP. Extrusion provides some resistance to damages. Each bar is coated with a reflecting TiO_2 layer of $250\,\mu$m. A photo of a cross section of a single bar is shown in Figure 2.9. Scintillation photons are guided through the wavelength-shifting (WLS) fibres (Y-11(300) Kuraray) via kidney-shaped holes in the bars. The light is propagated to a readout system, which is based on a silicon photomultiplier (SiPM) [107, 117].

To provide light-tightness, the scintillator is wrapped in a polyethylene foil with high static dissipative properties. On top of the detector, styrofoam pieces are placed to provide support and to fill the casing. Additional support structure is given by the wooden elements on top and below the bars. The detector is encapsulated in a very thin aluminium sheets of a 1 mm thickness. One of the prototypes is shown in Fig. 2.10. Such a module has a weight of less than 50 kg which makes it easier to manually deploy them in the harsh environment.

The data acquisition is based on FPGA system called TAXI [118]. It has been extensively improved and adjusted to the particular case of the IceTop enhancement [119, 120]. The system employs a μ-DAQ to read the data from the scintillators which are further send to the Field Hub. The Field Hub is an external box for each station which holds all necessary electronics to power the detectors and the readout and connects the station to the IceCube laboratory. The integrated online charges and timestamps from the scintillators as well as full radio waveforms are sent to the IceCube Lab where further selection and transfer of the data to the North takes place.

Figure 2.9: The side view of the plastic scintillator bar with kidney-like holes for guiding the wavelength-shifting fibres. The white layer around is a reflective material consisting mainly of TiO_2, which prevents photons from escaping the bar.

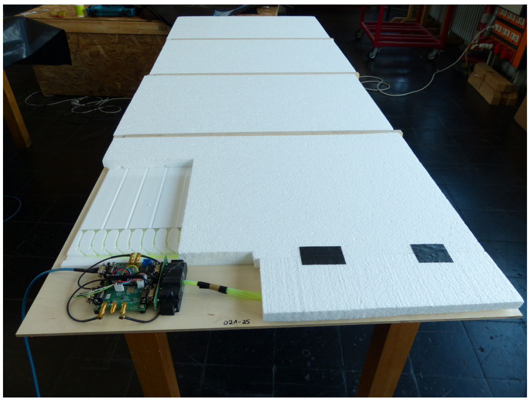

Figure 2.10: View to the insight of a scintillation detector with support structures and parts of the electronic system. Such a module is then encapsulated in an aluminum casing. The photo is taken from [121]

Scintillator characteristics

Due to their characteristics, the scintillator detectors are used by many applications in physics, in particular due to efficient conversion of particle kinetic energy to scintillation light inside the material.

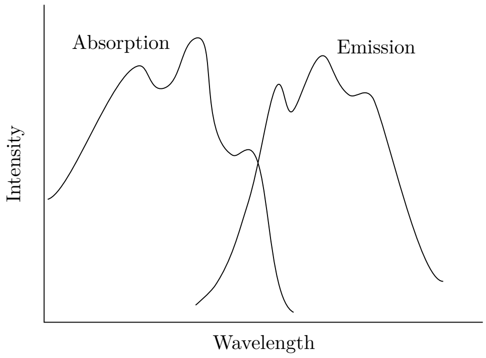

Figure 2.11: Sketch of absorption and emission spectra of organic scintillator based on [122]. A small overlap between both is present.

The used plastic scintillators belong to the group of organic scintillators. The scintillation process in organic materials is the emission of photons during the transition between excited states of a molecule and its ground electronic state, following the absorption of energy from charged particles [122]. However, the scintillator material can also detect photons, when they cause an emission of a charge particle inside the material. The main light is emitted via de-excitation in a fast channel of fluorescence, which can be described by the exponential decrease with small characteristic decay time. The second channel of the emission is delayed due to de-excitation via longer lived states. It can contribute to the overall signal with a delay.

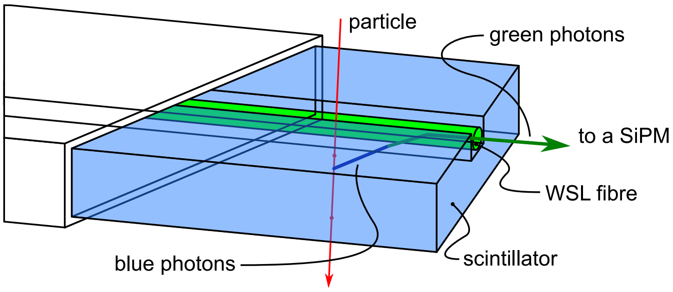

Figure 2.12: Scheme of processes happening in the scintillator and wavelength-shifting fibres. Particles crossing the detector generate UV light which is shifted to blue via dopants and to green via fibres. Figure was inspired by [123] and modified by [124].

Due to the fact that states for a prompt emission have in majority lower energy than the one necessary for the absorption, there is a small overlap between the absorption and emission spectra of a scintillator as shown in the sketch in Figure 2.11. This means that scintillators only partially absorb their own light. To improve the main material, in our case polystyrene, the base of the scintillator is doped with primary and secondary scintillating compounds. In the case of the discussed modules these are PPO and POPOP. The primary dopant improves the production of scintillation light, while the second one absorbs this light and shifts it to the visible light range, which is easier to detect and which is attenuated after longer propagation distances [122]. The emitted light is then collected by the wavelength-shifting fibres to shift the light further in order to better match the range in which the SiPM operates. These fibres provide a good light collection due to the reflections of the photons on their inner walls. The above described process is summarised in Figure 2.12.

Chapter 3

THE SIMULATION BASIS

A proper understanding of every experimental result has to be based on a comprehensive description of an underlying theoretical model or simulation. Exhaustive simulation studies are particularly relevant when analysing processes which are largely fluctuating, like in the case of extensive air showers. The variations in the development of the atmospheric cascades have to be taken into account to be able to draw valid conclusions on the final observables which can help to reconstruct the primary cosmic ray.

For the surface enhancement of IceTop, it is relevant to properly evaluate the capabilities of a particular air-shower array; namely, the detection and reconstruction efficiency, as well as resolutions of determining the physical parameters. Thus, a detailed simulation chain was constructed. In the first step, the atmospheric cascade initiated by a cosmic ray is simulated, providing a distribution of the particles at the observation level along with the information about the air-shower development. Then particles are further propagated through the detectors and the final detector signal is calibrated. The details of these steps are discussed below.

3.1 Cosmic-ray air shower simulations

In the first step, the cosmic-ray air shower simulations are performed using CORSIKA (COsmic Ray SImulations for KAscade) [125], which was initially developed for the KASCADE experiment. In the following years it has become the leading tool for the research in the field of cosmic-ray physics. The program simulates the creation and the development of an

Name of parameter	Set value
Primary (PRMPAR)	H, He, O, Fe, γ
Energy slope (ESLOPE)	-1 (within every energy decade)
Zenith (THETAP)	0°–50°
Azimuth (PHIP)	-180° – 180°
Observation level (OBSLEV)	2842 m
Energy cuts (ECUTS)	20 MeV, 10 MeV, 100 keV, 100 keV
HDPM Interaction Parameters (HADFLG)	0 1 0 1 0 2
To use NKG and/or EGS4 (ELMFLG)	T T
To use Sibyll model (SIBYLL)	T 0
To use cross-sections provided by Sibyll (SIBSIG)	T
Electron Multiple Scattering Length Factor (STEPFC)	1.
Muon multiple scattering angle (MUMULT)	T
Model transition (HILOW)	80 GeV
Model of atmosphere (ATMOD)	13
Magnetic filed (MAGNET)	16.40 μT, -53.4 μT

Table 3.1: List of input parameters for CORSIKA simulations in the scope of this work. Parameters which influence only on the additional output files are not listed.

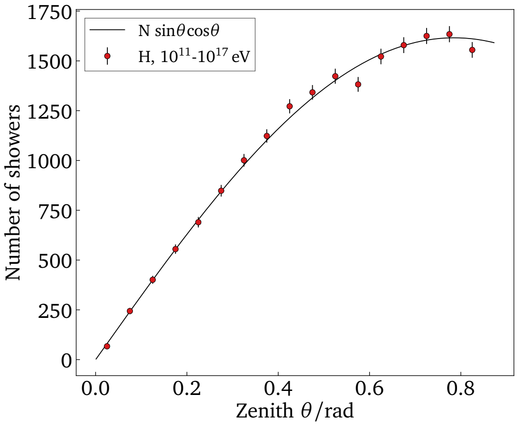

Figure 3.1: Zenith angle distribution of air-shower simulations resulting from the CORSIKA sampling algorithm, for H primary with energies from 100 GeV to 100 PeV. The fit curve is proportional to the distribution for the flat horizontal detector.

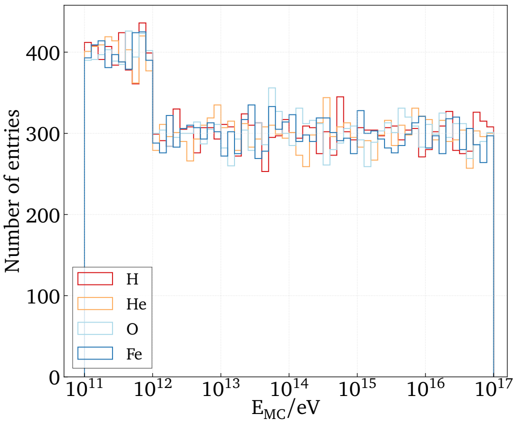

Figure 3.2: Energy distribution of air-shower simulations for H, He, O, Fe primaries with the zenith angle range from 0° to 50°. There are more simulations in the lowest energy bin.

extensive air shower initiated by a given cosmic-ray primary. Due to its quite broad flexibility, it allows a user to choose a configuration suitable for a particular experimental site and introduce a set of initial parameters for every simulation. The entries in the steering card influence on the first stage of the air-shower simulation and therefore on the propagation of the particles in the atmosphere. These properties shape the final air-shower characteristics at the ground, which are further included into the detector simulations. The detailed description of the possible settings can be found in the CORSIKA guide [126].

The set of relevant parameters used in the simulations in the scope of this work is listed in Table 3.1. The existing steering cards suitable for IceTop simulations could not be directly applied to the one for the scintillator array, due to the differences in the response of an ice-Cherenkov tank and a scintillation detector. The energy threshold to produce Cherenkov light is higher than the one for scintillation-light production. In the following paragraph a motivation for the chosen values for the most relevant parameters is presented, guiding from the primary particle interaction to the final output.

The 7.6400 version of CORSIKA was configured with the option of a flat horizontal array. A random generation of the zenith angle, θ, was done, by sampling a $dN/d\theta \propto \sin\theta\cos\theta$ distribution which takes into account the geometrical acceptance of the surface detector. The θ range varies up to 50° as shown in Figure 3.1, while the azimuth angle is chosen from -180° to 180°. The South Pole atmosphere chosen for the simulations is that of the 1st October 1997, which is the beginning of the austral summer (MSIS-90-E [126]). However, it was shown [127] that the extreme seasonal variations at the South Pole have a considerable effect on the air-shower development. Changing the temperature influences the production of high-energy muons, and therefore may affect the measurement of the cosmic-ray composition. Therefore, dedicated studies accounting for the influence of this will have to be performed for the data analysis in the future. Moreover a more accurate model of the atmosphere at the

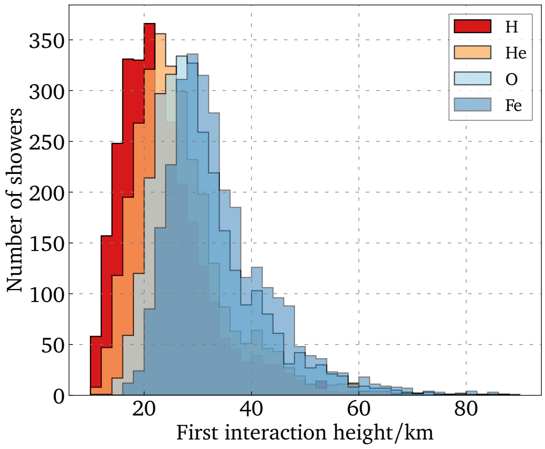

Figure 3.3: The distribution of heights of the first interaction for different cosmic-ray primaries with 10–100 PeV energy.

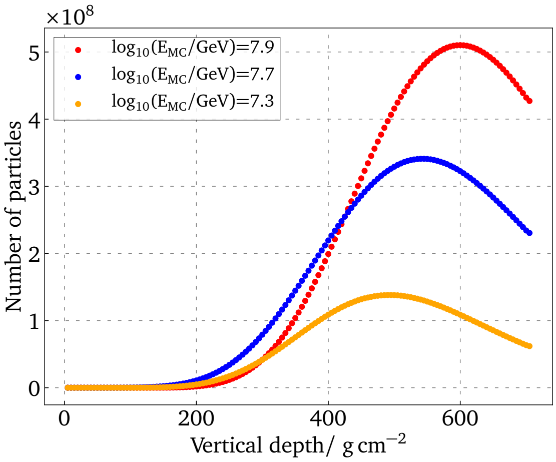

Figure 3.4: The vertical longitudinal profiles representing all particles of single proton induced air-showers with primary energies 10–100 PeV.

IceTop site currently exists and should be used for future studies. The value of the magnetic-field strength was chosen as 55.86 μT with an inclination of -72.93°. These are standard values used for the IceTop simulation production. However, according to the International Geomagnetic Reference Field model for 90° latitude on the prime meridian, recent values as of November 2019 are 16.785 μT for the horizontal intensity and -51.963 μT for the vertical one [1]. Therefore an additional study with all these updated parameters should be performed following this work, specially taking into account future hybrid-detector analysis. Moreover, some additional configuration options should be considered.

CORSIKA can simulate an atmospheric cascade initiated by different primary particle types as well as nuclei with a mass up to that of iron, with energies ranging from GeV to EeV. For this work, the parameters of the injected primary particles were established based on the areas of interest described in section 2.3: the energy region around the knee, the ability to reach energies lower than the threshold of IceTop, and mass discrimination of different species. Therefore, simulated primary energies range from 10^{11} to 10^{17} eV and are randomly generated from a flat power law distribution to obtain similar statistics in every logarithmic bin as presented in Figure 3.2. Five primary species were investigated: hydrogen, helium, oxygen, iron nuclei and photons. In different parts of this work different subsets were used. Since the computing time of simulations for these energies is still acceptable for the purpose of this thesis, the algorithm of thinning was not used. However, to prepare a larger set of high-energy simulations, specially for the hybrid simulations including different detector types, the thinning algorithm will need to be applied. This algorithm does not track all particles with energy below a certain fraction, but instead combines them, applying an appropriate weight.

The first interaction point of the primary particle as well as the target of the interaction are chosen randomly by CORSIKA with the top of the atmosphere being around 112.8 km. They

---

[1] Values obtained from `https://www.ngdc.noaa.gov/geomag/calculators/magcalc.shtml#igrfwmm`

depend on the cross-section of the interaction with the air molecules. The higher-mass cosmic rays interact in average higher in the atmosphere what can be seen in Figure 3.3. This interaction starts an atmospheric cascade, which creates the electromagnetic and hadronic sub-cascades. The rate of the interactions and decays depends on the particle energy and cross-sections [128]. The cascades develop longitudinally along the shower axis. The atmospheric depth at which the maximum of air-shower development occur, X_{max}, is correlated with the primary type and energy [61]. In Figure 3.4 the examples of single vertical longitudinal profiles are presented for proton induced air-showers with increasing energy. Both, the first interaction height and X_{max} influence on the footprint seen by detectors at the ground.

The current theoretical description of the electromagnetic component is relatively well understood with new models being developed to improve this understanding [129]. High-energy hadronic interactions cannot be fully described using QCD and hence are modelled using phenomenological approaches together with an extrapolation of accelerator data of lower energy [73]. They constitute the highest uncertainty in the interpretation of air-shower data and thus their influence should be studied in detail. For the treatment of the electromagnetic cascades, the software was configured so that Nishimura-Kamata-Greisen (NKG) and electron-gamma-shower (EGS4) [130] models are used, including the Landau-Pomeranchuk-Migdal effect [131] which is activated for the latter model. This effect accounts for the suppression of electromagentic processes due to the multiple scattering at large longitudinal distances, though it has relatively small influence on the air-showers below EeV energy [132]. The EGS4 allows for setting a factor which changes the length of multiple scattering for electrons and positrons. In this study we leave it without changes by setting STEPFC to the default value 1. The EGS was configured to create electrons and gammas down to 100 keV. The hadron-nucleus collisions below 80 GeV energy in the laboratory reference frame are simulated by the FLUKA [133, 134] package. High energy hadron-nucleus as well as nucleus-nucleus interactions are treated by SIBYLL 2.3c [135].

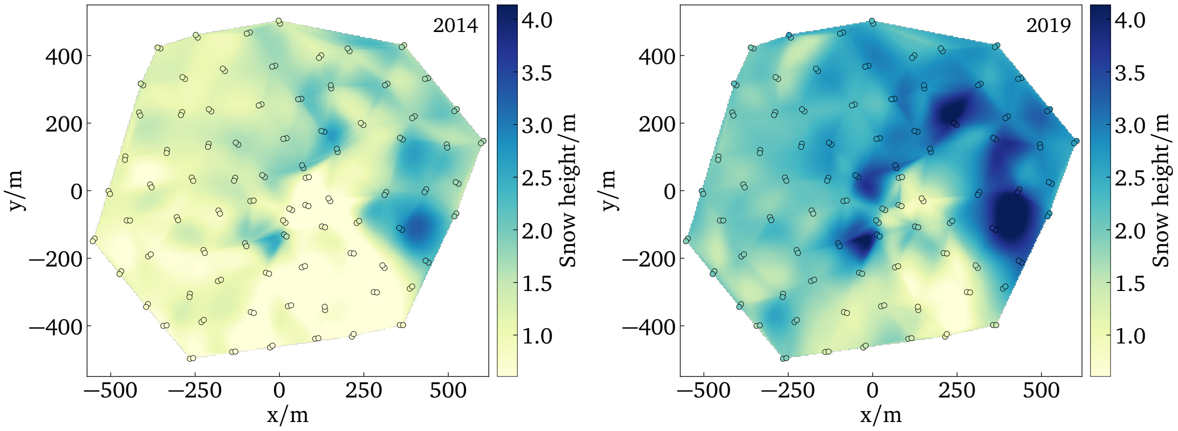

Figure 3.5: Heights of snow accumulated above IceTop tanks as of March 2014 (left) and 2019 (right). The map was created using cubic interpolation from *scipy*. The non-uniform accumulation is connected, among others, with the fact that tanks were installed over a few years period with the first part being the upper-right region. The distribution changes close to the buildings, like for instance IceCube laboratory.

The main output of such air-shower simulation consists of the position and momentum of each particle at the chosen observation level of 2842 m (703.68 g/cm^2), which is 4 m above the position of the scintillator panels. The position of the scintillator panels is, for the time being, the same over the whole array and is above the highest level of the snow surface measured in March 2019 [2]. The map of the snow heights above the IceTop tanks is depicted in Figure 3.5. The highest coordinate is 1953.51 m altitude, and therefore the scintillator panels are simulated at 1954.08 m in the IceCube coordinate system which corresponds to 2838 m elevation in the CORSIKA coordinate system. Comparing maps in Figure 3.5, one can notice that the mean accumulation of the snow on top of the tanks increased by 1 m within 5 years. For this reason each scintillator will be placed on 2 m high extendable poles.

The type of the secondary particle, its coordinates, momentum and arrival time with respect to the time of the first interaction of the cosmic-ray primary with an atmospheric nucleus are recorded. However, such extensive cascades create enormous amount of particles of which many low-energy ones do not create a signal inside a detector. Therefore, CORSIKA limits the number of saved particles by introducing cuts on the energy below which the particle is not tracked anymore and no information about its possible secondaries is stored. The cuts can be set for hadrons (without π^0), muons, electrons and photons (with π^0). It is not possible to use CORSIKA without any energy cuts as the lower limits on these values exist and are as following: 20 MeV for hadrons (when running with FLUKA option), 10 MeV for muons and 50 keV for electrons and photons. In order to properly adjust the energy cuts we analyzed the spectra of those particles directly from the CORSIKA output. The Figure 3.6 represents the number of $e^{\pm}, \mu^{\pm}$, γ and hadrons which arrive at the ground from air showers initiated by different cosmic-ray primaries. The electromagnetic component dominates significantly over all other secondaries. It can be also seen that with increasing cosmic-ray mass, the number of electromagnetic particles decreases while the number of muons increases and is the lowest for γ-showers, for primaries of the same energy range. These are important characteristics of air showers, often used in discriminating the cosmic ray species [83], as described in Chapter 7. The spectrum of hadrons has some distinctive features which are coming from single hadron contributions. The peak at 0.1 GeV originates from low-energy protons and neutrons, and the one at 10 GeV mainly from $\pi^{\pm}$. More detailed plots are in Appendix A. The significant difference in the number of hadrons, between cosmic ray and photon induced air-showers, can be seen as well. However at this stage what is relevant for further simulations is that all shown particles still contribute to the spectral peak, for instance there is still some production of low energy muons at 10 MeV, in particular at higher cosmic-ray energies. Therefore, the minimum values for energy cuts for hadrons and muons are kept. In addition, the single-detector response to $e^{-}, \mu^{\pm}, \gamma$ was evaluated with different incident energies (see sec. 3.2). The 100 keV cut for the significant electromagnetic component is dictated by the threshold value below which there is not any more a substantial signal generated in the detector. Further details are presented in the next section.

---

[2] Measurements done by the IceCube Collaboration

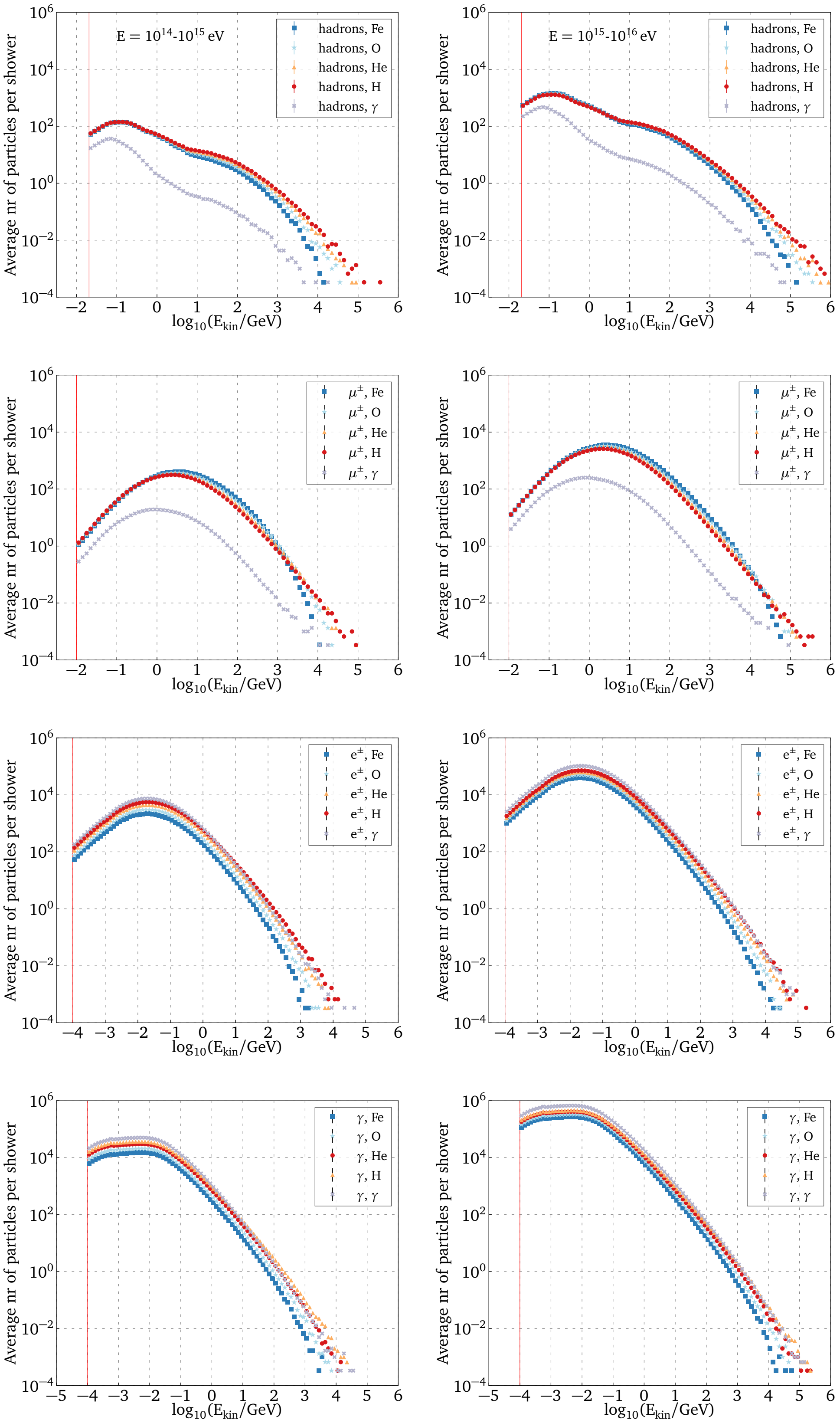

Figure 3.6: Secondary particle spectra for different primaries and two energy bins: left 10^{14-15} eV, right 10^{15-16} eV. Each plot contains 3000 air-showers per type of primary. The red vertical lines indicate energy cuts set in CORSIKA.

3.2 Simulation of the detector response

The next step of the simulation chain is to propagate the particles produced by CORSIKA through the array of the scintillation detectors and Cherenkov tanks and record the corresponding generated signals. This part is performed using the Geant4.10.5.p01 toolkit [136]. Geant4 calculates the total energy deposited by a particle passing through a given volume and records its time, track length and information about the corresponding processes and produced secondary particles. A choice of the required physics processes, taken into account during simulations, and an implementation of the detector geometry are the two most relevant aspects of preparing the Geant4 setup. As shown in Figure 3.6, the spectra of particles at the ground, which have to be processed via Geant4, extend over a few orders of magnitude in energy. Therefore, different physical processes should to be considered. For that reason, the *G4ModularPhysicsList* interface was used, which includes few of standard Geant4 lists, namely: *G4EmStandardPhysics*, *G4EmExtraPhysics*, *G4DecayPhysics*, *G4RadioactiveDecayPhysics*, *G4StoppingPhysics*, *G4IonPhysics*, *G4IonElasticPhysics*, *G4HadronElasticPhysics*, *G4HadronPhysicsFTFP_BERT* [137]. This set of *PhysicsList* covers processes which air-shower particles can undergo inside the detectors or in their vicinity (atmosphere, snow). However, for instance a very-high energy π or K cannot be processed in the snow therefore less than few percent of the simulations will result in an error and are rejected. An influence of these hadronic models in the scintillator-array simulations was partially studied but more systematic analysis needs to be performed. These processes are used when calculating the energy deposited inside a detector's sensitive volume. The dominant processes of energy losses by a particle traversing matter are electromagnetic effects. Charged particles undergo ionization, bremsstrahlung, pair production, multiple Coulomb scattering – and for positrons also annihilation. Photons participate in pair production, photo-electric effect and Compton/Rayleigh scattering. Hadronic interactions involve strong-interaction processes in the nucleus such as photonuclear and electronuclear reactions, inelastic and elastic scattering or hadron capture. They are more complicated since their theoretical description in some regimes is not completely obtained, hence phenomenological models are required to describe them [137, 128]. Along with physics models, Geant4 introduces the production cuts below which no secondary particle can be produced. These cuts are given by the ranges which a particle can travel in a particular material. They were set to the same values in all materials, namely: 0.1 mm for $e^{\pm}$ and protons and 0.5 mm for γ. Expressing those ranges into the energy cuts shows that the limit on γs is much lower than on $e^{\pm}, \mu^{\pm}$. Therefore, γ range was increased in comparison to the other three types of particles. Some comparison with different cuts can be found in Appendix B.

Particles produced by CORSIKA are read out and propagated through the detector array using the projects *topsimulator* and *g4-tankresponse* of the IceCube software. These projects were developed for IceTop tank simulations and are now extended with the relevant modules for the scintillator panels.[3] In the initial step, a grid of all surface detectors which are included in a *GeometryCalibrationDetector* (GCD) file is created. For each particle, a corresponding

---

[3] The modified projects, as well as additional projects created for scintillation detectors and radio antennas, are part of the *SurfaceArray* meta-project in the IceCube software.

position bin is found and a map of nearby detectors is passed further. In the next step, an additional geometrical check is performed, passing to the Geant4 module only those particles whose trajectories cross a certain volume around a given detector. This significantly reduces the computation time for Geant4 simulation. These procedures were already developed for the tank simulations and were further tested after the inclusion of the scintillator modules. Whenever a particle is injected into a detector, a new Geant4 event is initialized.

During the iteration over all detectors in the array, the signal generated by every particle passing through each detector is added up and the sum is assigned to the respective detector. However, to fully simulate an optical detector in Geant4, the photon-tracking option needs to be enabled. Simulating such optical processes, like Cherenkov radiation or scintillation, requires a long computing time. For a large-scale simulation this becomes unfeasible, therefore the response of the single detector, using more detailed simulations, is parametrised and the optical processes are not simulated anymore. While the response of the Cherenkov tank has been already extensively studied [138] (briefly described below), some of the characteristics of the scintillator panels had to be understood in detail and are presented below.

IceTop Cherenkov tanks

The simulation model of an IceTop tank consists of a polyethylene container filled with ice, 90 cm from the bottom, and perlite from the top. Two pressure-glass spheres filled with SiO_2 are inserted as shown in Figure 3.7. The sensitive area of an IceTop tank is $\approx 2.6\ \mathrm{m}^2$ for vertical incidence. From the previous detailed studies of the tank's properties [139], the response of a single tank is estimated using the number of generated Cherenkov photons inside a sensitive volume. The amount of produced light is calculated as the total number of Cherenkov photons generated along the particle track inside the tank [139]:

$$\frac{\mathrm{d}N_{Ch}}{\mathrm{d}x} = \frac{\alpha}{\hbar c} z^2 \left(1 - \frac{1}{n^2\beta^2}\right) \Delta P, \tag{3.1}$$

where α is the fine structure constant, z is the charge of the particle and β is its velocity, n is the refractive index, ΔP is the range of photon energy and dx the length of the Geant4 step (it describes a change during particle propagation [140]).

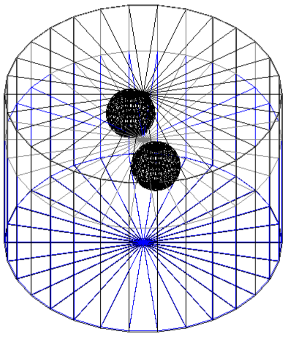

Figure 3.7: Geometry of the IceTop tank as implemented in Geant4. The black spheres indicate the model of DOMs, blue contours show a volume of ice, and gray lines – a volume of perlite.

A response of the IceTop tank is further expressed in the number of Cherenkov photons created by the simulated vertical muons of a fixed energy. This step is followed by the generation of photoelectron (PE) series with times. This series is then passed to the PMT simulator which generates the waveforms, which are processed further by the module simulating the DOM-mainboard response. The final signal calibration is based on vertical atmospheric muons (so called vertical equivalent muons — VEMs). Majority of atmospheric particles are minimum-ionizing particles — MIPs, mainly electrons and muons, which at some energies show a constant ionisation rate. The contribution of muons and electrons to the charge spectrum depends on the type and volume of a detector, hence calibration can be done to MIPs itself or to their vertical component only. This technique is commonly used for the calibration of cosmic-ray particle-detectors [141], and was already utilised decades ago [43]. In the IceTop simulations the resulting charge is calibrated to VEM units based on the simulated PE spectrum from low-energy air-showers, scaling the peak position so that it matches the corresponding VEM calibration data [142].

As it was mentioned earlier, IceTop tanks are covered with snow, therefore this effect is also simulated. Using measurements of the snow height above each tank, as shown in Figure 3.5, the snow surface is modelled in Geant4 using Delaunay triangulation [139]. The resulting model is shown in Figure 3.8. The snow density of 0.38 g/cm^3 is assumed, based on the measurements at the South Pole [143].

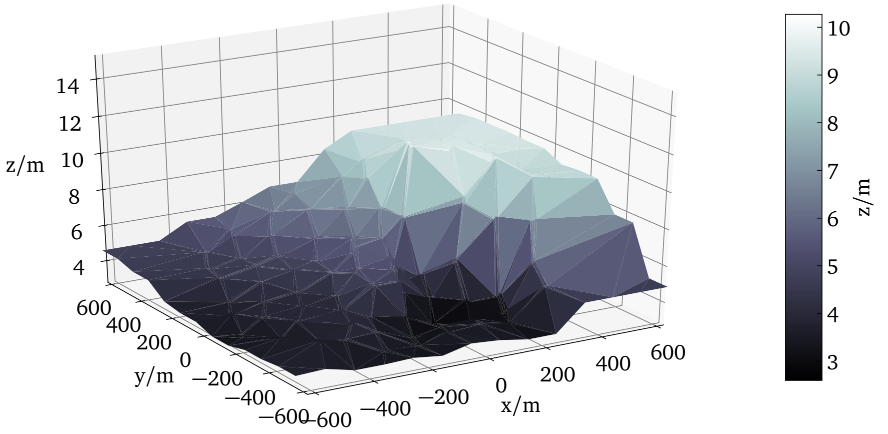

Figure 3.8: The heights of the snow above the IceTop tanks with respect to the bottom of the lowest position of the deployed IceTop tanks. By finding a crossing position with a particular triangle surface, one can determine the extrapolated heights of the future scintillation panels.

Scintillator panels

The simulated model of the scintillation detector consists of 16 Fermilab scintillator bars made out of polystyrene (Dow STYRON 663W) with two dopants: 1% of PPO + 0.03% of POPOP [144], which are highly efficient scintillators [122]. In addition, POPOP is a wave-shifting component which absorbs the light from the primary dopant and converts it to longer wavelengths [122]. The scintillator bars are simulated with a 0.5 mm thick reflective layer containing TiO_2 with a concentration of 10% by weight, and in total have a size of 5 cm × 187.5 cm × 1 cm. It has been shown that TiO_2 significantly increases the amount of collected scintillation light [145, 146]. The particular values of the thickness and concentration were studied by the MINOS collaboration [114].

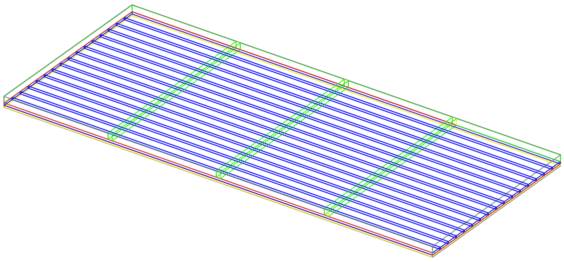

Figure 3.9: Geometry of a single scintillation detector as implemented in Geant4. Dark blue indicates scintillator bars, cyan - positions of air holes inside them, red - their coating, yellow shows wooden structures and green the styrofoam filling.

In the real panels, each bar has two kidney-shaped holes along the bars for fibre routing, as shown in Figure 2.9. For simulations a simplified model is used with a cylindrical hole of 2.5 mm diameter, filled with air. In the simulation model in addition, a 27 mm thick styrofoam and wooden blocks are placed but only on top of the bars. The total active area of the panel is 1.5 m^2. Everything is inserted in an aluminium casing of 1 mm thickness. In reality, the scintillator bars are covered with a black foil to provide a light tightness, however, since its effect on the particle propagation is assumed to be small, this detail is not included in the detector simulation. Such a detector geometry, as presented in Figure 3.9, is inserted in a Geant4-based module contained in the *g4-tankresponse-scintillator* project. The densities of the above materials used in Geant4 are listed in Table 3.2.

Material	Density
Polystyrene (C_8H_8)	1.06 g/cm^3
POPOP ($\mathrm{C_{24}H_{16}N_2O_2}$)	1.204 g/cm^3
PPO ($C_{15}H_{11}NO$)	1.094 g/cm^3
TiO_2	4.26 g/cm^3
Plywood ($C_6H_{12}O_6$)	0.7 g/cm^3
Styrofoam (C_8H_8)	0.01414 g/cm^3
Aluminum	2.699 g/cm^3

Table 3.2: Densities of scintillator-detector materials used in Geant4.

The number of created scintillation photons is calculated from empirical, non-linear Birks's equation [147]. It takes into account the excitation quenching which reduces the light output and leads to its saturation at higher energy losses.

$$\frac{\delta N_{scint}}{\delta x} = \frac{S\,\frac{\delta E}{\delta x}}{1 + k_B \frac{\delta E}{\delta x}} \quad \Leftrightarrow \quad N_{scint} = \sum_i \frac{S\,\frac{\delta E_i}{\delta x_i}}{1 + k_B \frac{\delta E_i}{\delta x_i}} \delta x_i\,, \tag{3.2}$$

where $\frac{\delta E}{\delta x}$ is the energy loss per unit path length. The parameter k_B is the Birks' coefficient which differs between materials and experimental conditions, and refers to the number of the molecules which lead to the de-excitation without the light production [148]. In the scintillator material used here, it is taken as 0.111 mm/MeV [148]. S is the scintillation light yield which is the number of photons which can be created per unit of released energy, in our case it is taken as 8960/MeV [4]. The length of the path, δx is the length of the Geant4 step, and so the integral from Equation 3.2 effectively becomes a sum over all steps.

---

[4] Since the exact value for FNAL scintillator was not known, it is taken as 80% of BC-408 light yield [149], which is taken as 56% of anthracene yield which is 20000/MeV according to `http://detecsciences.com/api/files/535012e58cd6be252e000081-Scint_Brochure.pdf`

Energy deposition

The generated number of scintillation photons from Equation 3.2 is based on a fundamental quantity, the energy loss. The energy loss of the particle passing through matter depends on the type of particle and its energy, as well as on the properties of the given material.

Single $\mu^{\pm}, e^{-}$, and γ particles were injected into the scintillator panel with two discrete values of the zenith angle, i.e. 0° and 50°, and continuous energy ranges as presented in Figure 3.10. The response of the detector to muons reveals some distinct features of different interactions types[5]. The lowest energy muons decay in the air before entering a detector but the secondary electrons still can deposit some energy within the sensitive volume through: $\mu^{-} \rightarrow e^{-} + \bar{\nu}_e + \nu_\mu$ and $\mu^{+} \rightarrow e^{+} + \nu_e + \bar{\nu}_\mu$. Close to 10 MeV, muons enter a detector and decay inside. The corresponding high-energy electrons ionise the rest of the material and escape the detector. This leads to increasing energy deposition with higher energy of injected muons. Around 10–20 MeV, a muon, in this particular geometry, deposits all of its kinetic energy, the ionisation rate reaches maximum and the muon is fully stopped inside the detector. At GeV energies and above a clear constant value of deposition is visible in both cases, vertical and 50° zenith angle. These relativistic muons constitute MIPs, they pass through the material and ionise it, loosing the minimal energy and further penetrating outside the detector. Low-energy electrons, in MeV range, are fully stopped inside the detector showing a clear correlation between their incident energy and the energy deposit. However, above a few MeV electrons start to show the same behaviour, as high-energy muons, i.e. a constant ionisation rate with respect to their kinetic energy. In this range, it is not possible to distinguish muons and electrons based on their energy losses. Photons, on the other hand, often do not deposit energy inside a scintillator. To some extent low-energy photons follow the electron response since they photo-produce an electron or up-scatter it to the higher energy state. At the lowest energies photo-electric effect dominates over Compton scattering and deposits more energy, what is visible as a separate band. At the highest energies photons start to produce $e^{\pm}$ pairs. One can see that vertical and inclined particles exhibit the same shape of the response. However, in case of an inclined particle direction the median deposition at the highest energies is larger. It means that in this range, only the length of the track within the material influences the sum of deposited energy, which in turn depends on the particle direction. Some of the discussed features of the particle response in this particular scintillator material are also seen by other studies [150].

An important fact to notice is that after translating these energy deposits to the normalisation value from vertical muons (as explained in the next sections), the approximate minimum deposition of energy, which is taken into account, is at the level of 0.8 MeV. Recalling Figure 3.6 with particle spectra obtained from CORSIKA, one can choose the energy thresholds above which particles still contribute to the signals. In case of muons, the lowest possible cut has been chosen since the detector is still sensitive at these energies. For electrons and photons a value of 0.1 MeV was chosen, since below that value the detector is not any more sensitive to these particles. In principle, the cuts on photons and electrons could be safely increased and

---

[5] This study was performed in cooperation with Fiona Ellwanger

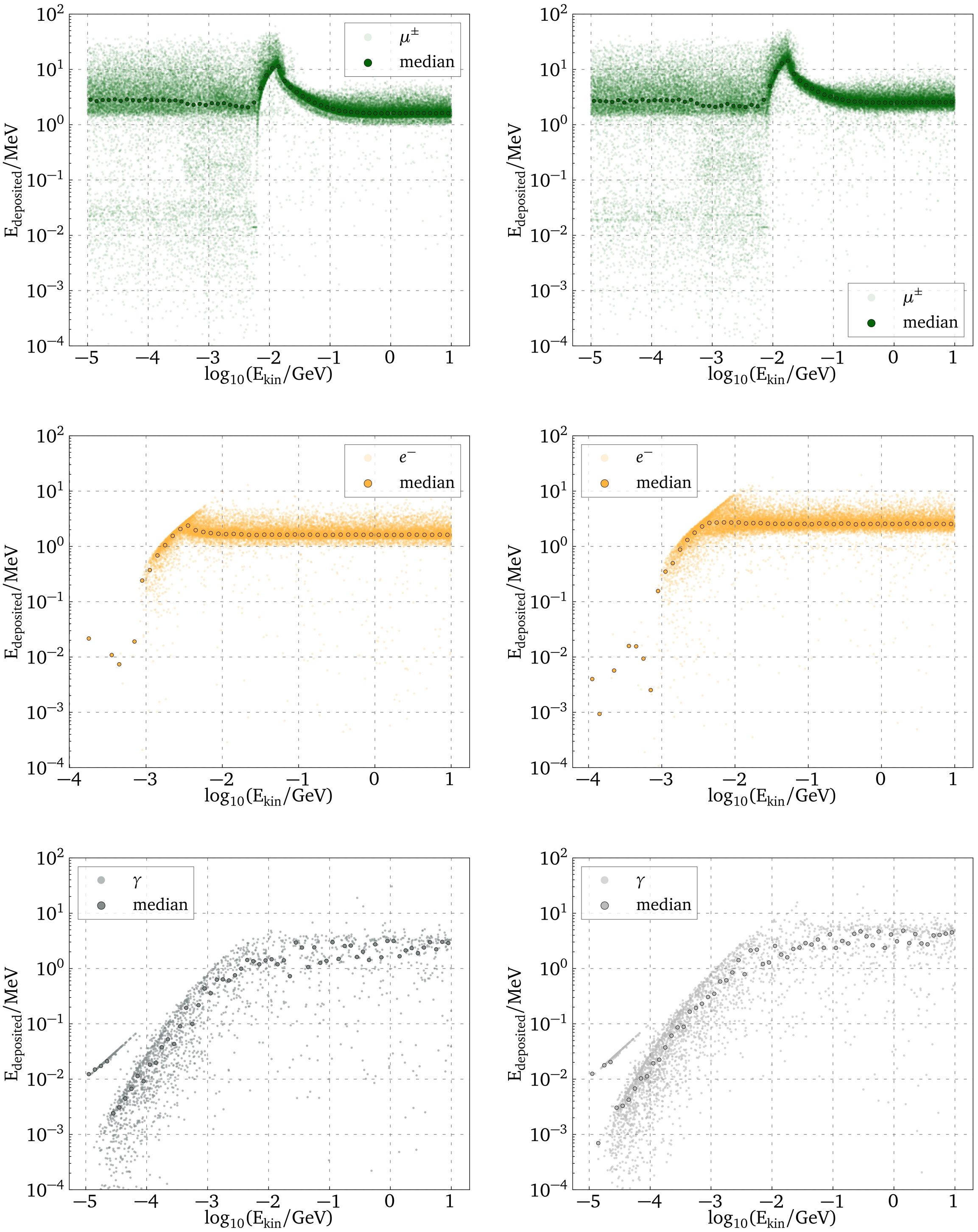

Figure 3.10: The energy deposited in the scintillation detector from different incident particles with zenith angles 0° (*left*) and 50° (*right*). The faded colors represent single energy deposits, while the vivid colors their median values in the incident-energy bins. See more details in the text.

the cuts on hadrons should be studied in more detail. However, for future simulations of the hybrid extension of IceTop, not only using scintillation detectors but also radio antennas, the influence of further cuts on the electromagnetic component has to be evaluated.

Position-dependent parametrisation

In the real detector setup, the scintillation light is guided via the wavelength-shifting fibres connected to the SiPM. They will significantly influence on the final signal output due to their limited reflection capabilities resulting in a loss of photons. However, similar to the case of Cherenkov tank simulations, the photon tracking is very CPU-intensive. Therefore a limited number of simulations with vertical muons was generated to parametrise the efficiency of photon propagation through the fibre, as well as the arrival-time delay at the SiPM. For these special simulations the above-mentioned geometry was additionally elaborated. This work was done in a stand-alone Geant4-based simulation and was performed by [151].

The scintillation-detector model was supplied with 1 mm diameter multi-cladding wavelength-shifting fibres from Kuraray Y-11(300)M, which provide a high light yield and a long attenuation length [152]. The main properties of the fibre are shown in Table 3.3. The fibres cross a single scintillator bar twice and are further connected to the SiPM as presented in left part of Figure 3.11. Tracking of the optical photons in the fibres was performed using a special extension of Geant4 - GODDeSS (Geant4 Objects for Detailed Detectors with Scintillators and SiPMs) [153], which allows for more exact simulations of the optical processes inside a detector. The ends of the fibres are connected to the SiPM coating with the SiPM sensitive volume via a layer of optical epoxy cement, EJ-500, with a refractive index of 1.57 [154]. After propagation through the fibres, the number of optical photons which hit the SiPM sensitive volume is recorded.

The parametrisation of a single-detector output was performed using simulations of verti-

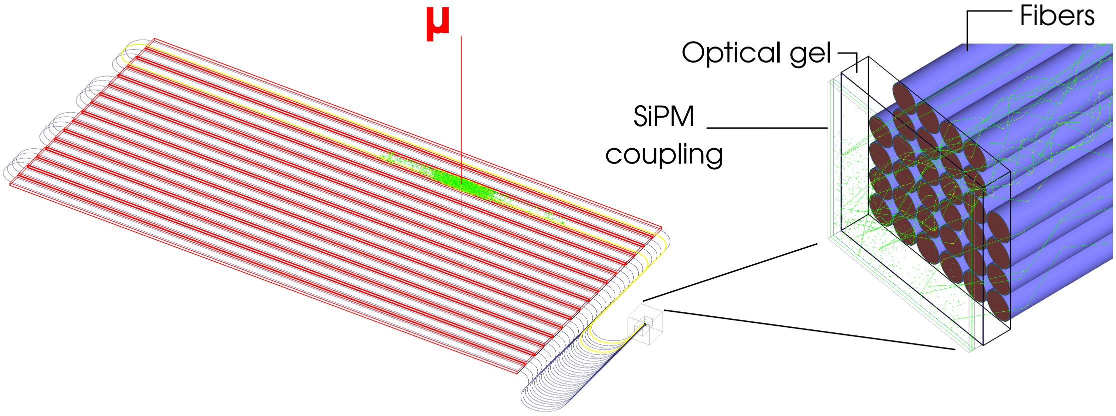

Figure 3.11: *Left:* Scintillation detector model with multi-cladding wavelength shifting fibres included in GODDeSS simulations [155, 151]. Figure is taken from [155]. The injection trajectory of a vertical muon is shown as the vertical red line and the created optical photons are in green (also propagated to the SiPM on the right). *Right:* Model of SiPM and fibre coupling. The SiPM sensitive area is shown in green, SiPM coating in blue and the optical gel in black.

Layer	Material	Average refractive index	Density
Fiber core	Polystyrene (C_8H_8)	1.59	1.05 g/cm^3
Inner cladding	Poly(methyl methacrylate) - PMMA	1.49	1.43 g/cm^3
Outer cladding	Polymer	1.42	1.19 g/cm^3

Table 3.3: Properties of the WLS fibres components used in GODDeSS simulations.

cally injected muons. The particular energy of 3 GeV [6] corresponds to the most probable region in the muon spectrum from CORSIKA simulations depicted in Figure 3.12, with the zenith angle limited to $\cos(\theta) \geq 0.98$. The spectrum was weighted according to the mass group and energy of its parent cosmic-ray, obtained from the Global Spline Fit [81] mentioned in Chapter 1.

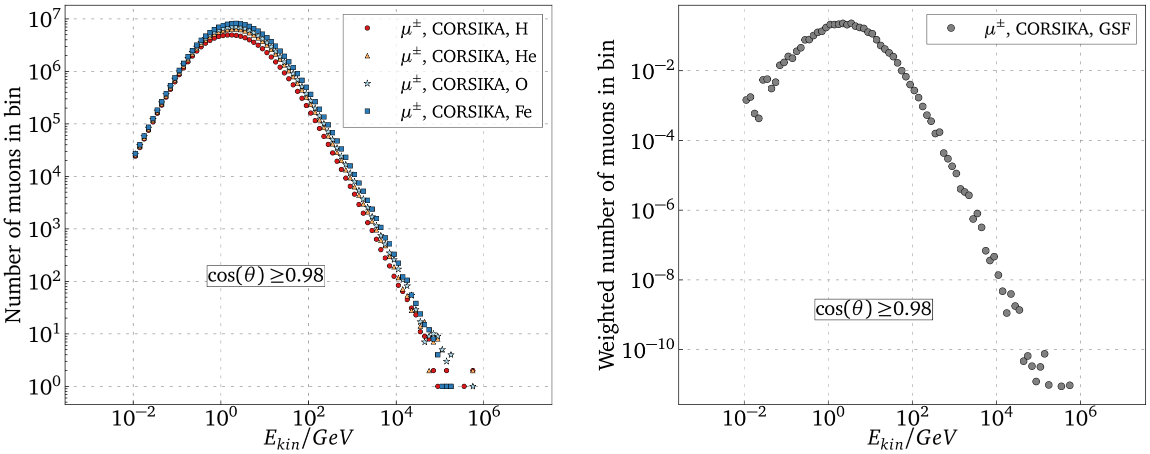

Figure 3.12: Quasi-vertical muon spectra for primaries with energies of $10^2 - 10^7$ GeV. *Left*: For H, He, O, Fe primaries separately. *Right*: Weighted according to the GSF model [81] for H, He, O, Fe where O was taken as CNO and MgSi groups.

Muons were injected uniformly over the scintillator surface. The number of created photons and their distribution at the SiPM is shown in Figure 3.13. The SiPM is mounted on the right side of this scan. The number increases as the photon injection takes place closer to the SiPM, which is connected to the shorter propagation distance through the fibres. Additionally, photons can escape the scintillator more easily at the end of bars, which is also visible in the figure. The upper plot shows the average amount of scintillation light with respect to the muon interaction point along the x-axis of the detector. The parametrisation has the form of Equation 3.3.

$$k_{\text{fibre}} = \begin{cases} k_1 \Delta x + k_2(\Delta x - x_0)^2 + C & \text{if} \quad \Delta x < x_0 \\ k_1 \Delta x + C & \text{if} \quad x_0 \leq \Delta x \leq x_1 \\ k_1 \Delta x + k_3(\Delta x - x_1)^2 + C & \text{else,} \end{cases} \tag{3.3}$$

where Δx refers to the position along x-axis relative to detector centre. k_{fibre} is the correction coefficient to the number of photons calculated initially from Equation 3.2: $\widetilde{N}_{scint} = k_{\text{fibre}} N_{\text{scint}}$.

---

[6] Test with the range of energies following the muon spectrum was performed and gives similar results within the error bars.

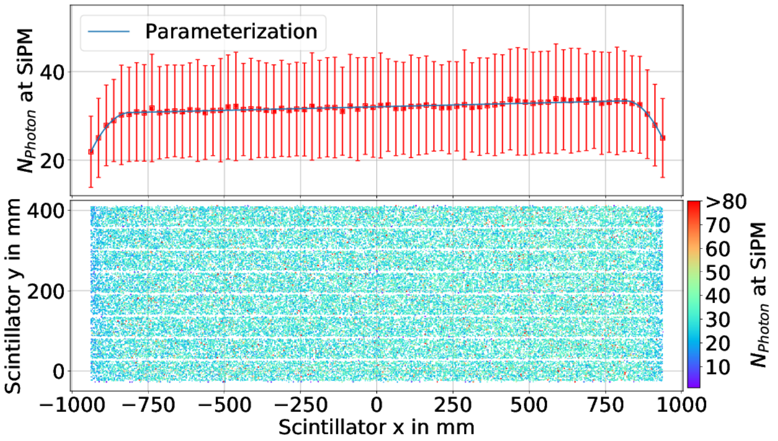

Figure 3.13: *Upper:* Mean number of photons in each slice of the lower plot. Plot is taken from [151, 155]. The uncertainty represents the standard deviation. *Lower:* Number of photons over the muon hit position along the detector.

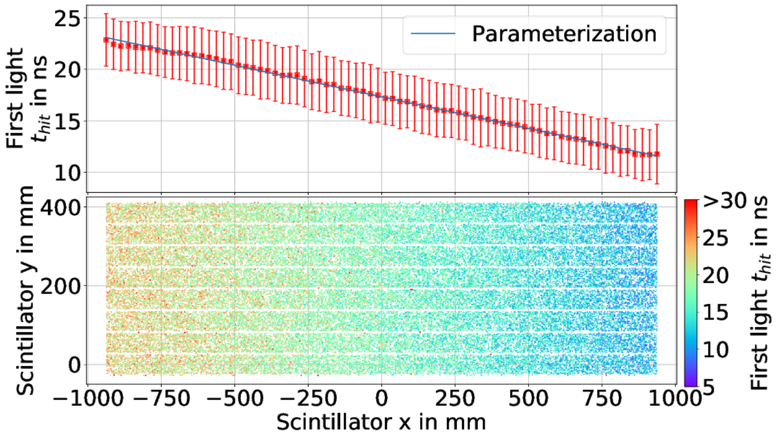

Figure 3.14: *Upper*: Mean time of first photon in each slice of the lower plot. Plot is taken from [151, 155]. The uncertainty represents the standard deviation. *Lower:* Scatter plot of the first detected light over the muon hit position along the detector.

One of the features of plastic scintillators is the fast rise time of the main light output which decays exponentially: $I(t) = I_0 e^{-t/\tau}$. Here τ is the decay time and I_0–the initial light intensity [122]. The second light component, mentioned in section 2.3, will be delayed and contribute to the total intensity curve as a less intense second decay. In the case of the chosen scintillator material, the decay time is 3.3 ns and the rise time is 0.9 ns for the fast component [156]. However, the arrival time of single photons to the SiPM is not only influenced by the light decay but also by the propagation inside the fibres. This propagation was parametrised using the above-described vertical muon simulations. The time delay between a particle crossing the detector and the first photon arriving at the SiPM is shown in Figure 3.14. As expected, the arrival time delay is shorter the closer to the SiPM an interaction takes place. When a particle hits the detector close to the SiPM, the average time delay is around 9 ns, and on the opposite side around 20 ns. The time of a single photon, obtained from this parametrisation, is described by Equation 3.4.

$$t_{hit_i} = t_i + a_0 \Delta x + a_1, \tag{3.4}$$

where t_i is a time when a simulated particle crosses the detector.

Vertical muon normalisation

As described in the previous sections, the Geant4 simulation provides the energy deposit within a sensitive volume. The number of generated photons is further calculated and their attenuation in the fibre is taken into account. The final step is the simulation of the photodetector, in our case the SiPM. This requires the time distribution of single PEs arriving at the position of the SiPM. The information about the number of generated PEs can be derived from the measurements from the muon tracking detector at KIT [157]. An example of the charge spectrum obtained from one of the prototype detectors can be seen in Figure 3.15. Based on the peak position of the charge, the resulting number of PEs can be calculated taking into account the SiPM and the electronic gain of a scintillation detector system. An average value is obtained from the measurements of 22 detectors and equals $\mathrm{N_{VMIP}} = 40$ PEs/VMIP [158].

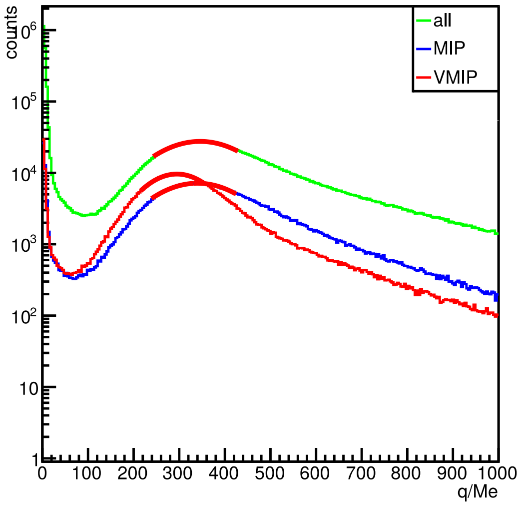

Figure 3.15: A charge spectrum built from a prototype detector data. The panel was scanned in the muon tracking tower at KIT, which can determine the direction of the incoming particle. The plot is taken from [158]. Red line shows the spectrum build from vertical MIPs and blue one from all MIPs.

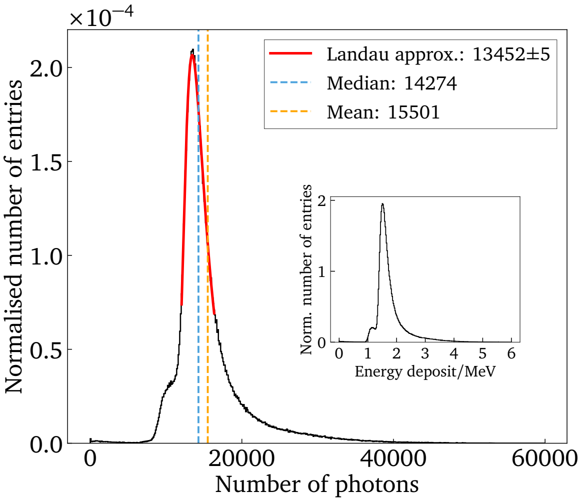

Figure 3.16: Number of generated photons produced in the simulations of 3 GeV vertical muons traversing a scintillation module and randomly distributed across the detector. Their energy deposit is depicted in the inner plot. The parametrisation of Landau distribution is used to estimate the peak value.

In the simulations, the conversion factor from the number of generated scintillation photons to VEMs is obtained. The 3 GeV vertical muons were randomly injected across the detector. The obtained reference value, $N_{\mathrm{ref}} = 13452 \pm 5$, is defined as the peak of the Landau distribution parametrisation [159], shown in Equation 3.5, partially fitted to the spectrum of the generated photons as presented in Figure 3.16.

$$\delta N(x) = \frac{N}{2\pi} \exp \frac{-(\lambda + \exp(-\lambda))}{2}, \qquad \lambda = \frac{x - \mathrm{MP}}{\eta}, \tag{3.5}$$

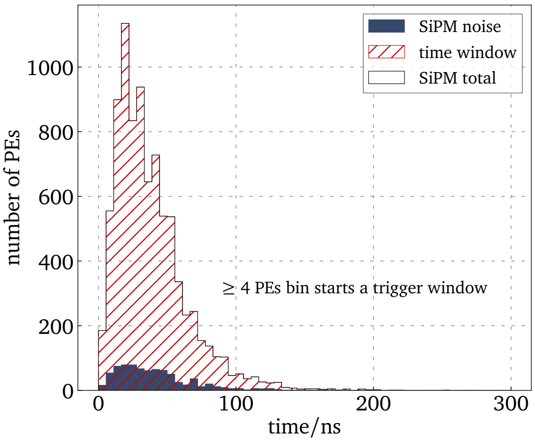

Figure 3.17: Time series of PEs arriving to SiPM with convoluted, simulated SiPM noise marked in blue. Majority of noise PEs originates from SiPM cross talks. A hatched region indicates a time window used in simulation to sum up PEs contributing to a signal.

where MP is the most probable value. The corresponding energy deposit is shown in the inner plot. The small peak on the left side is caused by the simulated air holes, which in reality contain the fibres. The final value is based on the number of generated photons, N_{scint}, which is taken as:

$$N_{\text{PE}} = \frac{N_{\text{scint}}}{N_{\text{ref}}} \cdot N_{\text{VMIP}}. \tag{3.6}$$

Simplified response of electronics

The number of photons generated by every particle is then converted to PEs, assuming that 1 VEM = 40 PEs based on the measurements from the muon tracking detector and from the prototype station at the South Pole. For each PE, a signal decay is added to t_{hit_i} by randomly choosing a value from an exponential distribution with $\widetilde{\tau} = 23.4$ ns, which is the mean decay time obtained from detailed simulations [151]. This creates a list of PE arrival times. A corresponding histogram of PE times, with 1 ns bin width, is passed to the SiPM noise simulator. The SiPM response was simulated with the G4SiPM simulation package [160] only for the detailed parametrisation. At this stage only module simulating SiPM noise is applied. This simulation module folds PE time-series with the electronic noise, such as thermal noise, afterpulses, and crosstalk with a random jitter applied. The most significant noise source are the SiPM cross talks. The crosstalk probability at SiPM is set in simulation to 9%, which is at the level of the measured value of 8.4% [117]. Therefore, the overall noise level constitutes less than 10% of the total signal. An example of this final simulated time series is shown in Figure 3.17 for a single detector signal. Since the behaviour of the electronic system is not included in the simulation chain, an idealised trigger module is applied. Similarly to what is done currently in the μDAQ system, it divides the arriving PEs in 5.55 ns bins and checks if at least 4 PEs are detected in the first bin (as marked in Figure 3.17). If this is the case, all PEs within a $5.55 \cdot 36 \approx 200$ ns time window are summed up. Although the prototype detectors are configured at the moment with $5.55 \cdot 18 \approx 100$ ns time window, this trigger time will be increased for the installation of the full array. The summation of PEs is an approximation of the μDAQ behaviour, which integrates the single PEs distribution and not the SiPM signal directly [161].

While the series in a left plot of Figure 3.18 is short enough to be fully integrated into the final pulse, the one in the right plot is cut. The series come from the same air shower, however the one which extends longer in time originate from a detector placed more than 200 m away from the air-shower's impact point on the ground. Contributions from different particle species reveal that late PEs are due to single late particles. PE series from 200 air-showers are shown in Figure 3.19 for proton and iron primaries. One can see that the great majority

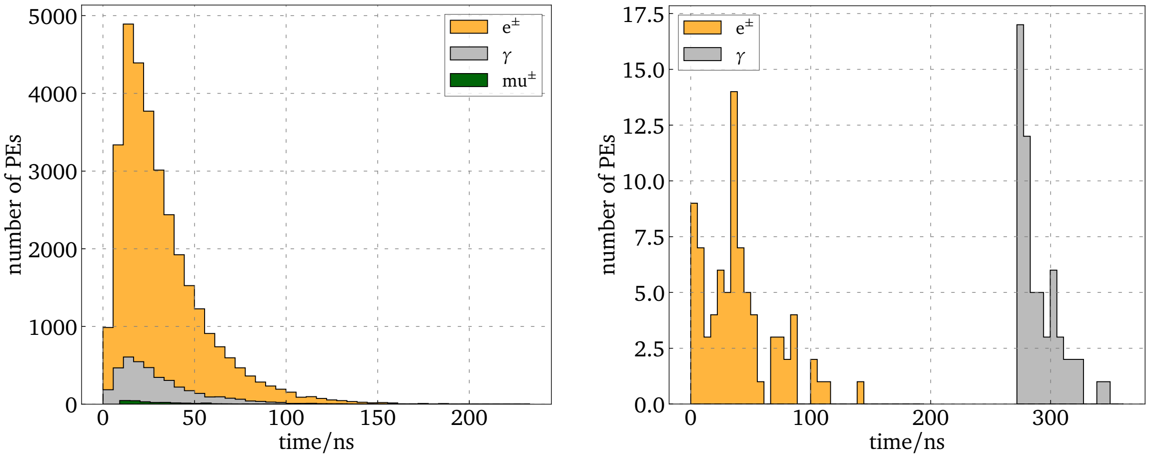

Figure 3.18: Time series of arriving PEs from an air-shower initiated by proton of 34° zenith. Left: Series from a detector located ∼ 12 m from the shower core. Right: Series from a detector located ∼ 235 m from the shower core. Colours indicate different particle species.

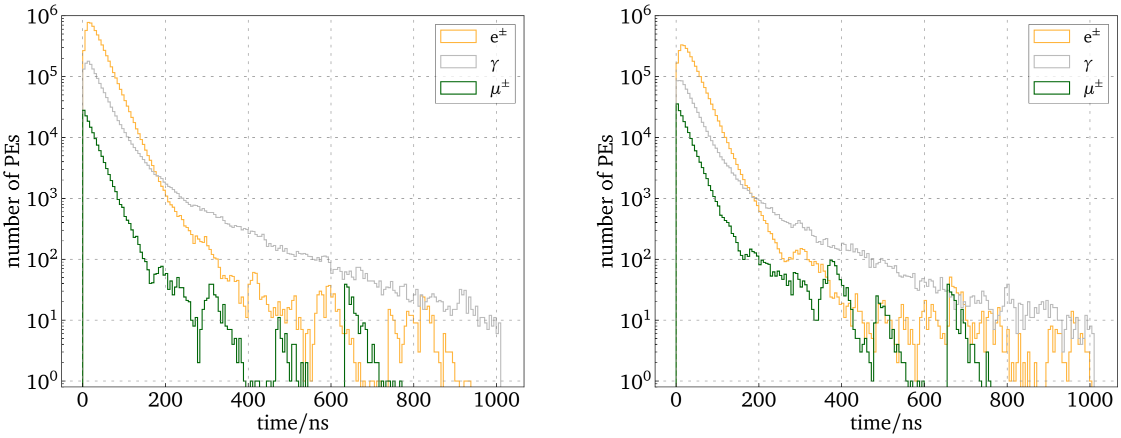

Figure 3.19: Times of arriving PEs from 200 air-showers initiated by proton (left) and iron (right) with zenith angle ranging from 0° to 50°. Colours indicate different particle species.

of signal arrive within the mentioned 200 ns. However, there is also not completely negligible contribution from 200 ns to 400 ns, which shows a different ratio of electromagnetic and muonic components for iron- and proton induced air-showers. Timing information which separates secondary species could be potentially used for a more advanced discriminant analysis in order to distinguish primary species. Therefore for the future firmware settings of the DAQ system an extended integration time should be considered.

MIP calibration

In reality an acquired signal will strongly depend on detector-specific properties which may change with time and vary between detectors. As it was already mentioned, a calibration using atmospheric particles is often applied. Above a certain energy muons and electrons (also electrons from γ interactions) ionise the traversed matter with a nearly constant probability. MIPs leave a distinct peak in the charge spectrum seen by the free-running scintillator module as presented in Figure 3.20. The position of this peak will be used to calibrate the

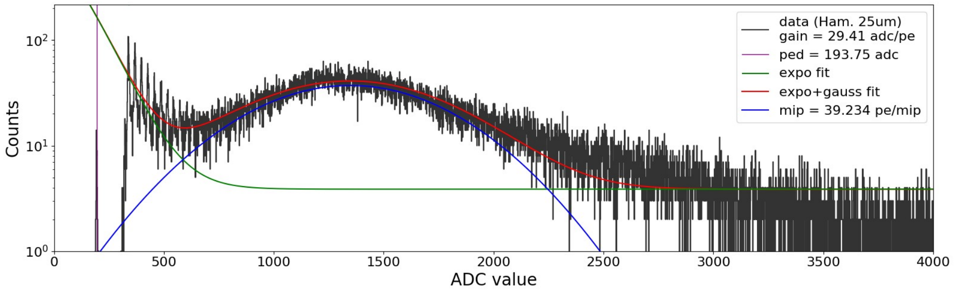

Figure 3.20: Charge spectrum measured in ADC counts by a μDAQ-based detector [16]. The measurements were performed with the high-gain ADCs settings. The distribution is well described by an exponential plus Gaussian function.

detectors.

A corresponding charge spectrum was simulated using low-energy air-showers which are the main source of MIPs. The simulations for H, He, O and Fe primary cosmic-rays were performed, with energy ranging from 1 TeV to 100 TeV with zenith angles up to 50°. Air showers were re-sampled 10 times within 500 m radius from the center of the array (see details of the array layout in the next chapter). The obtained signals were weighted according to the GSF model [81]. The simulated PE spectrum is shown in Figure 3.21. Only signals above 4 PEs threshold were taken into account. The mean value of the Gaussian-distribution fit results in the calibration constant of 53 PEs. The shapes of the spectra differ due to the particular settings of the DAQ system. A high-gain mode allows for an amplification of a region around the MIP peak, rejecting larger signals. An example of a medium-gain measurement can be seen in Figure 3.22. This spectrum roughly matches the simulated distribution, which does not include an actual characteristics of the electronic system. This can be seen as the first peak in the data spectrum. Moreover, the simulated and the prototype panel readout for these plots differed in geometrical details, which influences on the amount of generated photoelectrons.

In the simulations, however, the reference value $\mathrm{N}_{\mathrm{PE}_{\mathrm{ref}}} = 43$ PEs was used to convert all following simulation results to the reference unit VEM. The value of 43 PEs is lower than the MIP peak and is closer to the response of single vertical muons. The exact calibration procedure should be established in accordance with the commissioning data and verified. If VEM unit remains to be used then the according fraction of the MIP peak has to be selected from the data.

The minimum threshold for data acquisition is at the level of 0.1 MIP. However, in the simulations a conservative value of 0.5 in VEM unit is assumed, to account for the electronic performance which needs to be determined. If the DAQ chain is fully understood in the simulations, this value can be changed to the level, which minimises the coincidental noise-hits. On the other hand the photodetector and electronic system experience an effect of saturation. Above certain deposition in the panels, no more linear correlation between light and output signal is expected. This needs to be determined, thus in the simulations an upper signal threshold of 1000 VEM is assumed.

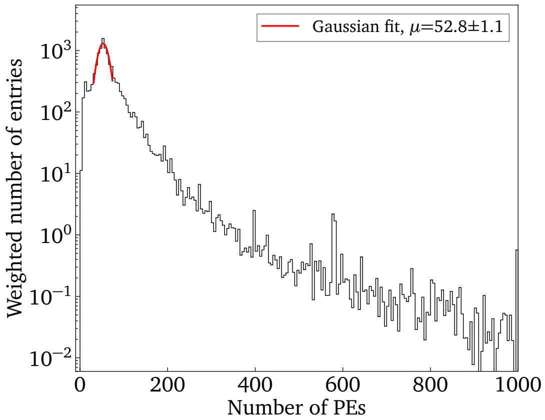

Figure 3.21: Simulated PE spectrum using low-energy air-showers weighted according to GSF [81]. The peak of this spectrum is used as a reference for the simulated signals.

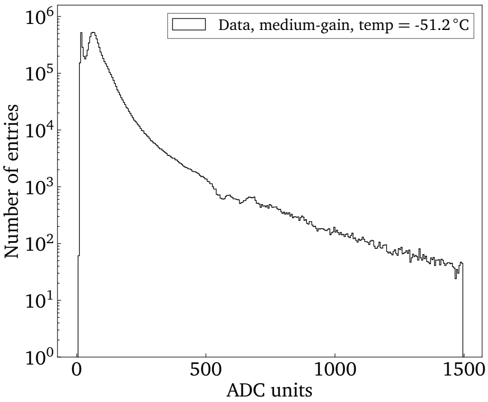

Figure 3.22: Charge spectrum measured in ADC units by μDAQ-based detector [162]. The measurements were performed with the medium-gain ADCs settings.

Chapter summary

Merging all steps described in this chapter, the software basis for the large-scale simulations is established. It is, on the one hand fast for the future production of a large library of simulated air showers. On the other hand it is precise enough to obtain correct information about the air-shower observables. Different software modules created for these simulations are already integrated in the IceCube software and undergo constant development to reduce the amount of possible errors and to provide code transparency and high flexibility to the users.

Chapter 4

ARRAY SIMULATIONS

The IceTop array can detect cosmic rays from PeV to EeV energies. This range covers a very pronounced feature of the cosmic-ray spectrum, the knee, where the spectrum significantly changes in steepness. The position of the knee, at around 3 PeV, can be qualitatively described by a model where the acceleration power of the Galactic supernova remnants is exhausted, as mentioned in section 1. Somewhere above the knee, the transition from Galactic sources of cosmic-ray acceleration to extragalactic sources is expected to occur. Recently, IceTop and other experiments have revealed more structures in the cosmic-ray spectrum in this energy range [86]. However, to interpret them in the context of their astrophysical origin, a more detailed investigation has to be performed above and below the knee. The KASCADE experiment has experimentally proven that the knee originates from a decrease of light-mass cosmic rays, shedding light on the spectral features being a result of a rigidity dependent cut-off. Thus, precisely dissecting the all-particle spectrum to individual-component spectra can possibly clarify the nature and properties of the sources. Therefore, it is of a great importance to boost the IceTop capabilities towards better mass discrimination on event-by-event basis, and at the same time reducing the measurement uncertainties on both, cosmic-ray energy and mass around the knee.

Furthermore, using the in-fill part of IceTop, it is possible to reconstruct the cosmic-ray spectrum as low as 250 TeV [163]. This lowering of the detection threshold brings the spectrum close to the energy region where direct measurements of cosmic rays are possible. The space- and balloon-based experiments can currently detect light-mass primary cosmic-rays up to 80 TeV [60]. However, to verify the spectral structures and, most importantly, the absolute scale of the cosmic-ray spectrum (which is more uncertain for the ground-based experiments), an overlap between these two distinct detection classes would be desirable.

The above goals can become more reachable with future hybrid measurements from IceTop (and its enhancement) and IceCube; in particular, an addition of scintillation detectors and radio antennas distributed over the IceTop footprint. The new surface detectors increase the number of the air-shower sampling points and provide a sensitivity to different air-shower components with respect to the existing Cherenkov tanks. Moreover, merging the information from surface-detectors and in-ice array can further resolve the cosmic-ray properties as it was already shown in [104]. Installing a detector of a new type will therefore increase the ability to determine cosmic-ray species.

Besides this, the important task which the surface enhancement should fulfil is an improvement of the atmospheric-background rejection for the astrophysical neutrino searches. This will be the first stage towards the large surface veto-array for the next-generation of IceCube.

In the scope of this thesis, only the simulation results for the scintillator array are presented.

However, broad studies have been performed on radio simulations for the IceTop enhancement separately [164, 106].

4.1 Optimisation of the array layout

Geometrical considerations

For any ground-based array, the distribution of the detectors is a key factor which determines the sensitivity to the experimental objectives, and connected to that – the parameters for the data analysis.

(a) All particles

(b) All particles

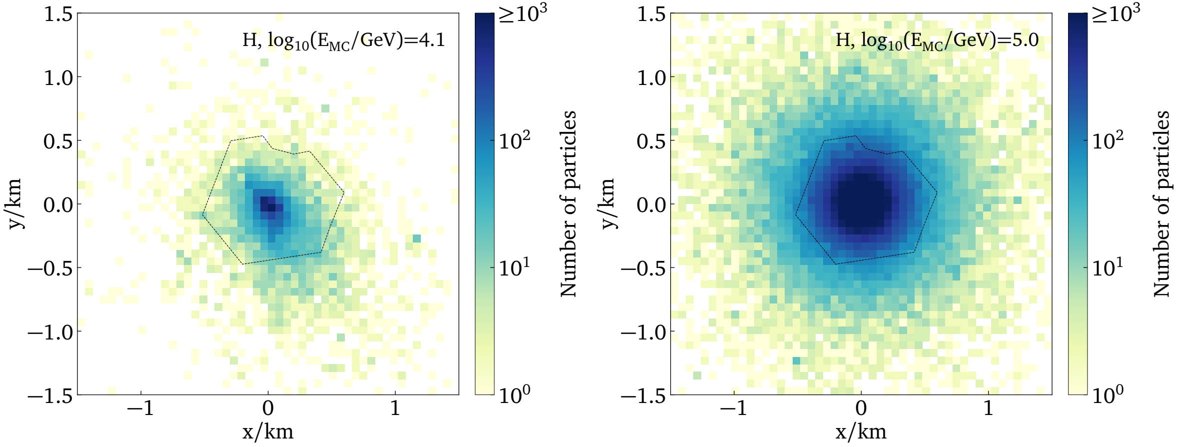

(c) Excluding photons

(d) Excluding photons

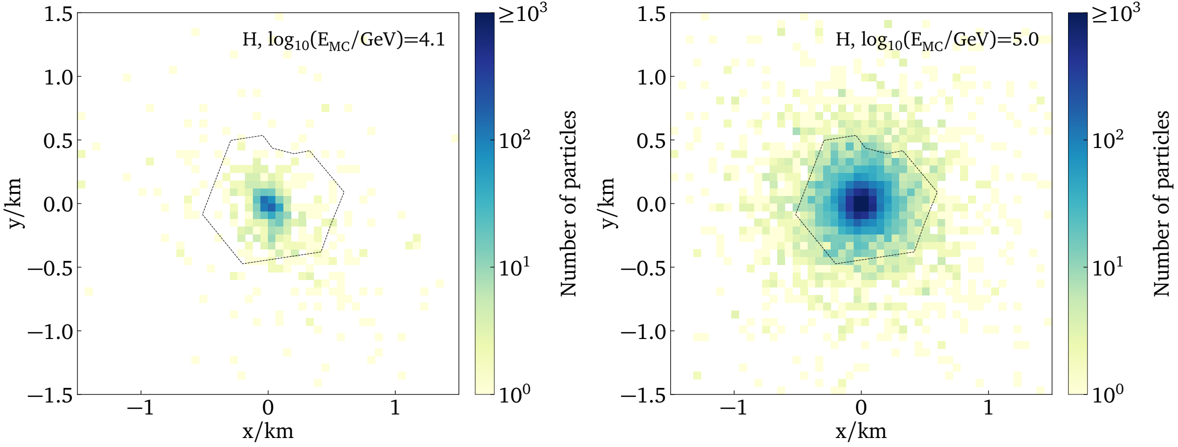

Figure 4.1: Distribution of the number of air-shower particles arriving at the South Pole observation level (2842 m a. s. l.). Air showers were initiated by a proton primary with an energy and zenith angle respectively: *a*, *c*: $10^{4.1}$ GeV, 46°; *b*, *d*: 10^5 GeV, 14°. The upper plots show all particle types from the CORSIKA output, while the lower plots exclude photons. It can be seen that the size and density of the footprint is mainly determined by photons, which on the other hand often do not leave a signal in the scintillators.

In the case of the discussed scintillator array, on the one hand, the planned detector has to fulfil the requirements given by the mentioned scientific goals, which in terms of detector layout mainly means lowering the energy threshold. To achieve the detection threshold on the level of a few hundreds of TeV, the arrangement of the new detectors has to be denser than the current Cherenkov-tank spacing, which is around 125 m. This is necessary to increase the number of sampling points over the relatively small air-shower footprint. The two such exemplary footprints of the air-showers induced by protons with energy ≈10 TeV and 100 TeV, respectively, are presented in Figure 4.1. The depicted border lines roughly indicate the edges of IceTop. The bin-width of the 2-dimensional histogram of the number of particles is 60 m. The scintillation-panel design provides an active area of 1.5 m^2 (see section 2.3). Assuming that such a bin has two detectors of 1.5 m^2 active area, 1000 particles arriving at this bin result in ≈80% probability of a particle crossing the detection area. Applying this idealistic consideration, at least three such bins are needed to detect a shower, a rough geometrical reconstruction of the core and direction of the incoming cosmic ray needs at least three points. In this case, 100 TeV shower (right plots) could be detected with quite high probability, while the 10 TeV (left plots) with much lower probability due to significantly smaller footprint. Taking into account a single-detector response will further worsen these effects, especially, since the majority of secondaries are photons which have a rather low probability of leaving a significant energy deposit inside scintillation module (as shown in Figure 3.10). The footprints, excluding photons, are presented in the lower panels of Figure 4.1. Clearly, to effectively target a detection threshold of hundreds of TeV for the air-showers contained within the array, a spacing between the modules of the order of 50–100 m needs to be considered for the subsequent simulation analysis.

In addition, the detector deployment at the South Pole entails a few logistical challenges. Only a limited number of modules can be installed in a deployment season, given the detector size and weight which are restricted to be carried by two people. Moreover, all power-cabling lines at the IceCube site need to be connected to the tower of the IceCube Laboratory, with all detectors attached to these lines. Due to the specific Antarctic regulations, these lines need to be first trenched to secure the cables. Such trenching requires a considerable labour input and therefore should be optimised to a feasible length. This in turn becomes a limiting factor for the arrangement of the detectors. Thus, it is crucial to understand if a very distributed layout can bring a significant decrease in the threshold for cosmic-ray detection. Otherwise the more optimal spacing could simplify and shorten the deployment.

Studied layouts

Several different layouts of the scintillation modules were proposed taking into account described scientific and logistical conditions [165]. Their responses to the air showers were simulated. Air showers initiated by H and Fe primary cosmic-rays with energies ranging from 1 TeV to 10 PeV were simulated. The zenith angle ranges from 0° to 50°. Every air-shower obtained from CORSIKA was sampled 20 times within a 500 m radius from the center of the IceCube-surface coordinate system and propagated through the array response (see details in Chapter 3). A sample of the core distribution over the array can be seen in Figure 4.2. The events with the impact point at the edges of the array will not be well-contained for further reconstruction, in particular in the case of some of the analysed layouts. Therefore for the comparison of the detector arrangements, only air-showers with a core position within 450 m from the center are analysed, as marked in Figure 4.2.

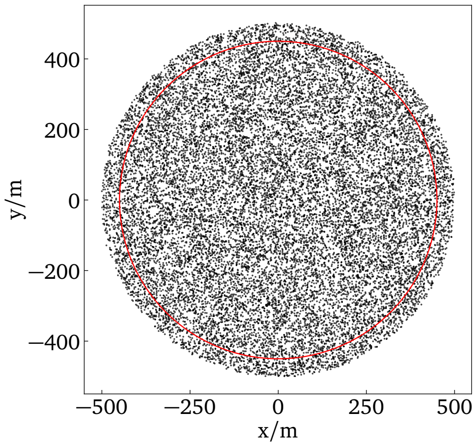

Figure 4.2: An example of core distribution over the array. Red circle indicates 450 m radius for the selection.

To understand the detection efficiency of a particular layout, a 3-fold-coincidence condition was applied. The air shower is considered detected when at least 3 scintillation modules have signals $\geq 0.5\,\mathrm{VEM}$ arriving together within a $3.5\,\mu\mathrm{s}$ time window, anywhere in the array. A probability to have a false 3-fold coincidence is low when selecting 3 given detectors [113], therefore a simple topological condition with 3 detectors can be applied to significantly reduce the background if required for data taking. The efficiency is defined, per energy-bin, as a ratio of the number of detected and generated air showers in a given energy-bin. The uncertainty on the efficiency points, shown on every plot [166], is defined using Wilson confidence-intervals for a binomial distribution [167], for 95% confidence ($\pm 2\sigma$). For every case, a simple fit to the efficiency points was performed using an error function:

$$p(\log_{10} E) = 1 - 0.5\left(1 + \mathrm{erf}\left(c\left(\log_{10} E_0 - \log_{10} E\right)\right)\right). \tag{4.1}$$

Using Equation 4.1, the threshold value of 98% detection fraction was obtained for every curve.

Layout 37x7

The initially proposed layout, presented in Figure 4.3, was inspired by the hexagonal structure of the IceCube-string distribution at the surface. It provides very uniform distribution of the modules. Due to the geometrical considerations presented above, the spacing in this layout is around 65 m, which is roughly two times smaller than for IceTop. One station comprises of 7 detectors. During the first deployment season, two prototype stations were installed according to this initial arrangement.

A few variations of this layout were also considered, see Figure 4.4.

Layout 37x4

The layout 37x4, presented in Figure 4.4a, was created by simply removing every second outer detector from every station of layout 37x7. It is motivated by intention to reduce the deployment efforts by requiring a smaller number of detectors and therefore a smaller amount of trenching lines.

Layout 18x7

The layout 18x7, presented in Figure 4.4b, represents another way of reducing the initial layout to roughly half, by randomly removing 19 stations. In this case, layout is highly non

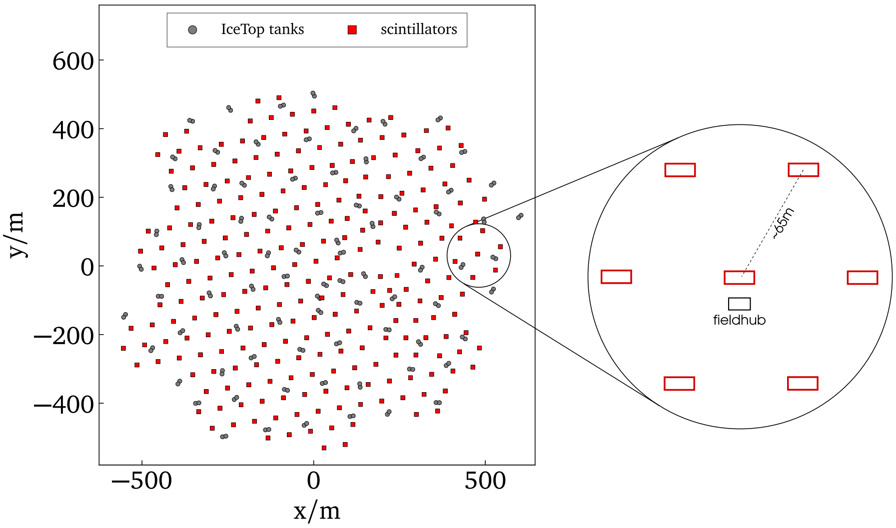

Figure 4.3: The hexagonal layout of the scintillation detectors placed within the IceTop footprint. As shown in the lower scheme, one station is comprised of 7 modules arranged in a hexagon. In this layout, the scintillators are the most uniformly distributed.

uniform what in principle could be an advantage in reducing possible influence from the instrumental effects coming from orderliness.

Layout 37x13

The layout 37x13, shown in Figure 4.4c is, on the contrary, almost doubling the number of foreseen modules. With this idea one can test how significant would be the improvement for such increase of effort. In this arrangement 6 detectors were added to every hexagonal station at around 30 m distance from the inner detector.

Layout 22x7

The layout 22x7, shown in Figure 4.4d constitutes the ring of the outer stations, creating an empty space in the center. This arrangement is obviously not good for standard air-shower measurements. However, it is considered here as a possible triggering solution. Such a ring of detectors could act as a trigger for a more sparse inner array of, for instance, radio antennas. In addition, it could be an additional vetoing ring.

The efficiency curves for the initial layout and its 4 variations are depicted in Figure 4.5 for two ranges of cosmic-ray zenith angle. The 98% efficiency of the 37x7 setup is reached at around 220 TeV for a proton cosmic-ray primary with zenith angles up to 45° and at 130 TeV for quasi-vertical showers. Reducing a single station to 4 detectors increases this almost by a factor of two. Removing 19 random stations increases the threshold to 600 TeV for the broader zenith-range case. This is a significant increase which would not allow for the realisation of the science cases mentioned above, especially that reducing the number of sampling points will worsen the reconstruction performance. Moreover, it essentially removes a possibility to veto low-energy showers or the higher-energy but very deep showers — with X_{max} much below the IceTop elevation. These showers would still produce a high-energy muon possibly leaving a track inside IceCube. Therefore substantial diminishing of the module

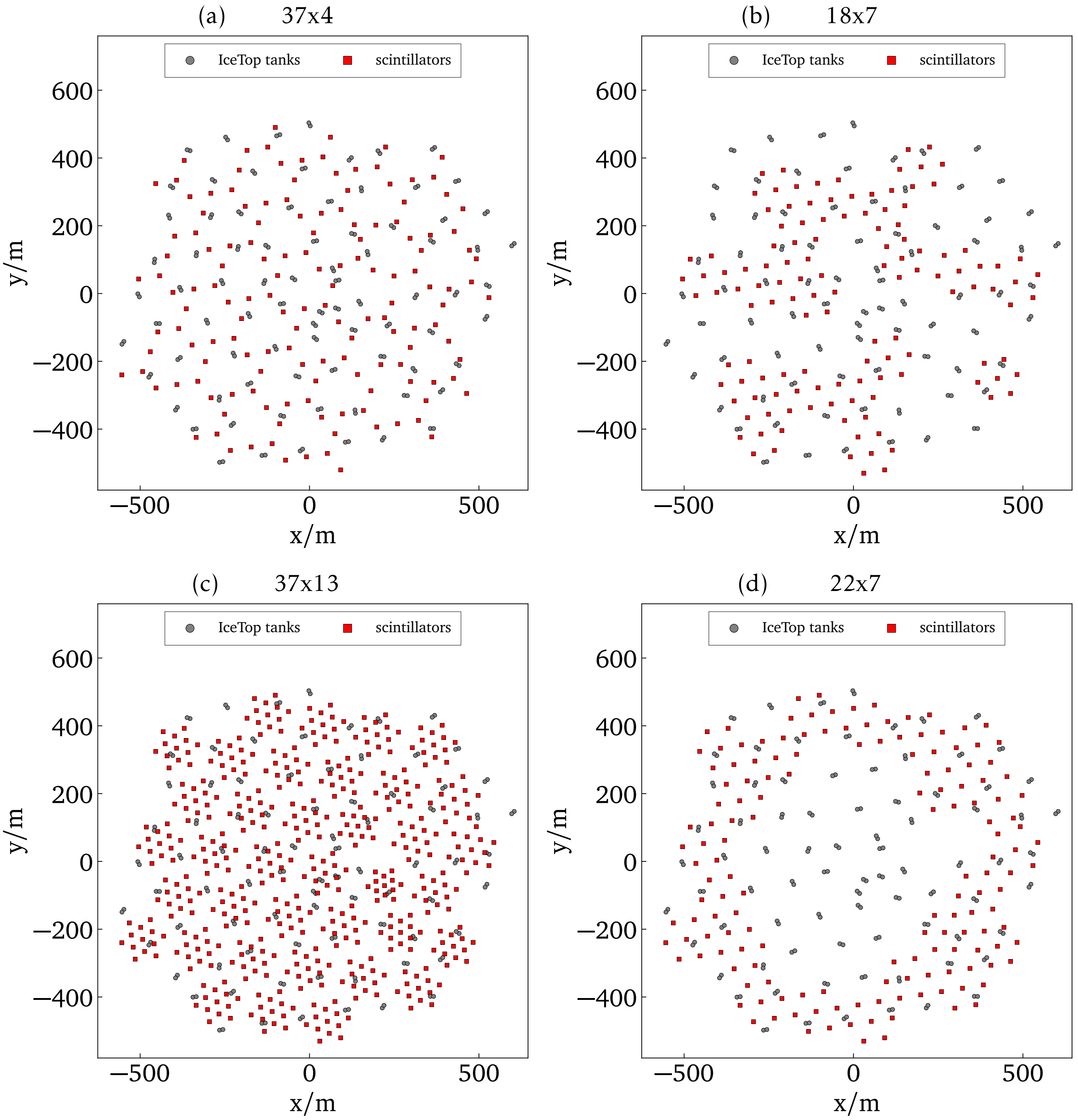

Figure 4.4: A set of scintillation-detector layouts arranged in hexagonal stations. *a:* The station is reduced to 4 detectors per station with 37 stations in total. *b:* The total number of stations is reduced to 18. *c:* The station is extended to 13 detectors per station with 37 stations in total. *d:* The total number of stations is reduced to 22 located only as an outer detector ring.

number cannot be considered for trenching length reduction. On the other hand, almost doubling the scale of each station, from 7 to 13 modules per stations, does not bring a very significant lowering of the detection threshold, ≈ 40%, with a substantial growth of the costs and labour. The layout comprised of an outer ring can efficiently trigger only on air showers in the PeV range. But it is interesting to notice that removing the central stations still allows for the detection of 50% of showers around 100 TeV, which can be a good hint for a future design of IceCube-Gen2 veto-array. Perhaps, arranging detectors in denser rings with sparser inner regions could be efficient for this purpose.

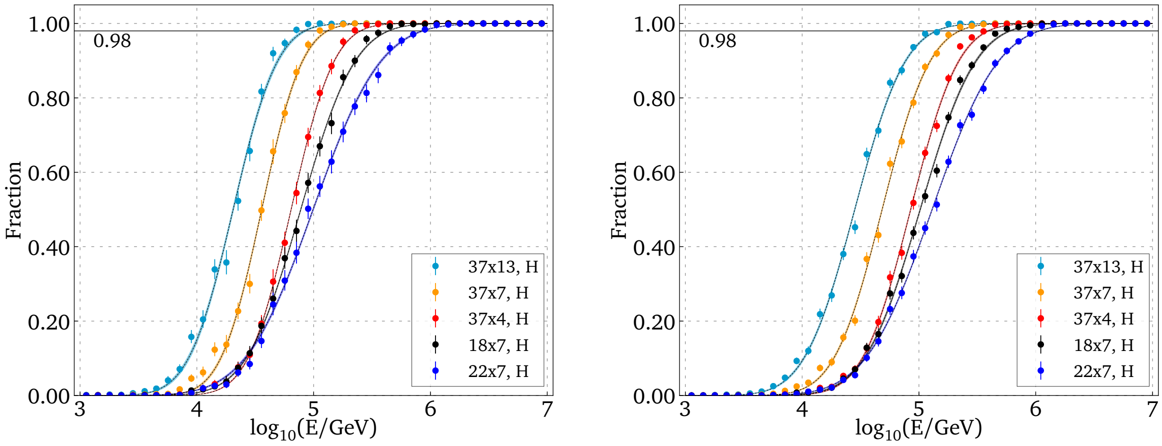

(a) $\theta \lesssim 26°$, $\cos\theta > 0.9$

(b) $\theta \lesssim 45°$, $\cos\theta > 0.7$

Figure 4.5: Efficiency of air-shower detection over the primary cosmic-ray energy for the 5 layouts of the scintillation detectors based on hexagonal station design, as described in detail in the text. Efficiencies are depicted for two ranges of cosmic-ray zenith angle.

Layout 36x8

Another idea for detector layout is depicted in Figure 4.6. It assumes arranging the detectors in pairs and aims to significantly reduce the trenching length required for the distribution of the cables. In this design one station comprises of 8 detectors arranged in a square of 90 m side length. Two modules are placed at a 2 m distance from their centres and are rotated by 90° with respect to each other to provide more uniform coverage.

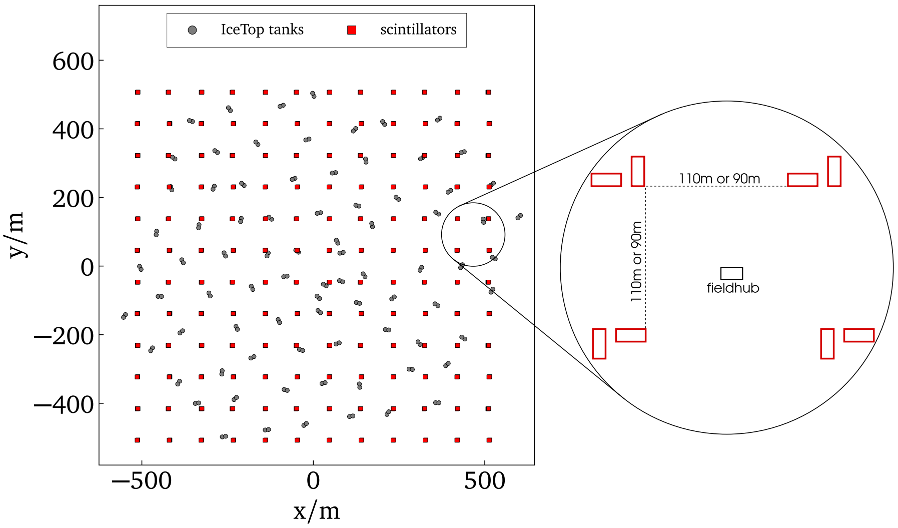

Figure 4.6: The alternative layout of the scintillation detectors slightly exceeding the IceTop footprint. As shown in the lower scheme, one station comprises 4 pairs of modules arranged in square. Placing scintillators in pairs reduces length of cabling lines.

Layout 25x8

This layout 25x8, shown in Figure 4.7b, is also based on square design but with 110 m length therefore there are 30% less detectors.

Layout 32x8

The last studied layout, 32x8, shown in Figure 4.7c, is based on the triangular station design. Two modules are placed 5 m from each other's centres. The orientation of detectors is presented in Figure 4.7c and is such that it increases the uniform coverage of the area. This setup can significantly reduce the deployment efforts. The difference in the trenching length between layout 4.3 and 4.7c is ≈ 10 km, which yields more than a 50% reduction. Moreover the triangular design can be more conveniently implemented among the IceTop tanks in the way that tanks appear in the gaps between the scintillator stations. Such solution will be definitely beneficial for vetoing the background for in-ice measurements.

The efficiency curves for the 3 layouts with detectors arranged in pairs are depicted in Figure 4.8 for two ranges of cosmic-ray zenith angle. The 98% efficiency of the 36x8 setup is reached at around 270 TeV for proton comic ray primaries with zenith angles up to 45°, which is worse than the threshold for the hexagonal 37x7 layout. Reducing the array to 25 stations increases this threshold further to 390 TeV, which is very similar to the case of the hexagonal layout reduced to 4 detectors per station, 37x4. Using a triangular station design one can reach 230 TeV threshold and 140 TeV for quasi-vertical air-showers, what is very similar to the values given by the uniformly spaced 37x7 setup.

Summary of the layouts

The efficiency curves for the above considered layouts were summarised in Figure 4.9. The 98% thresholds are shown for different designs and 3 ranges of zenith angles, showing a clear dependence for each layout. The trend of decreasing threshold with increasing number of detectors can be noticed, with an exception of the 22x7 setup which is only an outer ring of the detectors considered here more as a possible triggering solution.

Both of the studied variants of the design, the more uniformly distributed hexagonal setup and the one which places panels in pairs, can reach the targeted threshold region when a comparable effective area is considered. With overall similar levels of the detection efficiency, it becomes clear that the value of trenching reduction, while still providing a high-accuracy of reconstruction, is a decisive factor. Therefore it has been concluded that the triangular design (see Figure 4.10) will be the planned one for the enhancement of IceTop with the scintillation detectors and radio antennas. Moreover, as it was mentioned, this chosen design was additionally adjusted to be distributed to off-tank regions to increase the uniform coverage of this area with scintillation and Cherenkov detectors.

Realistic positions for the final layout

Due to the simultaneous development of the in-ice upgrade and existing equipment, some parts of the IceTop footprint are not available for the surface operations. Therefore the optimised setup on Figure 4.7c was adjusted to the objects at the IceCube site planned for the next seasons of deployment. As it was mentioned, the core of the IceTop enhancement lies in the hybrid design which merges particle detectors and radio antennas. Thus, 8 scintillation

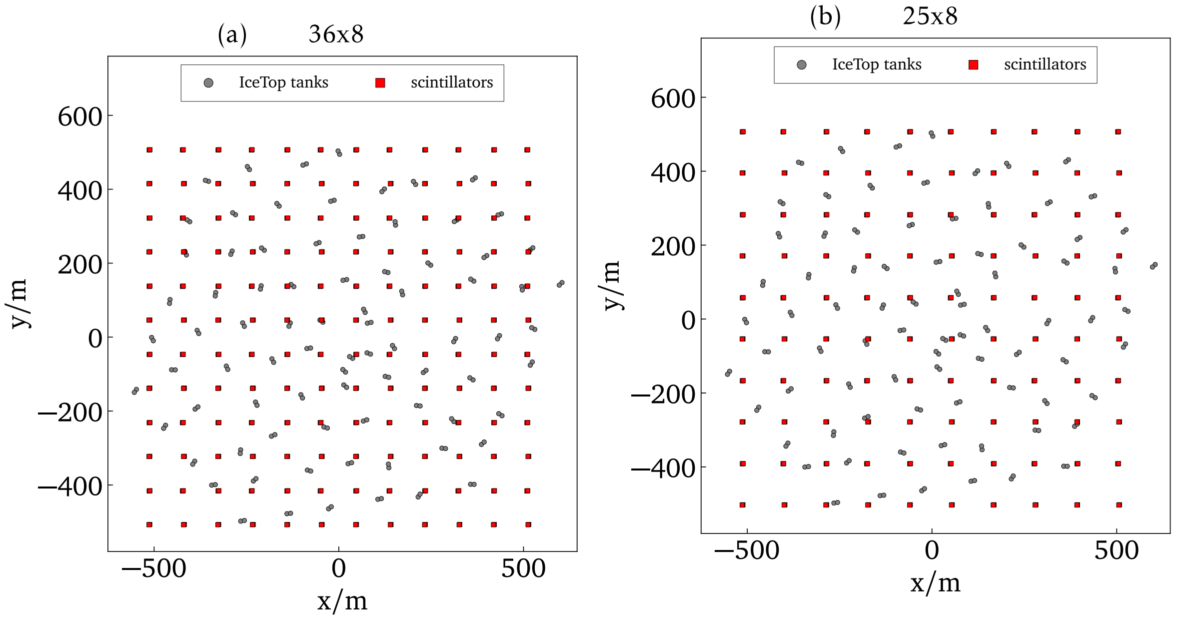
(a) 36x8

(b) 25x8

(c) Triangular layout 32x8

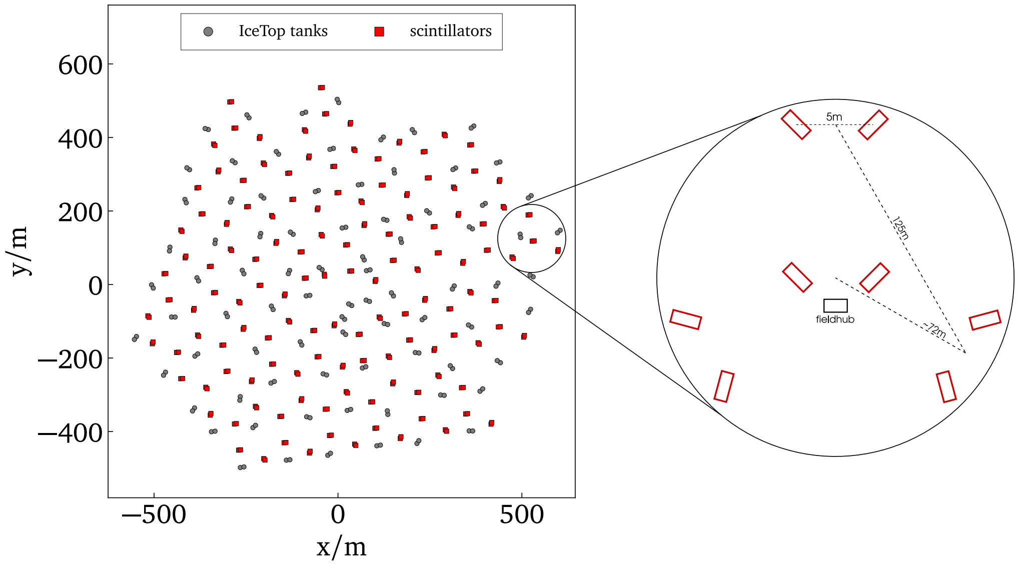

Figure 4.7: A set of scintillation-detector layouts arranged in stations with always two modules placed close to each other. *a:* The square-layout with 8 detectors per station with 36 stations in total. *b:* The square-layout with the number of stations reduced to 25. *c:* The triangular-layout with 8 modules per station with 32 stations in total.

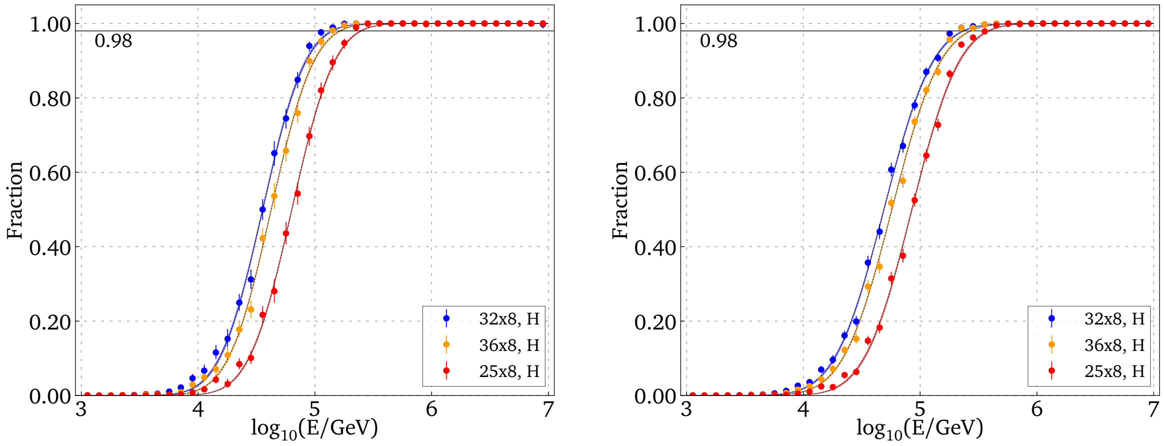

(a) $\theta \lesssim 26°$, $\cos\theta > 0.9$

(b) $\theta \lesssim 45°$, $\cos\theta > 0.7$

Figure 4.8: Efficiency of air-shower detection over the primary cosmic-ray energy for the layout of scintillation detectors and its 3 variations with detectors arranged in pairs, as described in detail in the text. Efficiencies are depicted for two ranges of the cosmic-ray zenith angle.

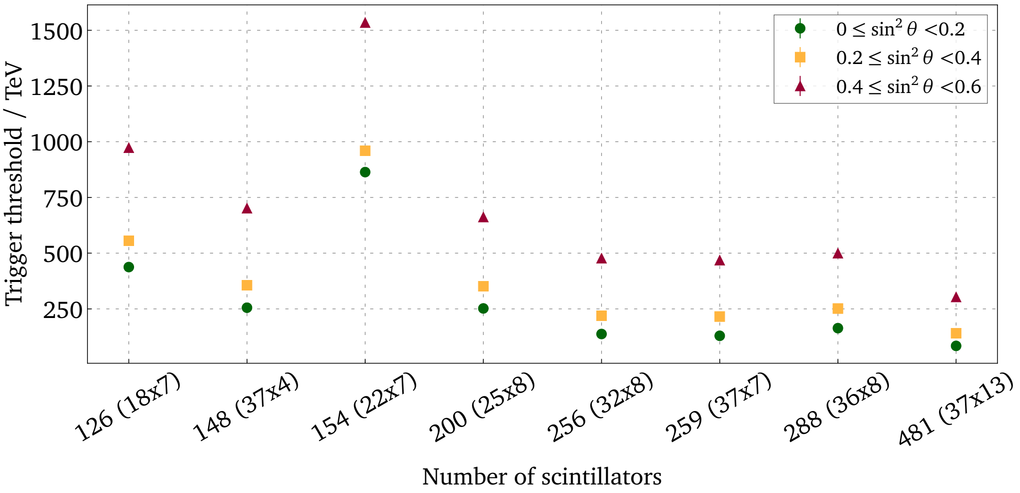

Figure 4.9: Summary of trigger thresholds for different layouts and zenith angle ranges. The uncertainties on the thresholds were obtained by error propagation on Equation 4.1 using minimal residual method.

modules and 3 radio antennas will be deployed. The adjusted layout of the hybrid stations among already existing modules — IceTop tanks as well as prototype scintillator-stations installed since 2018, are presented in Figure 4.10. The distance between two pairs of modules within the station is 72 m and the average distances between the closest centres of the stations is around 145 m.

4.2 Simulation results for the final layout

In this section a broader analysis of the detection-threshold for the chosen layout is presented with respect to different cosmic-ray properties.

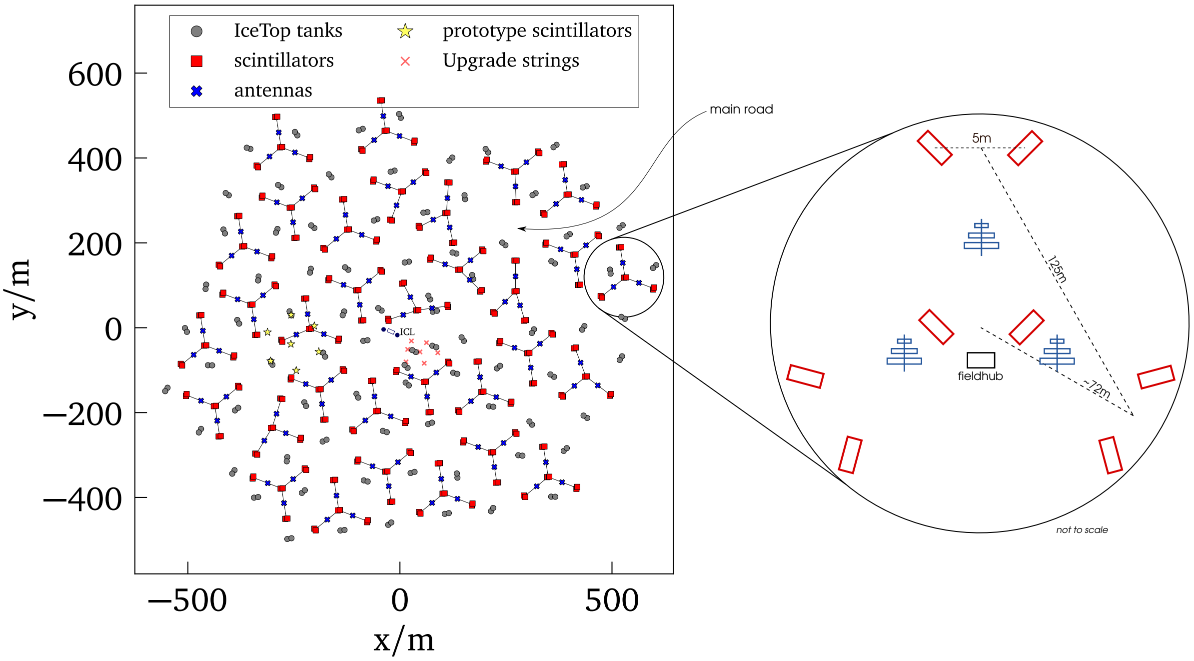

Figure 4.10: The final layout of the planned IceTop enhancement with hybrid stations. The revised layout includes areas reserved for the in-ice upgrade. The black lines which connect scintillation-modules roughly represent the cabling lines for each station. Every hybrid station will consist of 8 scintillation-detectors, 3 radio antennas and 1 field hub hosting the main electronics. Yellow stars indicate the position of 7 scintillation modules installed in 2018. In the same region 2 radio antennas in 2019 and 11 (8 scintillator panels and 3 radio antennas) detectors in 2020 were deployed.

The spatial distribution of secondary particles from atmospheric cascades differ with respect to the cosmic-ray interaction height and, what is directly connected to that, primary cosmic-ray species. In general, heavy-mass cosmic-rays lead to spread of particles over larger area, which can be understood with an idealistic superposition model where Fe-nuclei splits its energy in 56 H-like primaries of energy $E_{Fe}/56$. However, the heavier primaries will start the first interaction earlier in the atmospheric depth than the lighter ones, leading to the smaller number of particles surviving to the ground. Thus, the discussed efficiency curves will depend on the cosmic-ray mass.

The same steps as described in section 4.1 were performed but for 4 cosmic-ray primaries, H, He, O and Fe, and also for γ-rays. The results can be seen in Figure 4.11. The clear dependence on the mass is visible – the lighter the cosmic-ray, the lower the achievable threshold. The difference in the 98% threshold between proton and iron induced air-showers is around 180 TeV for a zenith angle up to 45° and around 80 TeV for the quasi-vertical range. In addition, there is a slight change in the slope of the efficiency curve – a higher mass results in a steeper slope. It is very relevant to properly understand the behaviour of these curves. Since all cosmic-ray analyses rely on the energy-dependent efficiencies, although as it will be shown in chapter 6, mainly on the curves with the folded reconstruction efficiency.

In addition, photon-induced air-showers were analysed. Photons are excellent cosmic messengers, providing substantial information about the Universe. They are not influenced by the magnetic field and therefore can directly reveal astrophysical sources. However, due to

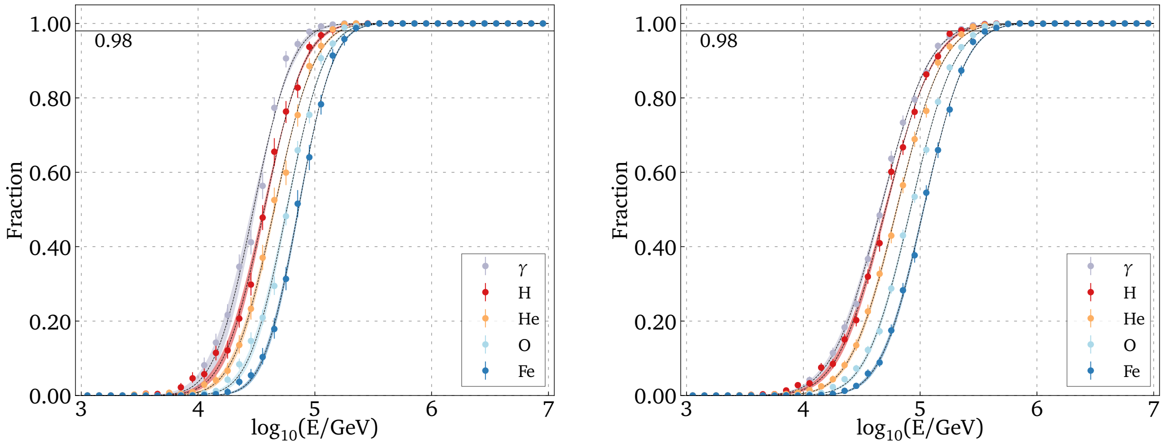

(a) $\theta \lesssim 26°$, $\cos\theta > 0.9$

(b) $\theta \lesssim 45°$, $\cos\theta > 0.7$

Figure 4.11: Efficiency of air-shower detection over the primary cosmic-ray energy for the final layout of scintillation detectors for H, He, O, Fe and γ primaries. The efficiencies are depicted for two ranges of the cosmic-ray zenith angle.

interactions with inter- and extra-galactic radiation, they are absorbed, and it is very challenging to detect and select them from charged primaries above 100 TeV energy [61]. However, with a new approach in radio-detection of air-showers it could be possible [164] if the particle detectors will efficiently trigger the antenna array.

As can be seen in Figure 4.11, the efficiency for photon induced air-showers is higher than in case of cosmic-rays. Photons generate large electromagnetic cascades with significantly smaller contribution of the muonic component. Electrons from pair-production have smaller transverse momentum than in the case of hadronic cascades. This results in a tight distribution of particles around the shower axis for photon induced air-showers [61] and thus the footprint is denser and more contained within a detection area. However, in the case of inclined air-showers, this situation changes due to absorption of the electromagnetic component along a larger slant depth.

Since the scintillation modules shall enhance the current IceTop, we investigated the efficiency for different combinations of selecting the scintillation modules together with Cherenkov tanks. The simulated tanks include a layer of snow based on in-situ measurements performed in March 2019 (see Figure 3.8). The results for the detection efficiency are depicted in Figure 4.12.

The IceTop trigger algorithm distinguishes two types of coincidence: soft local coincidence (SLC) and hard local coincidence (HLC). The HLC requires to have signals in both neighbouring tanks, arriving within 1 μs, while the SLC takes all single signals [97]. The HLC signals provide very clean data sets, while the SLC signals at large lateral distances are correlated to the muon component [105]. However, the HLC condition considerably increases the array energy threshold, which can be clearly seen in Figure 4.12 (selection of 3 tanks flagged as HLC). Including the SLC signals improves it to around 720 TeV for proton-induced air-showers. The combined efficiency of scintillation detectors and tanks allows for the detec-

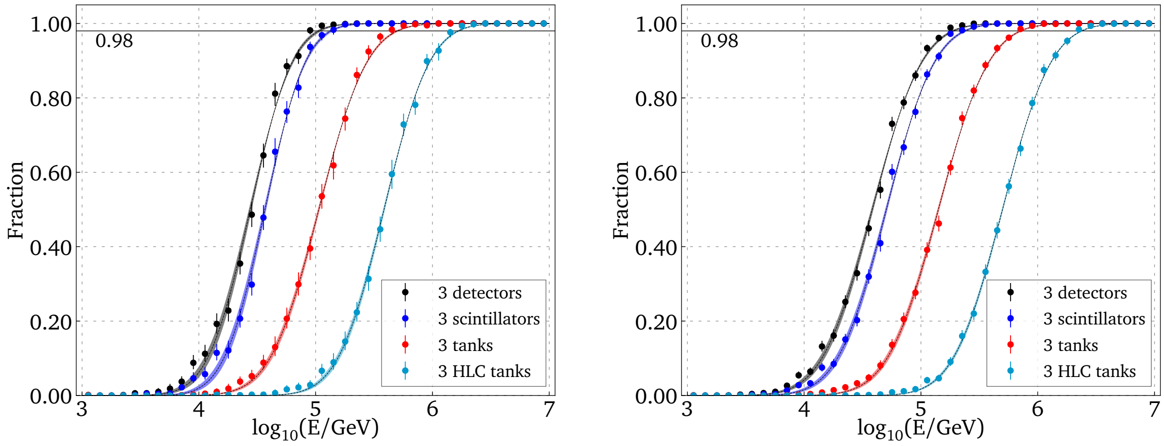

(a) $\theta \lesssim 26°$, $\cos\theta > 0.9$

(b) $\theta \lesssim 45°$, $\cos\theta > 0.7$

Figure 4.12: Efficiency of air-shower detection over the primary cosmic-ray energy for the final layout of scintillation detectors and for the IceTop tanks. The efficiencies are depicted for two ranges of the cosmic-ray zenith angle.

tion of air-showers below 200 TeV. This will not only allow for the further improvements of the low-energy cosmic-ray analysis but improves a potential for enhancing the veto capabilities for the in-ice. The main boost in lowering the threshold is provided by the scintillator array due to larger number of detectors and a snow coverage above the IceTop tanks. The increased efficiency is still possible despite the higher VEM threshold for scintillator modules (0.5 VEM) compared to that of the Cherenkov tanks (0.16 VEM). Moreover, no standard HLC cleaning procedure was applied to the tank signals to provide similar level of comparison since such procedure does not exist yet for the scintillator pulses.

Chapter summary

After studying different configurations of scintillation-detector placements within the IceTop footprint, the final choice has been made. It takes into account the aimed physics goals as well as an optimisation of the deployment procedure at the South Pole. We investigated the influence of the primary mass on the efficiency curve and the enhancement which the scintillation array will bring to the IceTop detection threshold.

Chapter 5

CHARACTERISTICS OF SIGNAL DISTRIBUTIONS

The main condition for detecting an air shower was introduced in Chapter 4, namely a coincident trigger of at least three scintillator panels. To further analyse those pre-selected events, a good understanding of their characteristics is essential, as it will be discussed in this chapter.

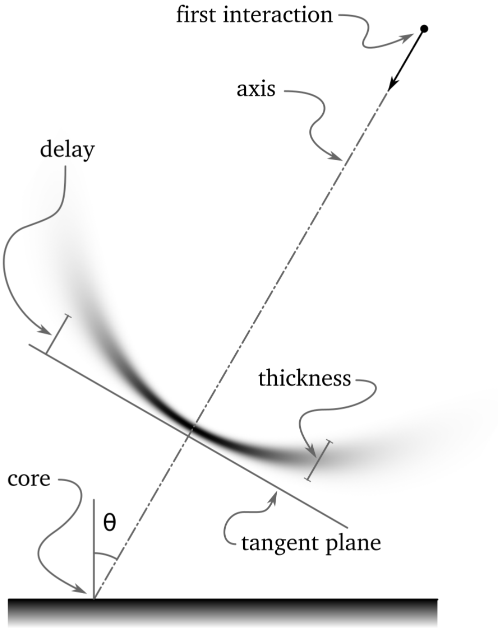

Figure 5.1: Scheme of an extensive air shower and its basic parameters used for the description. Starting from the first interaction and following the incident direction of the cosmic ray, the shower axis is built, which ends at the ground as shower core, the impact point with the highest particle density. Particles create a curved disk reflecting the lateral spread. The drawing was inspired by reference [61] and modified by [124].

The properties of the extensive air showers vary with the energy and type of the primary cosmic ray, as discussed in Chapter 3. These variables influence the air-shower development, and consequently, the distributions seen at the ground. When the atmospheric cascade is initiated, it propagates longitudinally along the track of the primary direction (see Figure 3.4), called the shower axis. But it also develops laterally, mainly due to the transverse momentum transferred from the hadronic interactions to the individual secondaries as well as the Coulomb scattering of the electromagnetic component [61]. The particles spread away from the shower axis and some of them reach distances far from the impact point at the ground, referred to as the shower core, see Figure 5.1. Thus in fact, shower propagates as a curved disk of the particles, with the disk spread increasing as the particles move away from the axis [61]. This spread is called the shower front thickness. The shape of such air-shower front indicates that the particles at the edges of the disk are delayed with respect to the ones close to the axis. With the core being the most dense region, it implies that the large fraction of the cascade arrives within a short time of few ns [61] on the area very close to the axis, and then some parts arrive tens and hundreds of ns later and much further away from the axis. The scheme of the air shower and its basic parameters are presented in Figure 5.1. The incoming direction of the primary particle are expressed by zenith and azimuthal angles in the same way as in a spherical coordinate system.

However, the ground measurements blur this pure information about the primary cosmic-ray and the air-shower development with different properties of the detector array (illustrated in Figure 5.2). The left panel represents the footprint of a single air shower simulated in CORSIKA. The region around the shower core is very dense but following its lateral behaviour, the density diminishes with increasing distance from the axis. The footprint is dominated by photons which do not contribute to the scintillator signals as significantly as electrons. The region with more than 1000 particles other than photons per bin is marked as a contour line. In the right panel, the same shower is shown, but now propagated through the response of the scintillation-detector array. The size of the detector signal footprint is much smaller and roughly corresponds to the white contour from the left plot (color scales indicate different values).

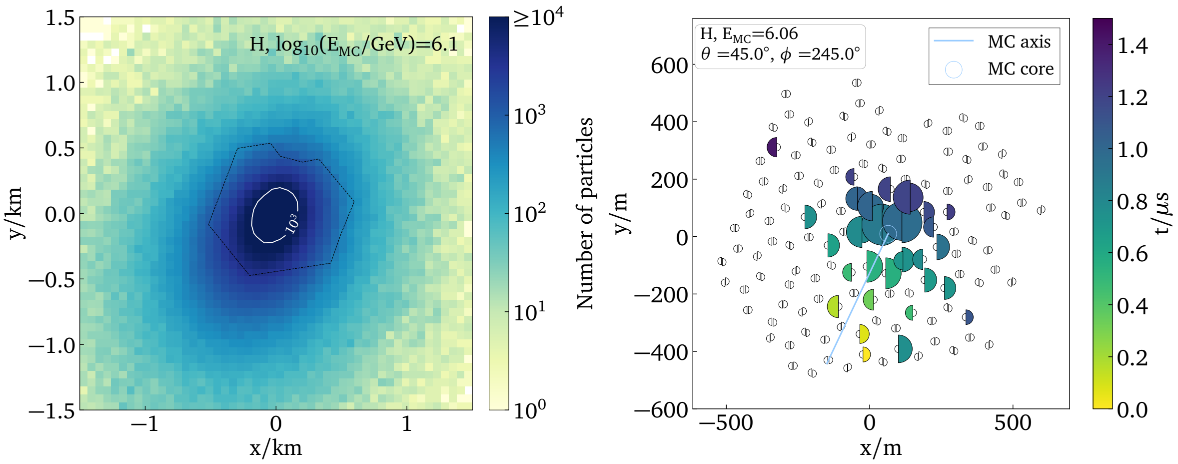

Figure 5.2: An air-shower footprint simulated with CORSIKA (*left* plot) and propagated through response of the scintillator array with Geant4 (*right* plot). The large footprint, dominated by photons, diminishes after sampling it by detector response. The main air-shower observables, like core and direction, can be still reconstructed from the signal distributions. The white contour on the left plot indicates 1000 non-photon particles, and roughly correlates to the footprint registered by the array. The black contour shows the edges of the array.

In Figures 5.3, the simulated lateral particle density (from CORSIKA) and lateral detector signal distribution (after Geant4 simulation) are shown, respectively, for different components of the air-shower initiated by a helium primary of 6.6 PeV and zenith angle of 10°. The density of photons is the highest across all distances. Far from the shower core, the muonic component may dominate the $e^{\pm}$ contribution, since muons can travel large distances without significant energy losses and carry their momentum from high in the atmosphere. The density of hadrons is the smallest close to the shower axis, and exceeds electromagnetic and muonic density at large distances. However, when looking into the distribution folded with the detector response, the situation changes. The photon component is less significant than $e^{\pm}$, as already seen in the footprint plots, the muon contribution is much flatter, and the hadronic contribution is almost negligible. The interesting feature, which is also seen in the IceTop tanks [105], is the increase of the muonic contribution at large distances. Far away from the shower axis, the electromagnetic component becomes less significant in contrary to muons. This effect, seen in the right plot, is however not always present and highly depends on the shower inclination. Nevertheless, it allows at large distances for an analysis of the lateral distribution of muons.

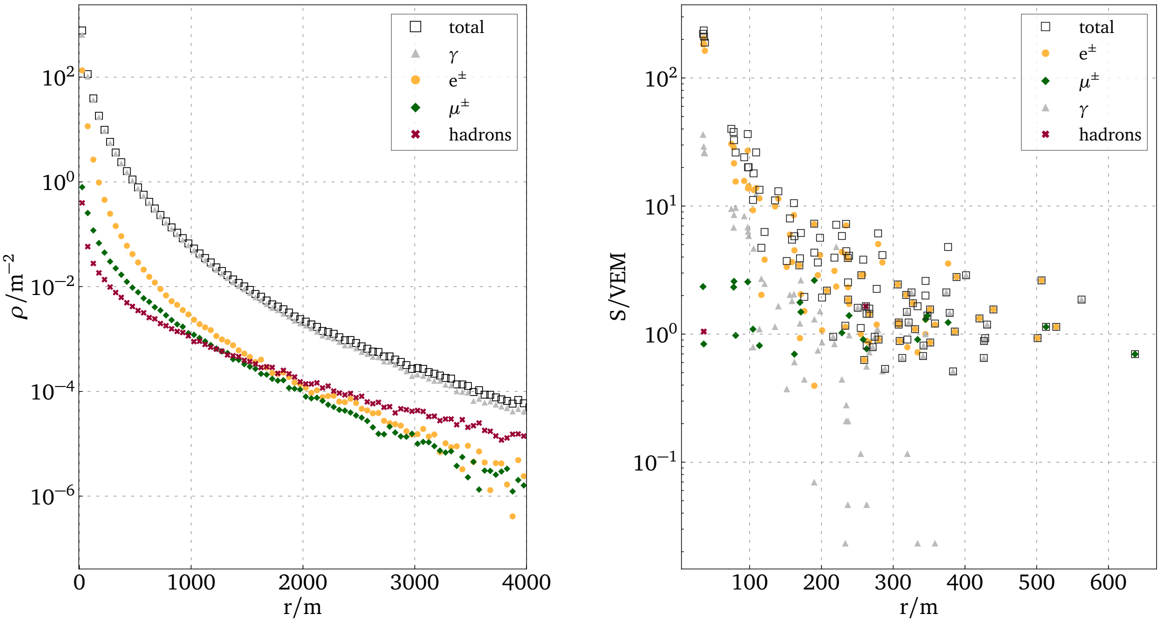

Figure 5.3: Lateral distribution for He-initiated air-shower with energy of 6.6 PeV and cosmic-ray zenith of 10°. *Left*: Density of particle number over a lateral distance of 4 km taken from CORSIKA output, *right*: Distribution of detector signals over lateral distance up to 650 m from Geant4 array simulation. The signals do not include SiPM noise to demonstrate the contributions form the air-shower particles.

Although a clear limitation of the information is left at the detector level, it still can be correlated with the air shower development. Thus, by studying the distributions of the signals and timing at the detector level with respect to the analysis of the pure air-shower development, one can reconstruct the primary information about the incident cosmic-ray. In this chapter, the analysis of the simulated signal distributions for the proposed scintillator array will be discussed.

5.1 Lateral distribution

As mentioned above, the spatial and temporal distributions of the detector signals are related to the energy, mass and incident direction of the primary cosmic ray. All these parameters are essential for a further determination of the spectrum, composition and eventually astrophysical context of cosmic rays. In particular, the lateral particle density seen by the surface detectors provides a main tool to infer the primary characteristics. Its proper parametrisation is one of the most important steps towards the air-shower reconstruction. Therefore, a lot of effort has been done over decades to understand the lateral spread at the ground and to describe its behaviour [61]. The most fundamental and pioneering analytical work on the lateral structure of photon-electron cascades was performed by Nishimura and Kamata [67], and Greisen [69]. It led to the approximated parametrisation of the lateral density of the electrons ρ_{NKG}, referred as NKG function, see Eq. 5.1. Such a function which describes the particle density ρ or the signal distribution S, as a function of a distance perpendicular to the shower axis, is known as lateral distribution function, hereafter LDF:

$$\rho_{\mathrm{NKG}}(r) = \frac{N_e}{2\pi r_m^2}\frac{\Gamma(4.5-s)}{\Gamma(s)\Gamma(4.5-2s-2)}\left(\frac{r}{R_m}\right)^{s-2}\left(1+\frac{r}{r_m}\right)^{s-4.5}, \tag{5.1}$$

where Γ is a gamma function, N_e is the total number of electrons at the observation level in this shower, referred as shower size, s is a slope parameter of the function. r_m is a Molière radius at the particular altitude of the observation, at the South Pole equals to 128 m. For pure electromagnetic cascades, Molière radius refers to a distance at which such shower is contained. Since there is a strong correlation between the total number of particles (and the number of electrons) in the shower and the primary energy, N_e has been often used as cosmic-ray energy estimator. The steepness or slope of the distribution, s, is related to the development of the shower, namely to the slant depth which shower propagates until it reaches the ground. The 'deep' showers, i.e. first interaction is deep in the atmosphere, traverse less distance and so one can see their early development stage close to the ground, thus they are called 'young'. Their lateral distribution is steep. On the other hand 'shallow' air-showers start early and can develop until they leave a footprint at the ground, and are referred as 'old'. Their lateral distribution is flat. Hence, the 'age' of the shower is folded into the slope parameter of the lateral distribution. Due to the difference in electromagnetic and hadronic showers across the overall lateral spread, as well as in detector response which is specific for a given array, some experimentally measured LDFs differ from this theoretical description [168, 169].

Since the different observation altitudes probe in average different stages of the shower development, the behaviour of the lateral distribution might differ between experimental sites. Hence, many groups across air-shower experiments have been developing different modifications to the standard NKG formula, as well as new functional forms, including a fine-tuning of the parameter behaviour. Thus, likewise for the discussed scintillator array, the study of the possible LDFs was conducted. The literature research on different functional forms of LDFs was performed, to benefit from the experience of other experiments, in particular the ones which used scintillation modules, like AKENO [169, 170], Volcano Ranch [43] or KASCADE [168]. The differences in the response of given detector types also influence a choice of LDF. The distributions for arrays, i.e. specific detector types, which are more sensitive to the electromagnetic component might be more easily described with the NKG function, while experiments with muon-sensitive detectors might require a flatter behaviour of LDF. Taking into account the LDFs used at higher altitudes, like IceTop [171], different LDFs were chosen for further studies and are described below.

The modified Nishimura-Kamata-Greisen function

The NKG-like function, equation 5.2, is a modification of the original NKG with different slope parameters and corresponding change in the normalisation coefficient [168].

$$S_{\text{NKG-like}}(r) = \frac{N}{2\pi R_m^2\,\mathrm{B}(s-\alpha+2,\alpha+\beta-2s-2)}\left(\frac{r}{R_m}\right)^{s-\alpha}\left(1+\frac{r}{R_m}\right)^{s-\beta}, \tag{5.2}$$

where α, β, and s are related to the slope of the function and thus in some ways to the age of shower development, as explained earlier. These additional slope parameters provide a better description of the lateral behaviour at various distances. R_m indicates Molière radius or can be also treated as a reference distances. N, the size of the air shower corresponds to the primary energy.
B is a beta function related to the gamma function via following relation: $\mathrm{B}(x,y) = \frac{\Gamma(x)\Gamma(y)}{\Gamma(x+y)}$. This function implies the mathematical constraints on the slope parameters: $\alpha - s < 2$ and $\alpha + \beta - 2s > 2$.

The Linsley function

The other modified form of NKG function is represented by the Linsley function (after [43]), equation 5.3. After it was suggested, many experiments followed and applied this or a similar form to the data [169].

$$S_{\text{Linsley}}(r) = \frac{N}{2\pi R_m^2 \,\mathrm{B}(2-\alpha, \eta-2)} \left(\frac{r}{R_m}\right)^{-\alpha} \left(1 + \frac{r}{R_m}\right)^{\alpha-\eta}, \tag{5.3}$$

where α and η are related to the slope of the function and R_m indicates Molière or reference radius. The change in the normalisation coefficient is also present. The normalisation gives the mathematical constraints on the slope parameters: $\alpha<2$ and $\eta>2$.

Further modified functions

Further modifications led to yet another form which includes the additional term accounting for the higher scaling with the radial distance, equation 5.4. This function is based on hypergeometric Gaussian (HG) formalism taking into account a normalisation constant, as discussed in [172]. While the NKG and NKG-like functions described above are based on Beta functions.

$$\begin{aligned} S_{\text{HG}}(r) &= C(s)^{-1} x^{s-\alpha} (1+x)^{s-\beta} (1+d\,x)^{-\delta} \\ C(s) &= 2\pi \, {}_2\mathrm{F}_1(\delta, s-\alpha+2, \delta+\beta-s, 1-d)\,\mathrm{B}(s+2-\alpha, \delta+\beta-2s-2), \end{aligned} \tag{5.4}$$

where α, β, δ, and s are related to the slope of the function. ${}_2\mathrm{F}_1$ is a Gaussian hypergeometric function. This function also gives mathematical constraints on the slope parameters: $s-\alpha+2 > 0$, $\delta - 2s + \beta - 2 + \alpha > 0$ and $|1-d| < 1$.

Some form of this function was already used by, for instance, the AGASA experiment [173]. Lagutin derived equation 5.5 from theoretical calculations [174]. This group has performed very interesting work by applying the scaling formalism via parameter $R_{m.s.r.}$, targeting the distributions seen by large arrays.

$$S_{\text{Lagutin}}(r) = \frac{N_e C_e}{R_{m.s.r.}^2} \left(\frac{r}{R_{m.s.r.}}\right)^{-\alpha} \left(1 + \frac{r}{R_{m.s.r.}}\right)^{\alpha-\beta} \left(1 + \frac{r}{10\,R_{m.s.r.}}\right)^{-\delta} \tag{5.5}$$

where $R_{m.s.r.}$ refers to mean square radius and is a function of the observation level and the primary energy. Application of this formalism for the case of the scintillator array could be studied in the future.

The double logarithmic paraboloid function

The double logarithmic paraboloid function refers to equation 5.6 in the logarithmic form. It is used in the standard air-shower analysis for the IceTop tanks as it fits to the the flat shape of the tank response distribution [175]. This formula has a different functional form which includes a logarithm in the slope itself and is simpler than others which is reflected in the fit stability. Slope β from DLP functions was reported to have a quasi linear dependence with the NKG age parameter s [175].

$$S_{\mathrm{DLP}}(r) = S_{\mathrm{ref}} \left(\frac{r}{R_{\mathrm{ref}}} \right)^{-\beta - \kappa \log_{10}\left(\frac{r}{R_{\mathrm{ref}}} \right)} \tag{5.6}$$

Although it has been used for the IceTop Cherenkov tanks, it was found to be also suitable for the scintillator array, perhaps due to being at the same experimental altitude, i.e. observation level. Although there are no explicit constraints on the parameters, one can derive the proper physical range on β by requiring that the function has to be monotonically decreasing across the fitted radial range.

Average lateral distributions of signals

All above functions show similar monotonically decreasing behaviour. The main difference lies in how flexible a given function is to describe at the same time, a steep region close to the core and a smoother, but more fluctuating, tail. The average lateral distribution of signals was analysed for different cases, to probe described LDFs and demonstrate general features of these distributions with respect to the cosmic-ray properties.

The average calculations include non-triggered stations to represent the lateral signal density. Three fits to these average distributions were performed using Equations: 5.2, 5.3, 5.6. The optimisations were obtained with the ensemble sampler for MCMC [176].

Two average lateral distributions are shown in Figure 5.4, for proton and iron induced air-showers with primary energy ranging from $10^{5.5}$ GeV to 10^{6} GeV (left plot) and from $10^{6.5}$ GeV to 10^{7} GeV (right plot). The differences between the values expected by a particular function and simulated signals over the error of the mean are shown in the lower panel. The differences between fit types are small. This indicates that all 3 functions can represent the average lateral shape in a similar manner.

Such an average signal distribution shown in Fig. 5.4 manifests an important feature of the lateral distribution. Namely, a region at which distributions from light and heavy primaries cross. It was thought to be of particular interest as it could provide a way towards a mass-independent estimate of the primary energy. This point can be also seen in Figure 5.6, where

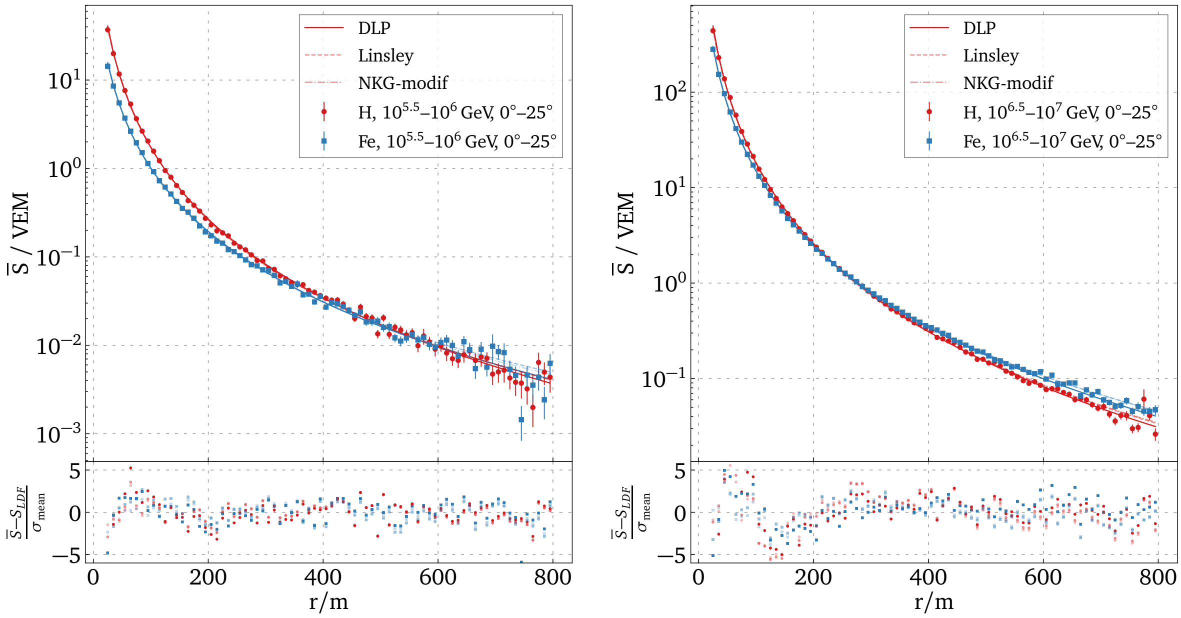

Figure 5.4: Average lateral distribution of signals for proton and iron primaries with energies $10^{5.5}$–10^6 GeV (*left* plot) and $10^{6.5}$–10^7 GeV (*right* plot) with arrival directions smaller than 25° ($\sin^2\theta \leq 0.18$). Lines and residual markers represent respectively different LDFs.

the average distributions produced by different primaries are presented. However, this region strongly depends on the primary energy, which can be seen in these two plots and therefore a different study was performed on the energy estimator as discussed in the next chapter.

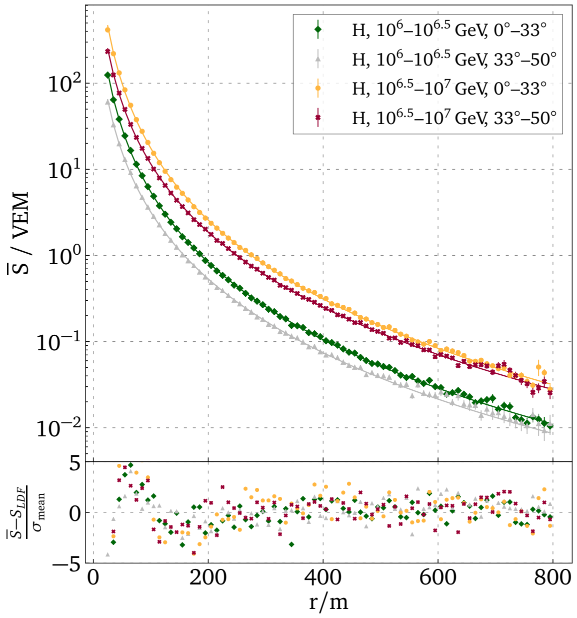

Figure 5.5: Average lateral distribution of signals for proton primaries of 10^6–10^7 GeV energy and two ranges of zenith angles, equal in $\sin^2\theta$. Lines and residual markers represent DLP LDF fits.

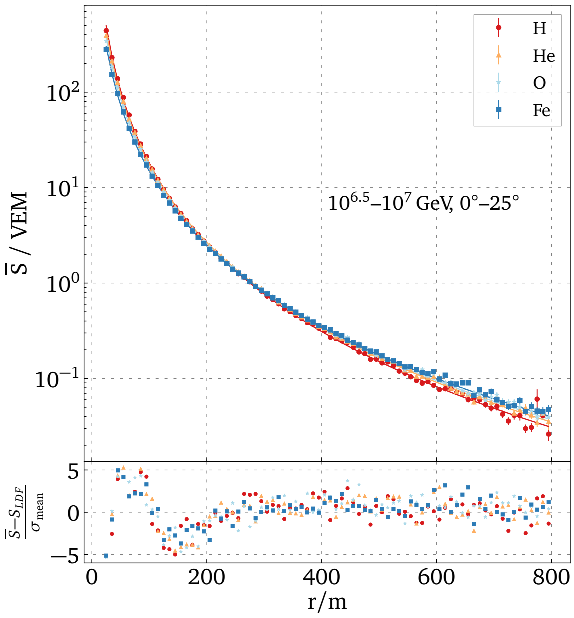

Figure 5.6: Average lateral distribution of signals for H, He, O, Fe primaries of $10^{6.5}$–10^7 GeV energy with arrival directions smaller than 25° ($\sin^2\theta \leq 0.18$). Lines and residual markers represent DLP LDF fits.

In Figure 5.5, the dependence of the lateral distribution on the zenith angle is presented for proton-initiated air-showers for different energy ranges. Two clear features can be observed. For more inclined air-showers, the electromagnetic component is subject to a larger absorption. This is visible as a lower average signal for these showers. The higher zenith angle leads also to a decrease in the slope parameter. However, the zenith influence is less significant than the dependence on the primary energy. A clear dependence of the absolute position of the lateral distribution on the primary energy, seen in Figure 5.5, is the main feature used for energy estimation by many analyses.

Even though the presented average distributions exhibit small deviations with respect to different functions, the event-by-event fits can differ significantly. The fluctuations of single distributions are correlated with large uncertainties due to the stochastic nature of the cascade processes, which are mitigated during the averaging procedure. Moreover, the stability of single fits vary significantly especially for low-energy air-showers. Hence, the LDF optimisation for application on an event-by-event basis was performed and is discussed in the next section.

Scans of the parameter space

The choice of proper parameters for a particular function is a challenging task. Hence, to better understand the lateral behaviour of signals of scintillation detectors, the LDF fits to the individual simulated events were performed. This procedure takes into account the signal fluctuations and the stability of the optimisation procedure for particular LDF. The fit parameters are obtained by minimising the negative logarithm of likelihood function which is constructed in a similar way as in the final reconstruction procedure described in the next chapter. The analysis of the pure simulated distributions with *true* (pure Monte Carlo) values for direction and core allows for neglecting the influence of the reconstruction accuracy in the first step of the parameter evaluation.

The parameter scans were performed for DLP (5.6) and Linsley (5.3) LDFs, on a sample of 2000 proton and iron-induced air-showers. However, to avoid mis-optimisation due to poorly detected air-showers, a series of preliminary quality cuts was applied. Only air-shower with zenith angle up to 45°, true core within 200 m from the array center — so that it can be almost fully contained within the array, with at least 40 triggered detectors — to provide enough points to properly sample lateral distribution. The scans include two free parameters: $\mathrm{S}_{\mathrm{ref}}$, β for DLP and N, α for Linsley, and two fixed parameters: $\mathrm{r}_{\mathrm{ref}}$, κ for DLP and r_{m}, η for Linsley. In both functions an optimal value of reference distance was found and only one slope parameter was scanned (κ and η respectively), by varying it around the allowed space. The HG function has a very complex parameter space and can be a subject of a dedicated study in the future.

The accuracy of the fit is evaluated with the average residuals defined as a function of the lateral distance:

$$\overline{R(r)} = \frac{1}{N}\sum_{i}^{N}\frac{S_i - S_{\mathrm{LDF}}(r)}{\sigma_i}, \tag{5.7}$$

were σ_i is a signal spread which depends on the signal value (discussed in section 5.2). The residuals for DLP and Linsley LDF are presented in Figures 5.7 and 5.9.

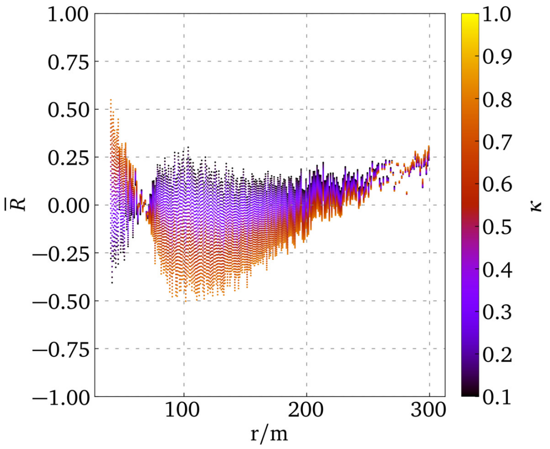

Figure 5.7: Average residuals over lateral distance for different κ values in the DLP LDF represented by colors.

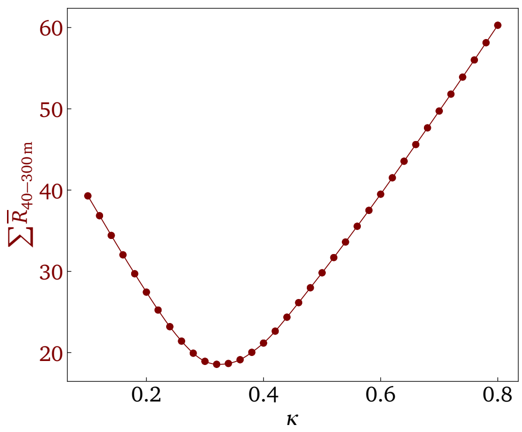

Figure 5.8: Sum of average residuals, $\sum\overline{R}_{40-300\,\mathrm{m}}$, for optimisation of κ parameter in DLP LDF.

To obtain globally optimised values for scanned parameters the sum of $\sum_r|\overline{R}_{40-300\,\mathrm{m}}|$ of all single fits was minimised, as shown in Figure 5.8 and in Figure 5.10. The lateral distribution reflects the density by including the silent station. However, at large lateral distances only the positive fluctuations of the signals [177] can be detected and therefore the fit range at which residuals are calculated is limited to 300 m. To avoid large influence on the residuals close to the shower axis, due to logarithmic behaviour of lateral distributions, the additional cut on radial distance was increased to r≥40 m. In fact, the inner cut on the lateral distance influences the sum of average residuals and hence the optimal values of the parameters, which should be studied in more details in particular when saturation level is experimentally obtained. The choice of log-likelihood optimisation settings was determined by studies of different minimisation algorithms and their limitations. Moreover, the behaviour of function fit was tested in terms of stability. It is important to chose a compromise between the function

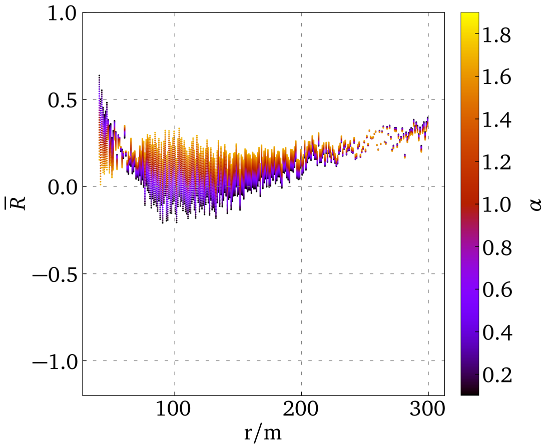

Figure 5.9: Average residuals over lateral distance for different α values in the Linsley LDF represented by colors for a chosen r_m=40 m

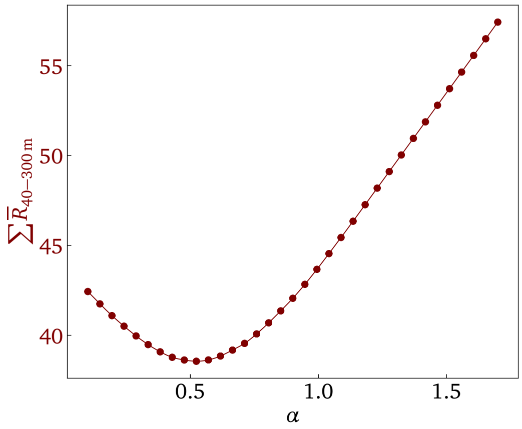

Figure 5.10: Sum of average residuals, $\sum\overline{R}_{40-300\,\mathrm{m}}$, for optimisation of α and r_m parameters in the Linsley LDF.

flexibility and rate of successful fits. Otherwise the accurate fit for some class of events may worsen later the reconstruction efficiency.

The minimisation of the scanned slope parameters is shown in Figures 5.7 and 5.9. The structures on the residual distribution can be correlated with the particular layout and appear for both functions. For instance, the clear drop in the residuals to 0 at around 70 m originates from the fact that in one station detectors are ≈ 70 m apart, hence the probability of sampling this distance is very high. The other structures can be caused by larger distances between stations, where no scintillator module is placed due to presence of IceTop tanks. Increase of the discrepancy between LDF and signals at larger distance is caused by increasing relevance of silent detectors in the minimisation procedure.

Based on these simulation results, $\kappa = 0.35$ for DLP was taken as initial parameter for the further analysis in the reconstruction procedure, taking into account the influence on the reconstruction stability and accuracy.

5.2 Signal spread

Fluctuations of the detected signals originate mainly from the variations of the air-shower development but also from the geometrical response of the array and single-detector fluctuations. There are different methods developed across the experimental groups to account for these effects.

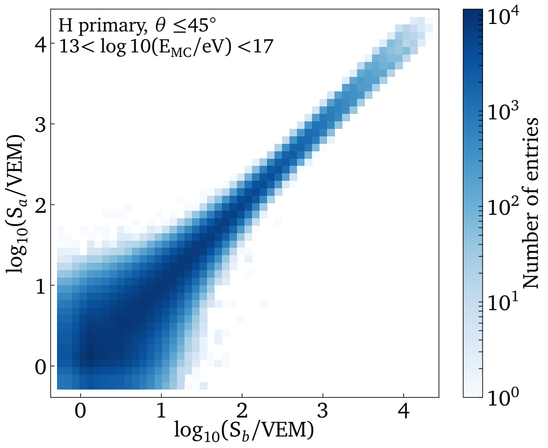

Figure 5.11: Signals from neighbouring detectors from proton initiated air-showers with energy from 10 TeV to 100 PeV with multiplicity of at least 5. Signals are binned along the main trend line. Here shown are all simulated signals, which extend the assumed saturated region. However, for the analysis only S≤ 1000 VEM are included.

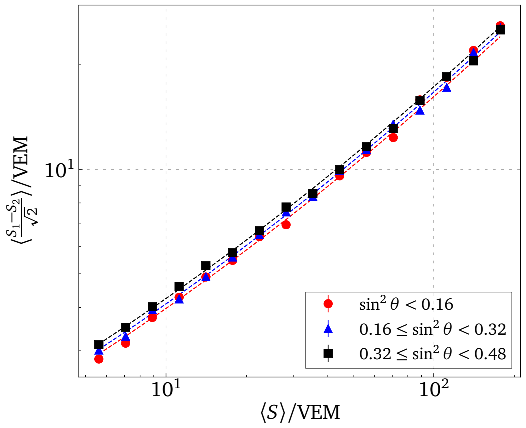

Figure 5.12: De-convoluted signal fluctuations as a function of mean of two signals for different ranges of zenith angles. Signals from H, He, O, Fe primaries in an energy range of 10^{14}–10^{17} eV are included according to GSF [81]. The air-showers from the lowest bin are, however, excluded by a multiplicity cut.

The pairs of signals from the neighbouring panels, S$_a$ and S$_b$, are plotted in Figure 5.11 for proton initiated showers. In the analysis only signals below an assumed saturation of 1000 VEM were taken into account. Only air-showers with more than 20 signals were included, which implicitly increases a considered energy threshold to the region where almost full efficiency is achieved. Moreover, only signals within 40–500 m of lateral distance are considered to minimise the effect of the distance between two detectors.

Due to lack of a large air-shower data with the scintillation detectors, the simulated signals were analysed. Benefiting from the single station layout, the signals from the neighbouring detectors can be compared and constitute as a double measurement at similar lateral distances. The signal expectation value for both detectors will be on average very similar, under the assumption that 5 m distance between two detectors is point-like with respect to the large air-shower footprint. This method was inherited from the analysis performed by the Pierre Auger group on the experimental data [178]. A similar analysis was done also by the IceTop group [179].

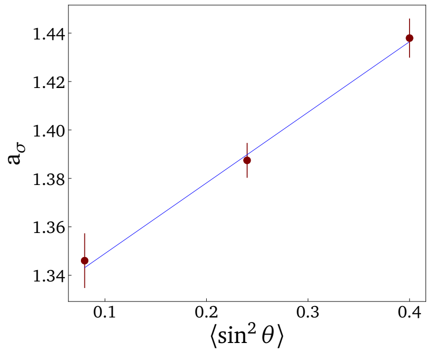

Figure 5.13: Factor for signal fluctuations formula depending on zenith angle for H, He, O and Fe induced air showers, based on Figure 5.12.

The signal uncertainty can be defined as a difference between signals in both panels (similarly like in [178] where instead the relative difference was defined). Such distribution of signals from two detectors gives a convoluted Gaussian sigma and its deconvolution leads to:

$$\delta S = \frac{S_a - S_b}{\sqrt{2}}, \tag{5.8}$$

as a spread of the average simulated signal. The signal pairs are projected and binned along the line of 1:1 correlation between signals in a logarithmic scale shown in Figure 5.11. Every bin is fitted using Gaussian distributions and the resulting mean of δS is taken as a function of center of a given diagonal bin. The mean values are presented in Figure 5.12 for different ranges of zenith angle. Due to the stochastic nature of the cascade development, signal fluctuations are expected to roughly follow the Poisson statistics. However, due to the dependence on the primary zenith angle, the distance from the shower axis as well as general characteristics of the particular array, the results deviate from this assumption. The distribution cannot be well represented by pure Poisson behaviour, hence a more general form of this distribution was assumed: $\sigma(S) = a_\sigma \, S^{c \log_{10} S + d}$, where S is a detector signal and σ describes the typical fluctuation in a single detector. The difference might have also an origin in different detector types or in higher observation level.

A slight dependence on the zenith direction yield the following form for the signal fluctuations:

$$\sigma(S) = (a \sin^2 \theta + b) \, S^{c \log_{10} S + d} \tag{5.9}$$

This result is presented in Figure 5.13. However, the discussed results will have to be revised with the experimental data after the deployment of the first few stations. Then the effects which are not explicitly included in this analysis will be present in the data.

5.3 Time front

The arrival times of the particles hitting each detector in a single event allow for reconstruction of the incident direction of the cosmic ray. The first estimation of the primary direction is obtained analytically from the assumption that the shower particles arrive as a plane disc. More refined results can be reconstructed from the optimisation of the shower front curvature which depends on zenith and azimuth angles. As with the lateral distribution, the shower front recorded by an array will differ between experimental sites due to, for instance, different response of detector types.

The shower curvature is defined as a delay of signal arrival with respect to the plane front assumption as shown in Figure 5.1. This behaviour can be in general described by some form of the parabola-based or in general power-based function. In the scope of this work few functions were studied on average distributions and single events. The functions which most accurately represent the shower front of this particular array are presented in Equation 5.10 and 5.11.

$$\Delta t(r) = n\left[\exp\left(-\frac{r^2}{s^2}\right)+1\right] - ar^2, \tag{5.10}$$

$$\Delta t(r) = ar^2 + b, \tag{5.11}$$

where Δt is a time delay with respect to the plane front and r is a lateral distance. Equation 5.10 is employed in the IceTop reconstruction. The IceTop function includes an additional structure close to the shower axis modelled by a Gaussian part, while the tail is represented by an exponential drop. The parameter scans of those functions were performed in a similar manner as for LDFs to find the parameter values optimal for the scintillator array response.

The Equation 5.11 was found to be more suitable. After visual analysis of many shower fronts, a clear desirability of a parabolic function was found. At lower energies, the parabolic function can well go across the points since they start to delay more quickly from the shower front. On the contrary, at the high energies, when the distribution is more flat at a quite significant range of lateral distances, the parabolic function does not describe the flatness well enough.

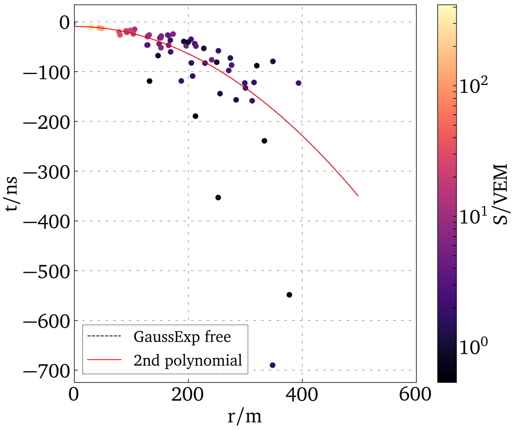

Figure 5.14: Example of shower front initiated by a proton of PeV energy. Colours indicate values of the detector signals. The red line shows the fit with Equation 5.11.

An example of an air-shower front simulated for the scintillator array can be seen in Figure 5.14. In a convention of IceTop reconstruction, time delays are defined negative to the shower plane. The distribution of particles arriving at the ground is spread over the lateral distances. Some of them arrive much delayed with respect to the front, creating a thickness which increases with increasing distance from the shower axis, as shown in Figure 5.1. As seen in Figure 5.14, at larger distances, relatively small signals (represented in the figure by the colors) are subject to larger time delays. These are signals from low momentum particles distant from the shower axis due to development of the cascade and multiple scattering [61].

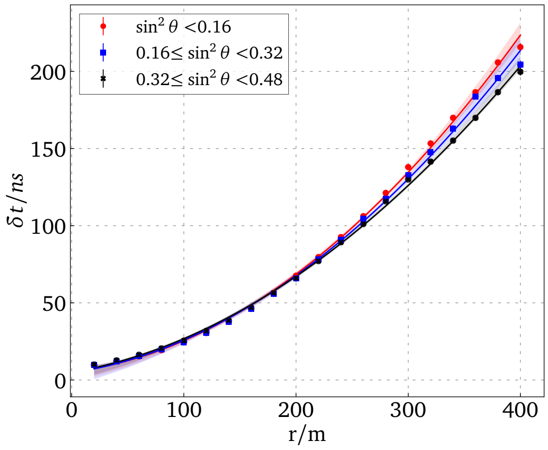

Figure 5.15: Average arrival time delays for H induced air showers in an energy range from 1 PeV to 10 PeV for different angular ranges. The mean of the distribution is obtained from an exponentially modified Gaussian function.

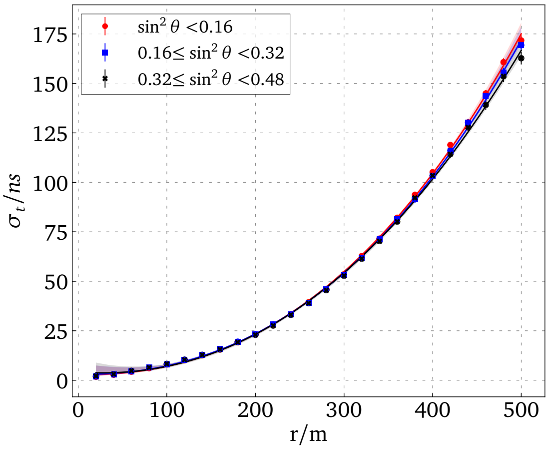

Figure 5.16: Spread of arrival time delays which originate from the shower thickness. The spread is defined as σ of the distribution obtained from exponentially modified Gaussian function. Times from H, He, O, Fe primaries in an energy range of 10^{14}–10^{17} eV are included. The lowest energies are excluded by the multiplicity cut.

This radial dependence of the time delays was analysed. The time delays from air-showers induced by H, He, O, and Fe primaries with energies from 100 TeV to 100 PeV were binned as a function of radial distance. Such distribution of time delays can be well represented by exponentially modified Gaussian function:

$$f(\Delta t) = \frac{\alpha}{2} \exp\left[\frac{\alpha}{2}\left(2\mu + \alpha\sigma^2 - 2\Delta t\right)\right] \mathrm{erf}\left[\frac{\mu + \alpha\sigma^2 - \Delta t}{\sigma\sqrt{2}}\right], \tag{5.12}$$

where $\mu_t = \mu + 1/\alpha$ and $\sigma_t^2 = \sigma^2 + 1/\alpha^2$. The distribution of the μ_t is shown in Figure 5.15 and refers to the average shower front. The distribution of the σ_t is shown in Figure 5.16 and refers to the time spread. Such shower thickness folded with the detector response can be treated as time fluctuations, therefore σ_t represents the uncertainty on the shower front curvature and was parametrised with a 3rd degree polynomial with the leading coefficient depending on $\sin^2\theta$, and is included in the reconstruction optimisation.

Primary mass dependence

Due to their varying properties, the air-shower particles differently contribute to the shower front. It has been already seen [61], that muons arrive earlier than electromagnetic particles. This also can be seen in Figure 5.17. As it was discussed, air-showers induced by different primaries manifest differences in number and distribution of various secondary types.

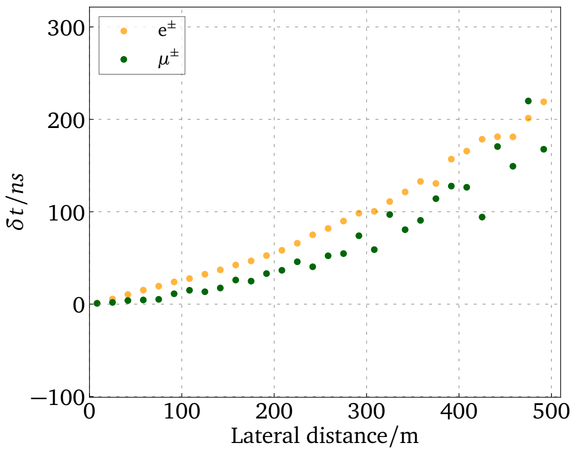

Figure 5.17: Average arrival time delays of muons and electrons for proton initiated air-showers.

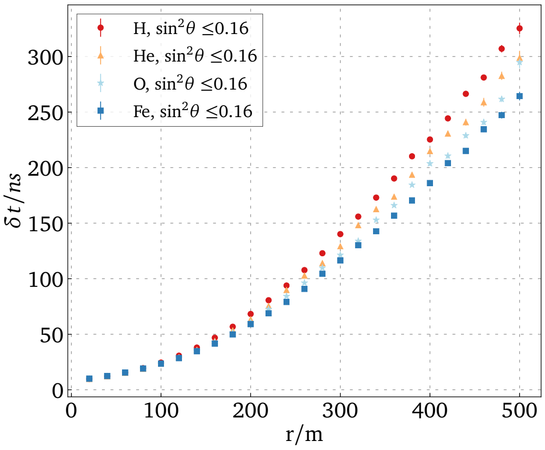

Figure 5.18: Average arrival time delays for H, He, O and Fe primaries for quasi-vertical showers in energy range from 1 PeV to 10 PeV.

Thus, many analysis are aiming on estimating mass of primary cosmic-ray based on such arrival time information, by separating muonic and electromagnetic components. Average shower fronts for H, He, O and Fe induced air-showers are depicted in Figure 5.18. Clear differences in slope of the distributions can be seen, what indicates that a parameter in the shower front fit, which describes parabolic term, can be sensitive to the primary mass.

Chapter summary

The temporal and spatial distributions of the detector signals were studied for the finally proposed scintillator detector array. After evaluating different functions, the DLP LDF and the parabolic shower front description were chosen as functions for the reconstruction of the extensive air showers.

Chapter 6

AIR-SHOWER RECONSTRUCTION

In Chapter 5 it was discussed that the spatial and temporal distribution of the detector signals from air showers reflect the properties of the incident cosmic ray. The functions describing these distributions can be directly correlated to the observables of the primary properties. Therefore, it is essential to derive a reliable procedure for the reconstruction of the extensive air showers parameters and hence infer the cosmic-ray properties.

The reconstruction method for the scintillator array is based on the methods employed by other cosmic-ray experiments [177, 180], but in particular on the procedure developed for IceTop [175]. Within the scope of this thesis, the first version of the reconstruction software [181] for the discussed scintillator array has been developed to create a standard analysis chain. The work was incorporated within one of the first versions of the new project of the IceCube software, called *RockBottom* [182, 183]. The project itself deserves additional attention, since its main goal is to provide a common framework for a multi-detector reconstruction. The first benefits of this approach are clear when combining IceTop and in-ice data to recontruct, for instance, the cosmic ray direction as presented in [183]. Using individual and independently operating surface arrays in a hybrid reconstruction will bring further improvements and will decrease analysis uncertainties. One of the essential tests of the new framework was to perform an analysis for the new detector array, here the scintillator array, of which the results are presented in this chapter.

6.1 Reconstruction algorithm

The reconstruction algorithm is based on a fit of the lateral distribution of signals and trigger times of the detectors by an iterative minimisation of the negative log-likelihood functions, taking into account properties of the response of this particular air-shower array (signal and time spread presented in Chapter 5).

First estimates

The first step of the reconstruction procedure is based on calculating the approximate values for the shower core and direction. The position of the core can be approximated with Equation 6.1:

$$\mathbf{r} = \frac{\sum_i r_i w_i}{\sum_i w_i}, \qquad w_i = S_i, \tag{6.1}$$

where r_i represents coordinates of i^{th} detector and S_i its signal in VEM.

The direction of the primary, $\mathbf{n}$, is estimated in the first step with an assumption that the shower front is a plane. This is a valid approximation taking into account a fairly small curvature of analysed air shower front. The time needed by the shower plane to reach a given detector, in the shower coordinate system, can be calculated, assuming the plane moves with speed of light, c and the shower core arrives at ground at the time t_0. The primary direction and the time of the core arrival can be estimated by minimising Equation 6.2:

$$\chi^2 = \sum_i \frac{\left(t_i - t_0 + n_x x_i/c + n_y y_i/c\right)^2}{\sigma_i^2}, \tag{6.2}$$

where t_i is the time recorded by the i^{th} detector. The simplified analytical solution for the set of 3 linear equations can be obtained by ignoring the z component (relative height difference of the detectors) and utilising Cramer's rules.

These steps provide the first guesses and initial parameter values for a more elaborate reconstruction procedure. They were evaluated in the validation against the real data from the prototype stations. Reconstructions based on simulated and measured signals from scintillator station were compared giving only a few degrees difference in zenith and azimuth angles (see details in Appendix C).

The accuracy of these first estimates based on a full array simulations is on the order of a few tens of meters for the core and around 10° for the angle between the true and estimated directions. In addition to these geometrical parameters, the first guess on an energy estimator can be obtained simply from the number of hit detectors.

Construction of a log-likelihood function

The information from all detectors is further merged in three iterations of minimisation of the negative log-likelihood $-\ln\mathcal{L}$. The minimisation is performed using the MINUIT algorithm implemented within the IceCube software. The log-likelihood, $\ln\mathcal{L}$, for optimisation of the lateral distribution is taken as a sum of log-likelihoods for: triggered detectors, $\ln\mathcal{L}_{tr}$, saturated detectors, $\ln\mathcal{L}_{sa}$, and silent detectors, $\ln\mathcal{L}_{si}$, as represented by a set of equations 6.3 [177, 180].

$$\begin{aligned}
\ln\mathcal{L} &= \ln\mathcal{L}_{tr} + \ln\mathcal{L}_{sa} + \ln\mathcal{L}_{si},\\
\ln\mathcal{L}_{tr} &= \begin{cases} -\sum_i \left[\frac{1}{2}\left(\frac{S_i - S_{\mathrm{LDF}_i}}{\sigma_i}\right)^2 + \ln\left(\sqrt{2\pi}\sigma_i\right)\right] & \text{if } \mathrm{S}_i \geq 2\,\mathrm{VEM},\\ -\sum_i \left[S_{\mathrm{LDF}_i} - S_i \ln\left(S_{\mathrm{LDF}_i}\right) + \ln\Gamma(S_i+1)\right] & \text{if } \mathrm{S}_i < 2\,\mathrm{VEM}, \end{cases}\\
\ln\mathcal{L}_{sa} &= \sum_i \ln\left[\frac{1}{2}\,\mathrm{erfc}\left(\frac{S_{max} - S_{LDF_i}}{\sqrt{2}\sigma_{sa_i}}\right)\right],\\
\ln\mathcal{L}_{si} &= \sum_i \ln(1 - P_{hit}),\\
P_{\mathrm{hit}} &= 1 - a\left(1 + \mathrm{erf}\,\frac{b - \log_{10} S_{\mathrm{LDF}_i}}{c_1}\right)\left(1 + \tanh\frac{b - \log_{10} S_{\mathrm{LDF}_i}}{c_2}\right),\\
S_{\mathrm{LDF}_i} &= S_{\mathrm{LDF}_i}\left(r_i, \kappa, S_{\mathrm{ref}}, \beta, \theta, \phi, \mathbf{r}_{\mathrm{core}}\right),\\
\sigma_i &= \sigma_i\left(S_i, \theta\right)
\end{aligned} \tag{6.3}$$

where S_i is the signal recorded by the i^{th} detector, S_{LDF} is the expected signal based on the chosen LDF model, and σ is the square root of the signal variance as described in Chapter 5. The spread of signals acts as a weighting factor for the minimiser, accounting for the fluctuations of the air-shower development and array response. The signals below around 2 VEM do not follow the Gaussian distribution anymore, therefore a likelihood based on gamma distribution is used in this region (second part in $\mathcal{L}_{tr}$).

The probability for a detector to be triggered, P_{hit}, is derived based on the signals above the trigger threshold as a function of the logarithm of the expected signal. The trigger threshold of a single detector is assumed to be a fixed value of ≥0.5 VEM on the signal level. Below that value also the SiPM trigger of 4 PEs is folded in. The efficiency is calculated based on the reconstructed LDF values. Once the curve is implemented in the reconstruction, the next iteration might change it. Thus, the fit values are further re-implemented in the reconstruction and the analysis is repeated as long as the resulting curve does not change significantly. The final curve is shown in Figure 6.1 and is fit with the modified error function [184].

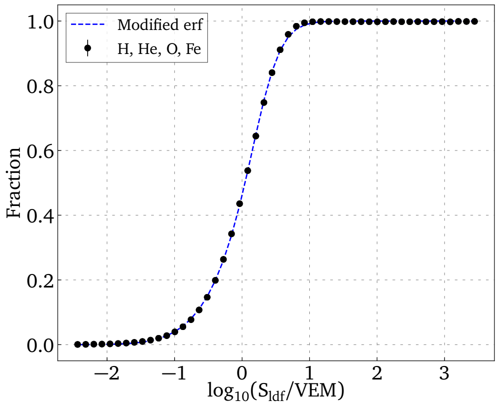

Figure 6.1: The probability of a given detector to be triggered above the 0.5 VEM threshold as a function of lateral signal expected by the LDF model. The distribution was obtained for H, He, O and Fe induced air showers.

The timing log-likelihood is defined by Equation 6.4:

$$\ln \mathcal{L}_t = -\sum_i \sqrt{S_i}\left[\frac{1}{2}\left(\frac{\Delta t_i - \mathrm{front}_i}{\sigma_{t\,i}}\right)^2 + \ln\left(\sqrt{2\pi}\sigma_{t\,i}\right)\right], \tag{6.4}$$

where Δt_i is the time recorded by a detector and front_i is the time expected by a curved shower front model as described in Chapter 5. σ_t is the time spread originating from the shower thickness. In general, the timing likelihood could be formulated with an exponentially modified Gaussian function, which properly describes the binned time distributions, but due to its non-trivial parameter space it is challenging to obtain a stable algorithm. This can be studied in more details in the future and was not covered within this thesis. Moreover, a weighting of the timing likelihood with $\sqrt{S_i}$ was applied, allowing for a slight improvement of the direction accuracy at the highest energies. However, there is still a room for further improvements and verifications against the experimental data.

Iterative minimisation

The optimisation of the signal and time distribution functions must simultaneously resolve 8 parameters: x and y position of the core, zenith and azimuth of the direction, the LDF parameters shower size and slope, and the parameters of the shower front core time and coefficient of the parabolic shape. This implies a requirement on the iterative reconstruction to select events with at least 5 triggered detectors to assure a good stability of the procedure. [175]

During the 3 iterations, different settings are defined for each step, by setting free and fixed parameters, boundaries and step sizes for free parameters. This procedure leaves a broad space for fine-tuning of these settings, in particular to provide the best stability of the minimisation.

It was shown in Chapter 5 that the Linsley function exhibits, in general, smaller deviations for all scanned slope values. However, it is also more likely to enter a difficult optimisation region due to the beta function in the normalisation. Therefore, the reconstruction was performed with the DLP function to study preliminary capabilities of the air-shower reconstruction. For the shower front, a parabolic function with a quadratic coefficient, a_t being free in the reconstruction was used. In the first step, only the LDF fit is performed, where together with S_{ref} and β, the air-shower core position is varied. In the second step, both, LDF and shower front fits are performed, by fixing the core position derived from the previous iteration. In the final step, only the LDF fit is repeated. The settings for this 3-iteration minimisation are summarised in Table 6.1. These settings are found to produce stable reconstructions and provide good reconstruction accuracy throughout three orders of magnitude in energy and a zenith range up to 45 ° for different types of cosmic-ray primaries.

Step	Free parameters	Fixed parameters
1	S_{ref}, β, x, y	θ, ϕ, t_0, a_t
2	S_{ref}, β, θ, ϕ, t_0, a_t	x, y
3	S_{ref}, β, x, y	θ, ϕ, t_0, a_t

Table 6.1: Minimisation settings for three iterations of the reconstruction. The first and last step use only LDF likelihood, while the second step optimises also the time likelihood.

Quality cuts

Based on the analysis of the reconstructed events the selection criteria for a real data sample can be established. Such cuts provide a set of high-quality events and minimise the bias introduced in the final results. There are two sets of cuts applied in the reconstruction. The first one affects the scintillator signals included in the minimisation. A region very close to the core is problematic due to the functional form of the chosen LDF being undefined at $r = 0$ m. On the other hand, since the measurements at a distance far away from the core are very imprecise due to large fluctuations, the LDF is fitted between 10 m and 800 m distance. Regarding the detector trigger times, the scintillator trigger window of 3.5 μs is applied where at least 3 hits are required to record the event. For the shower front reconstruction, hits which are delayed more than 2 μs from the shower plane and are further than 800 m from the shower axis are removed, to eliminate very late hits which do not follow the assumed shower front curvature or, for real measurements, are likely to be due to single muon hits. Some of these restrictions will, of course, influence the efficiency. However, for a given analysis, the individual events can still be included based on the first estimates of the geometry or for the combined minimisation with the IceTop tanks.

The second set requires that the minimisation converged, the reconstructed core is within

400 m from the centre of the array, and reconstructed zenith angle is less than 45 °. For the DLP LDF, the energy sensitive parameter needs to be positive and the slope parameter is required to provide a monotonically decreasing behaviour within the fitted radial range, which can be calculated from the LDF derivative. For instance, at the distance of 10 m, β has to be greater than or equal to 1. In addition, as mentioned earlier, a requirement of 5 hits is applied to provide enough individual point measurements for all reconstructed parameters. Additional quality cuts need to be introduced for the events which are not contained within the array. The cut on the reconstructed core to be inside a radius of 400 m from the centre of the array could be reliable only if there are no mis-reconstructions. In fact, there will be always air showers having their true core outside and systematically reconstructed towards the inside of the array. The influence of these events on the reconstruction and possible cuts, which can be applied to clean the sample are discussed in section 6.3.

6.2 Energy estimator

The cosmic-ray energy spectrum measured at Earth serves as a signature of acceleration phenomena happening at different scales of the Universe. Since it is already convoluted with effects of the cosmic-ray propagation, which are not fully understood, it is very important to understand the actual flux arriving at Earth as precisely as possible. Hence, good methods of air-shower reconstruction with low uncertainties of the parameters characterising the primary energy are crucial.

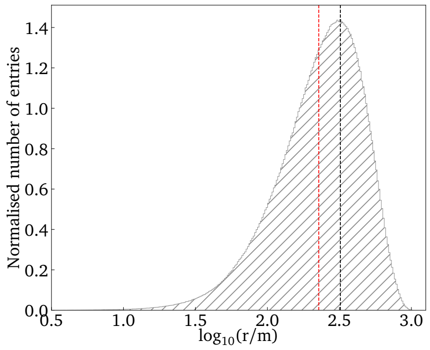

Figure 6.2: Distribution of the lateral distances from triggered detectors. The mean value (red line) corresponds to the distance of 220 m and the most probable value (black line) above 300 m.

After decades of research, still two main aspects are considered while choosing suitable parameters to determine the primary energy and construct the all-particle spectrum. Namely, the independence on the primary mass and the minimisation of the statistical fluctuations. The minimum bias on the primary mass is also crucial for better estimation of the single mass-group spectra. The results can be sensitive to a preferential response of the array which systematically reconstruct light-mass groups better than heavy ones due to their higher number of secondary particles at the observation level.

According to the NKG formalism, the shower size, which refers to the number of particles in the cascade, can be directly connected to the primary cosmic-ray energy. However, in the case of Cherenkov tank or scintillator panel arrays, it is not possible to measure the real particle densities. Hillas [185] has shown that, for an array of Cherenkov detectors, the signals taken at medium distances from the shower axis do not strongly depend on the lateral shape and can therefore serve as a reliable primary energy estimator. The choice of the proper distance is, however, not a trivial task. The methods chosen for different arrays alter depending on the detector type and response, observation level and array spacing, showing that there is so far no method which can be straightforwardly applied to all air shower experiments.

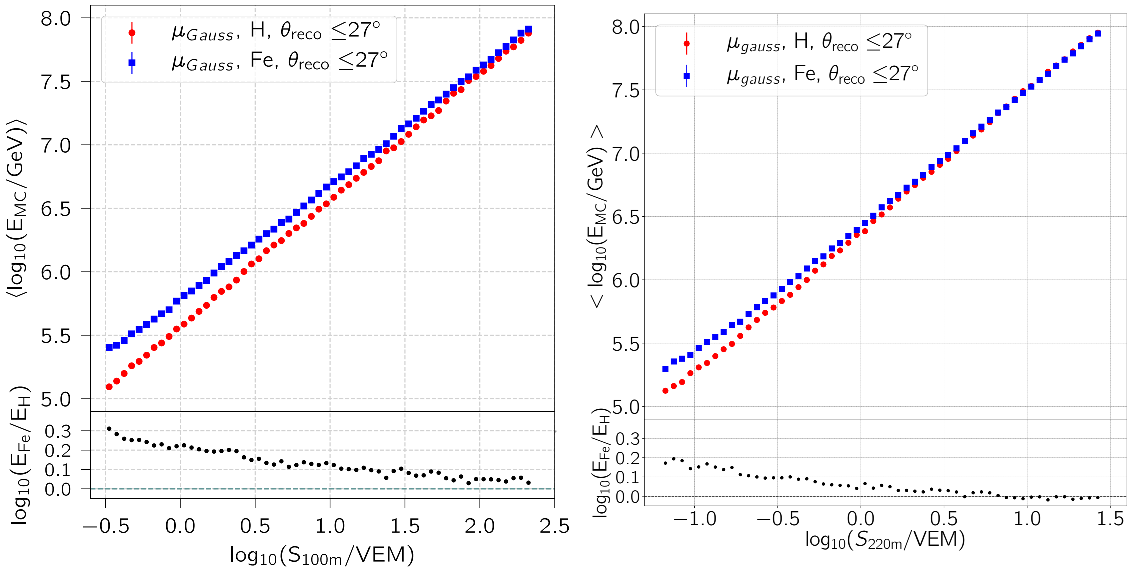

Figure 6.3: MC energy binned as a function of reconstructed S_{ref} for 100 m (*left* plot) and 220 m (*right* plot) for H and Fe induced air showers. At larger distances from the shower core, a difference between two cosmic ray types diminishes. Figures taken from [155].

Reference distance

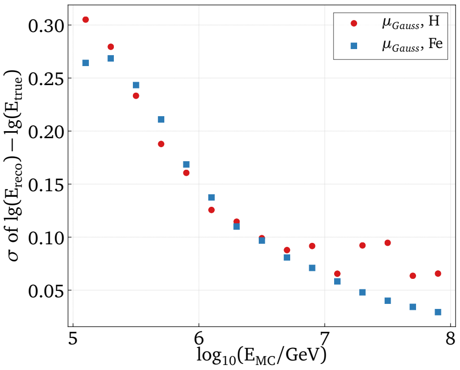

Figure 6.4: Resolution of energy estimator for quasi-vertical H and Fe induced air showers.

For the chosen DLP LDF, the choice of reference distance does not directly influence on the quality of the lateral fit, since the signal at the reference distance only acts as a normalisation factor. Hence, two approaches were used to obtain some reliable values. The method used in the IceTop analysis itself, points out that the slope of the LDF is correlated quite strongly with the primary mass [186]. Therefore, to achieve a minimum correlation between the energy estimator and the primary mass, a minimisation of the covariance between β and S_{ref} was performed. With some approximations, it was concluded that the mean of the lateral distances corresponds to such a minimum correlation [186]. This distribution for the scintillator detectors is shown in Figure 6.2 and suggests a distance of around 220 m. However, since air showers are subject of stochastic processes, their development fluctuates significantly, which is also reflected at the ground in the lateral distribution. These fluctuations are not equal across all lateral distances, and hence care must be taken to chose an optimal distance which does not considerably increase the uncertainty of the energy estimation.

To verify the above assumption, a second approach was utilised to analyse the influence of the r_{ref} parameter on the behaviour of the energy estimator directly in the reconstruction. The results of the reconstruction for two reference distances are presented in Figure 6.3. In

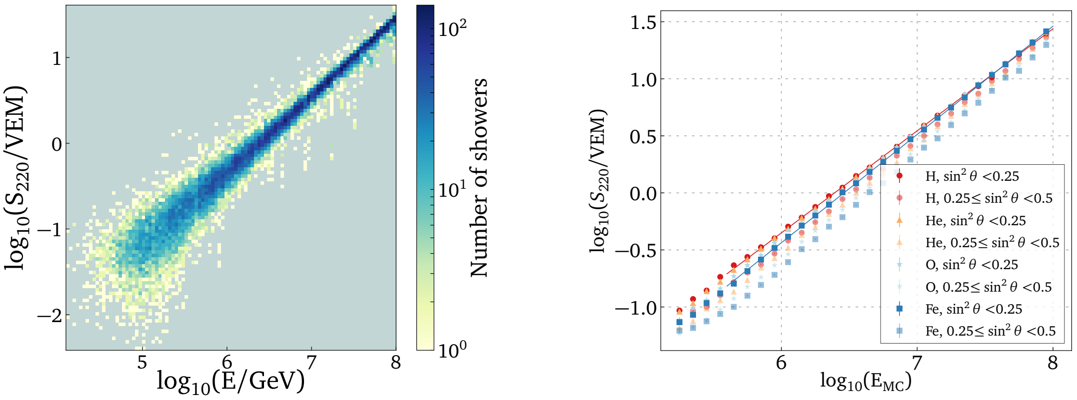

Figure 6.5: Distribution of S_{220} for H induced air showers (*left* plot). Average S_{220} for quasi vertical air showers, up to 30°, and more inclined ones from 30°–45° for H, He, O and Fe air showers (*right* plot). The bias between different primary types increases with the zenith angle.

the lower panels the differences of $\log_{10} E_{Fe} - \log_{10} E_H$ are depicted. The reference distance closer to the core provides a smoother behaviour of the energy calibration curve, however it shows a clear bias between two primary types. On the contrary, going to larger reference distance decreases this effect, which results in smaller differences between H and Fe curves. Since this is also the distance when a triggered detector appeared the most often, it seems to be a stable point to infer the primary energy. Thus, a distance of 220 m was chosen for the further reconstruction.

In Figure 6.5 (left) a distribution of the reconstructed S_{220} is shown with respect to the MC energy for H induced air showers. A clear dependence on the primary energy is visible with a spread decreasing with increasing energy. In Figure 6.5 (right) mean S_{220} distributions are presented for H, He, O and Fe primaries. The fairly linear dependence on the averaged values holds over almost 3 energy decades — the full studied operation range. Moreover, only a small bias on the primary mass can be noticed for quasi vertical showers, providing a reliable energy estimation disentangled from the primary type. More inclined showers quickly introduce larger uncertainties on the primary energy estimation. Due to absorption in the air, the differences in the size of electromagnetic component are enhanced.

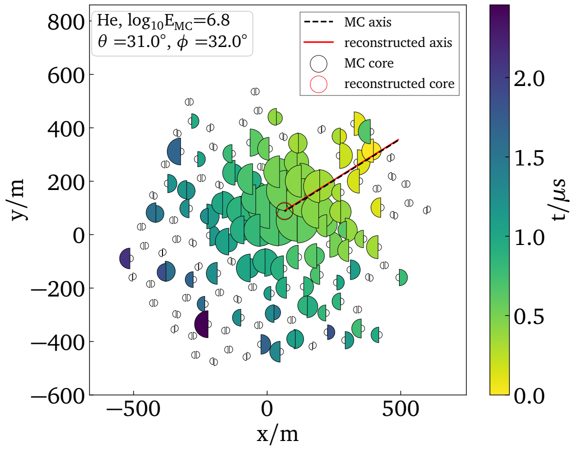

Figure 6.6: A footprint of a He initiated air shower of simulated energy of 6 PeV. The halves of the circles indicate signals in two neighbouring detectors with size being related to the signal value. The colors correspond to the trigger times. The simulated (black) and reconstructed (red) shower core and projected axis are also shown.

The distribution of the reconstructed energy estimator corresponds to a certain width, which can be used to assess how accurate is a given energy estimator. Standard deviations of the differences between $\log_{10} E_{reco} - \log_{10} E_{MC}$ are presented in Figure 6.4 as a function of MC energy. At the full effiency region around 1 PeV the value reaches a level of 0.12 and reduces at higher energies to 0.06. This is somewhat higher than IceTop values [187], around 0.05, probably due to larger fluctuations further away from the shower axis. Therefore, in future data analysis, one can further optimise the energy estimator to improve the resolution and minimise the mass dependence.

6.3 Reconstruction performance

The results of a single reconstruction for a He induced air shower are shown in Figure 6.6 with the simulated Monte Carlo and the reconstructed core positions and shower axes; the corresponding distributions are presented in Figures 6.7. A large number of detectors allow for a better estimation of the core, already at the level of first estimates. The corresponding reconstructed distributions are also depicted. The differences between simulated MC and reconstructed values in the lateral and time distributions are really small, taking into account the size of the array and detector spacing. The analysis of the shower front is satisfactory, however some improvement of the functional form is possible.

For the analysis of the reconstruction performance, a set of air-showers from H, He, O and Fe simulations in the energy range from 100 TeV to 100 PeV were reconstructed. The simulated showers were resampled using core locations that were randomly chosen but within 500 m of the center of the array to increase the statistics for studying the array response. For showers that land outside the array, a determination of the primary observables is more difficult. This effect was studied on a sample of proton showers and is discussed briefly in section 6.3.

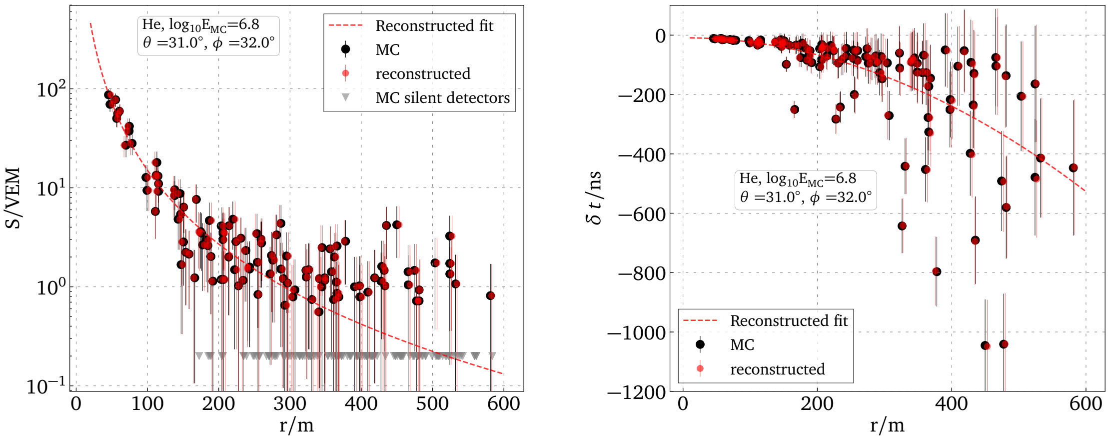

Figure 6.7: The lateral distribution of signals and time delays with respect to the shower front for a He induced air shower (the one from Figure 6.6). Black points represent distributions using simulated MC parameters, while red points reconstructed values. The lines show the fit from the optimisation procedure. In the right panel no silent detectors are shown since they are not included in shower front minimisation.

Resolution

The performance of the reconstruction is quantified by the resolution of the estimated direction, core, S_{ref}, and reconstruction efficiency. The resolution is defined as 68th percentile of the given distribution binned in the MC primary energy or in energy estimator, S_{ref}. Accuracy of the reconstruction strongly depends on the multiplicity, as more points reflect better optimisation of the fit. The relation between average multiplicity and true energy for different primaries is shown in Figure 6.8. In Figure 6.9 and 6.10 the angular and core resolution are depicted for proton and iron initiated air showers for two angular ranges. The lower panels of the plots show also a dependence of the average multiplicity of triggered scintillation detectors. The resolution of the core significantly improves when a lateral fit is included after the center of gravity estimation. At the lower energies, the resolution corresponds to the spacing between closest detectors, while at the highest energies it improves so that the size of the detector constitute an uncertainty. It is worth to notice, that although a shower core is never used directly as an observable, its resolution influences on the shower front reconstruction and energy estimator.

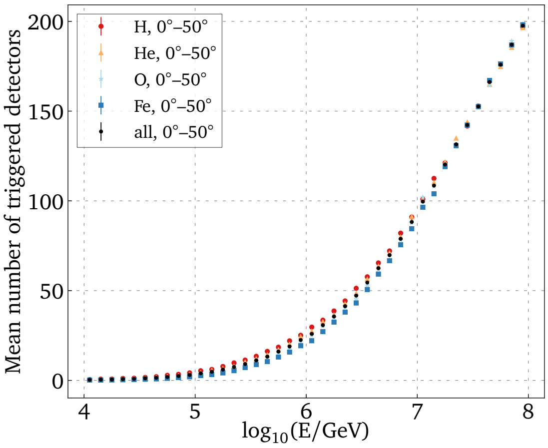

Figure 6.8: Average number of triggered detectors (above 0.5 VEM) as a function of MC energy for all H, He, O and Fe induced air showers, with zenith up to 50°.

The cosmic-ray direction can be reconstructed with a precision of a few degrees below the PeV range. At higher energies, this improves to better than 1°, and even less than 0.2 at 100 PeV. The resolutions worsen in both cases for more inclined showers. Air showers of larger zenith angles manifest different characteristics due to their absorption in the atmosphere and geometrical effects, making the apparent distribution of the detectors seen by the shower not equal with respect to the shower plane. For instance, the flatter shower front of inclined showers is less accurately described by the assumed curvature and core estimation and can be mis-reconstructed due to the asymmetry of the lateral distribution which is more pronounced at the higher inclination. Moreover, for the shower front fit, at larger distances, relatively small signals are subject to larger time fluctuations, which can lead to a mis-reconstruction of the front shape. In addition, shower cores at lower energies can be fixed to the center of gravity which is a more reliable method for low multiplicity events. However, the presented results are sufficient for a future analysis of the anisotropy of cosmic ray arrival directions. In general, also more refined cuts could be applied to achieve a better resolution.

The resolutions for all primaries for quasi vertical showers are depicted in Figure 6.11 and Figure 6.12. A common feature can be noticed: the higher the cosmic-ray's mass, the worse the estimates are on the core and direction. It is directly correlated to the characteristics

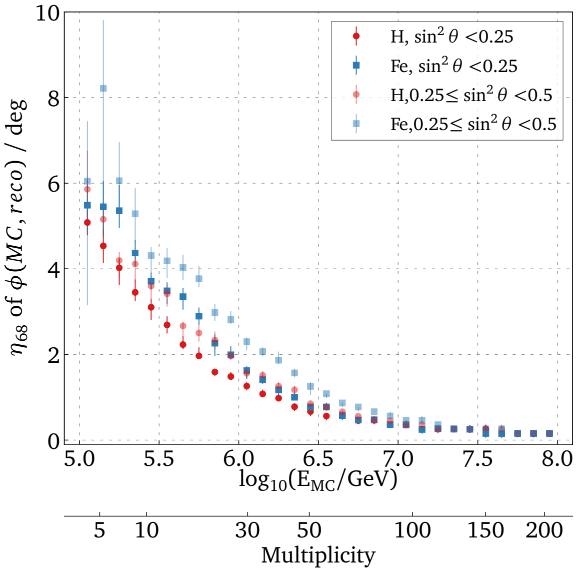

Figure 6.9: Angle of incidence reconstruction for the scintillator array for H and Fe induced showers for different zenith angular ranges up to 45°. The errors were estimated using the bootstrap method and show 95% confidence intervals.

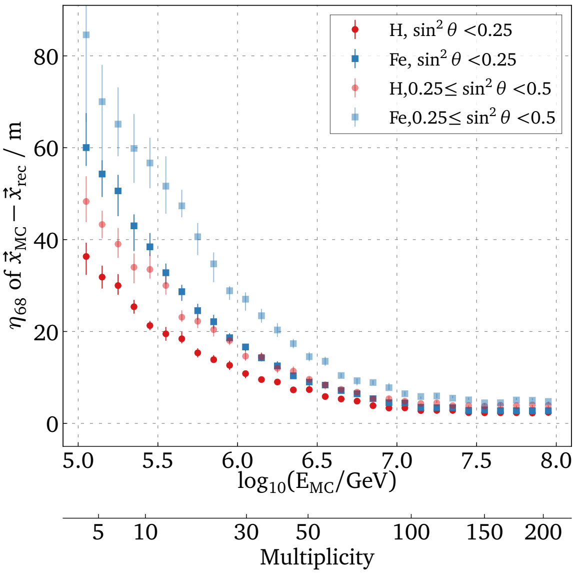

Figure 6.10: The shower core reconstruction for the scintillator array for H and Fe induced showers for different zenith ranges up to 45°. The errors were estimated using the bootstrap method and show 95% confidence intervals.

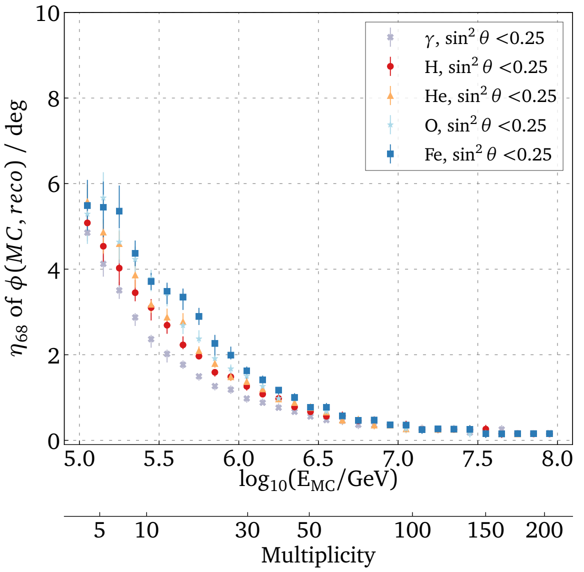

Figure 6.11: Angle of incidence reconstruction for the scintillator array for H, He, O, Fe and γ induced showers for different zenith angular ranges up to 30°. The errors were estimated using the bootstrap method and show 95% confidence intervals.

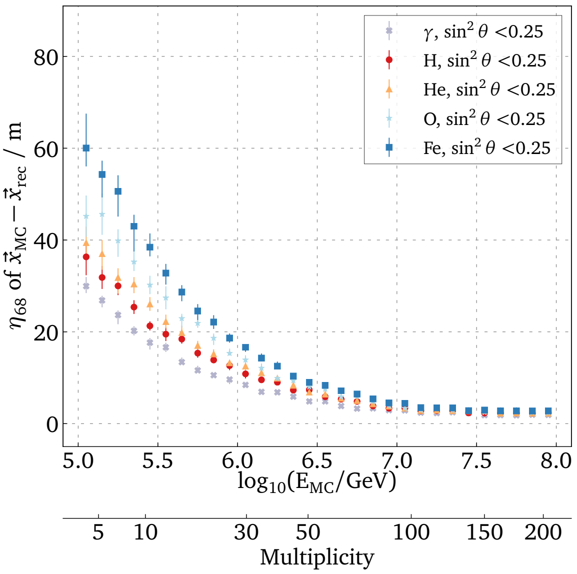

Figure 6.12: The shower core reconstruction for the scintillator array for H, He, O and Fe induced showers for different zenith ranges up to 30° ($\sin^2\theta$<0.25). The errors were estimated using the bootstrap method and show 95% confidence intervals.

of the showers initiated by different primaries. Heavier cosmic rays interact earlier in the atmosphere resulting in smaller number of signals which are more unevenly distributed. Together with cosmic rays, the resolution from gamma induced air showers is presented. Photon showers generate large electromagnetic cascades and have less contribution from muonic and hadronic components. Thus, their distributions is more uniform [61] leading to better reconstruction of the primary properties.

Comparison with IceTop reconstruction

The performance of the scintillator reconstruction can be compared to the IceTop results shown in Figure 6.13. It can be noticed that for the region shown in the IceTop analysis, the core resolution obtained by the scintillator array is highly improved due to the increase of the measurement points. It can reach the level of less than 2.5 m. The angular resolution is better for IceTop in the PeV region. Methods to improve the scintillator array's angular resolution will be studied in the future. At the higher energies the values obtained by the scintillator array become comparable to those of IceTop. The rise of the resolution for IceTop tanks is believed to be connected with the events which saturate the array, which in this scenario is not the case for the scintillator array.

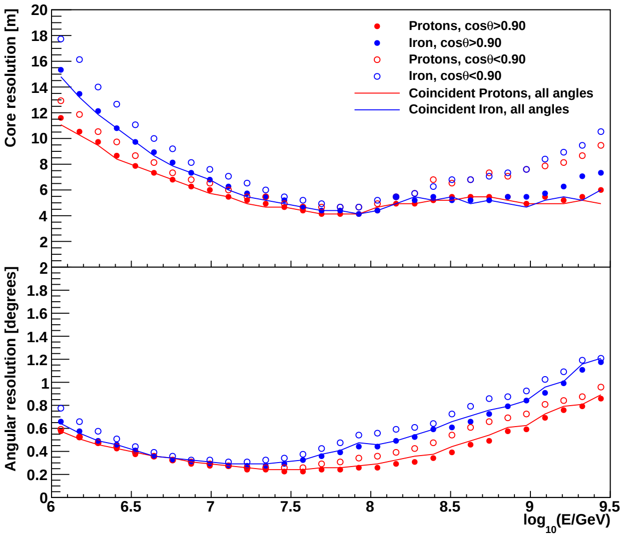

Figure 6.13: IceTop reconstruction performance. The upper panel shows core resolution and the lower angular resolution defined as 68th percentile of the underlying distributions. Different zenith angle ranges are depicted for proton and iron primaries. Figure is taken from [188].

Efficiency

Understanding the efficiency of the reconstruction is relevant in terms of verification of the procedure's stability as well as future high-level analysis of the cosmic ray spectra. For these two purposes a different definition of efficiency is formulated. In Figure 6.14 the efficiency for proton and iron showers is presented as a function of true energy where efficiency is calculated as the ratio of all the events which were successfully reconstructed (convergence with proper values for S_{ref} and β) and all generated showers within a fiducial area selected based on the true core values. Thus, these curves represent how well the reconstruction procedure works for different energies, having in mind that these cores and directions are inside the fiducial area, within the uncertainty given by the resolution plots.

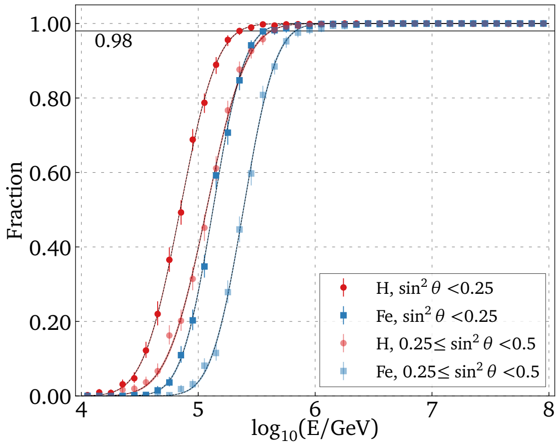

Figure 6.14: The efficiency of air shower reconstruction with folded trigger efficiency as a function of energy within MC fiducial area without selection on reconstructed cores and zenith angles.

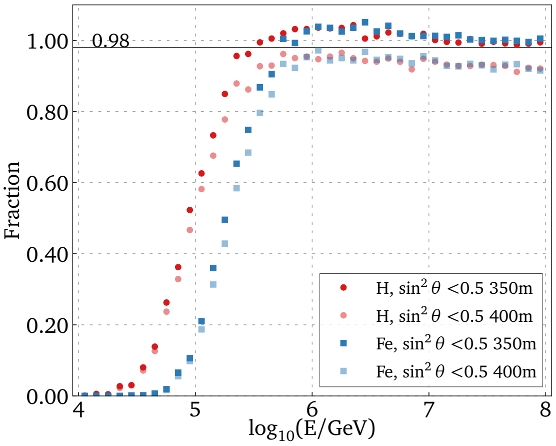

Figure 6.15: Efficiency of air shower reconstruction with folded trigger efficiency as a function of energy, taken with respect to the reconstructed core and direction within the fiducial area after containment cuts (see section 6.3.)

However, for the analysis of the cosmic ray spectrum one needs to know how many air showers will remain reconstructed within a given selection area. Hence efficiency is defined as the ratio of all air showers which are reconstructed within the fiducial area and pass all quality cuts over a number of all events which were truly generated within this selection area. This is depicted in Figure 6.15. Efficiency values above one originate exactly from this effect of mis-reconstruction, on one hand excluding air showers which are wrongly reconstructed outside the array, and on the other including the ones mis-reconstructed inside the array. This is not compensating each other as the area inside is smaller than the one outside. Increasing this area will cause a drop in the efficiency, since a shower on the edge of the array will be not properly reconstructed and shall be excluded from the analysis. What, however, is essential, is the estimation of the threshold, within which the statistical fluctuations stays the same.

Influence of showers falling outside the array

Due to the large footprint of the air showers of the highest energies, some events which impact outside of the array, can still trigger a significant number of detectors. Some of them will have a core properly reconstructed outside of the array and will not be included in the analysis. However, it can happen that these events will be mis-reconstructed inside the fiducial area. Since the array would then record only part of the shower footprint, the core position would be effectively pulled towards the center of the array. The effect causes also a mis-determination of shower energy, resulting in a worse energy resolution. Thus, it is relevant to understand how significantly this can affect the performance of the above presented reconstruction, where the core was simulated only within 500 m from the center.

Based on the results obtained from the reconstruction, a parametrised model of the air shower footprint was prepared. The 50000 air-shower events, with a given energy and direction, were generated using the inverse random sampling method, covering the relevant ranges of the reconstruction parameters. Based on the trigger probability of the expected LDF signals (see Figure 6.1), the decision on the single detector trigger is determined by inverse sampling of a Bernoulli distribution. Such a model of an air shower is considered to trigger the array if at least 3 detectors were triggered. The model was verified against the trigger efficiency curve obtained from the full Monte Carlo. The following radii for the triggering were obtained, giving a trigger probability larger than 30%: 600 m for 0.1–1 PeV., 800 m for 1–10 PeV and 1000 m for 10–100 PeV.

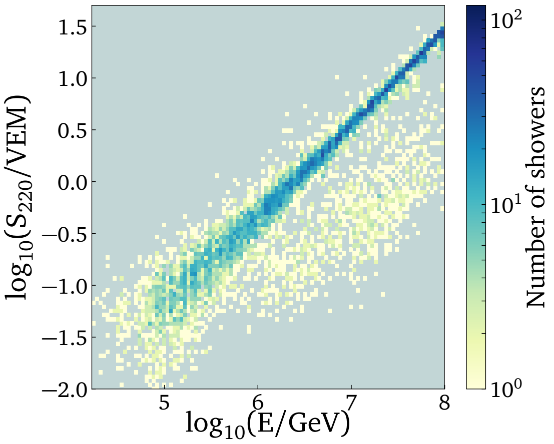

Figure 6.16: Distribution of S_{220} for H induced air showers including air showers far away from the center of the array. The cluster of points at the higher energies corresponds to air showers which triggered the array but due to their core outside, were wrongly mis-reconstructed as showers of lower energy.

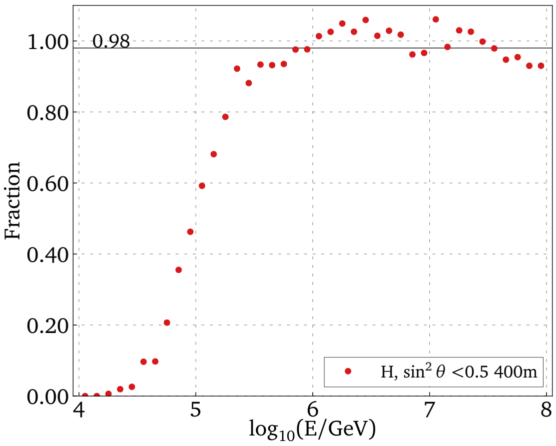

Figure 6.17: The efficiency of air shower reconstruction with folded trigger efficiency as a function of energy, taken with respect to the reconstructed core and direction within the fiducial area after the containment cuts which removes the cluster from the distribution depicted in the left plot.

The main influence of such showers is shown in Figure 6.16, depicting the reconstructed S_{220} with respect to true energy. However, the spot of mis-reconstructed un-contained events can be removed with some refined quality cuts, like the ones applied by the IceTop analysis. The one applied to efficiency in Figure 6.17 excludes events which have the largest signal at outer area of the scintillator array and a maximum signal smaller than 1 VEM.

The results of the reconstruction efficiency taken with respect to the reconstructed core range of 400 m from the array center are presented in Figure 6.17. The probability above 1 is connected to events which are wrongly reconstructed inside the array. Clearly the influence of events with core placed even further from the array centre is very visible, resulting in the large fluctuations also at the higher energies. Thus a deeper analysis needs to be performed improving the influence of the quality cuts without rejecting well reconstructed showers.

6.4 Items to consider

Within the scope of this thesis, the standard analysis of the air showers for the scintillator array was performed. Due to the early stage of this experiment, there are still many unknowns which will need to be included and considered in the analysis in the future. Moreover, the analysis itself offers many places for improvements. For example, treating the lowest energy air-showers with different minimisation settings may improve the resolution and the fit stability in this region. Although quite some effort was spent to optimise the procedure for all showers, certainly more systematic studies can be done. In addition, the reconstruction accuracies might be slightly worse once the realistic relative altitudes of the detectors are included, instead of equal heights for all scintillators. However, since the z-coordinate is not being reconstructed, the change should be small. For the direction accuracy a time correction would be applied what will make this effect rather negligible.

Chapter summary

The framework for the scintillator reconstruction and basic air shower analysis have been established. The simulation study indicates a good resolution of shower core and direction. Different energy estimators were studied to minimise the dependence on the primary mass and at the same time keep the uncertainties small.

Chapter 7

TOWARDS COSMIC-RAY MASS SEPARATION

A validation of the astrophysical models describing the cosmic-ray sources and acceleration mechanisms requires a precise measurement of energy spectra of individual masses or at least mass groups. This subsequently requires a primary mass determination on an event-by-event basis, which is the most difficult task in interpreting the data of air-shower experiments. However, it has been shown that a great potential to improve this situation is given by the detection of different shower components using hybrid arrays [189]. The foreseen IceTop enhancement with the scintillation detectors and radio antennas in operation together with IceTop and IceCube will be an excellent example of such an approach.

Due to differences in the development of the extensive air showers, the number of secondaries of a given type and their longitudinal and lateral spreads vary from proton to iron primaries. This results in variations in the characteristics of the signal and time distributions on the ground (see Chapter 5). Although the information about the primary species is convoluted in the development of the air shower and the response of the array, it is possible to infer the cosmic-ray nature via careful studies of the measured signals [83]. This path starts with understanding of a single detector's response to different particles (see Chapter 3). Based on this, a suitable design of the air-shower array needs to include the possibility to measure different secondary components in the context of their contribution to the overall signals and arrival times.

Across previous chapters, it has been proven that air showers induced by different primaries manifest distinguishable features. The showers induced by heavier primaries interact higher in the atmosphere, resulting in a smaller value of X_{max}, this in turn leads to a flatter lateral distribution seen at the ground. This link can be provided by the LDF slope parameter, or the age of the shower (discussed in Chapter 5). This is considered as an observable which manifest the correlation with the cosmic-ray mass as shown by many studies e.g. slope of NKG and Linsley functions separates the mass at ultra high-energies [190], using the mean square radius in scaling fromalism (HG-like function) [174]. Moreover, the air showers induced by heavier primaries produce more muons and slightly less electromagnetic particles. Such a ratio can be inferred from dedicated muon detectors buried underground, like in case of the Pierre Auger Observatory [191] or muon trackers like in the KASCADE experiment [192]. Also from the LDF fit the muon content in the air shower can be obtained, at least at large distances [105, 182].

All of these approaches use multiple detection channels to compare almost pure muon information with the major electromagnetic signal. Such hybrid measurements will also be possible with the extension of the IceTop array with the scintillator panels. The scintillation detectors are very sensitive to the electromagnetic component of the air shower, while muons often pass through, depositing very similar amount of energy. On the other hand, IceTop

Cherenkov tanks exhibit a more pronounced response to the muons, since muon trajectories inside a tank are longer. However, due to the overwhelming amount of photons coming from the air shower, the major contribution of the tank signals comes from photons, which can among other processes, scatter via Compton effect or produce $e^{\pm}$ pairs. These small differences on the level of the individual detector are magnified when a large fraction of the surface array detectors is triggered. Then, combining information from these two detector types can be of a great advantage, providing an insight into the air shower development. In addition, in the current stage, the IceTop tanks are covered with up to a few meters of snow. This makes it more difficult to disentangle the single particle component, but on the other hand it can reduce the signals coming from photons and show the muonic component even more distinctly. On contrary the electromagnetic part is still clearly detectable with uncovered scintillation detectors.

In the following sections, the first analysis of the air showers propagated through scintillator and tank arrays is discussed, based on the combined simulations. This aims to estimate the capabilities of the enhanced array on mass composition studies.

7.1 Reconstructions

Over the years, the IceTop groups have developed the standard algorithm and software for air shower reconstruction with Cherenkov tanks. Since the procedure used by scintillators utilizes the basics of the IceTop algorithm, only a reference to the full IceTop reconstruction is given [175]. The main project used there is called Laputop and provides the basic air shower observables, like shower core, time and direction as well as the LDF parameters, β and S_{ref} which, in case of IceTop, was chosen as the signal at the reference distance of 125 m. Although the new reconstruction framework was developed, and will allow in the near future to truly combine the scintillator and tank signals in one minimisation procedure, in the scope of this thesis the standard, Laputop based, IceTop reconstruction was used. This assures the consistency with the existing results for the IceTop reconstruction. In addition, this reconstruction includes a correction of an energy estimator with respect to the snow accumulation. In this work, $\lambda = 2.3$ was assumed.

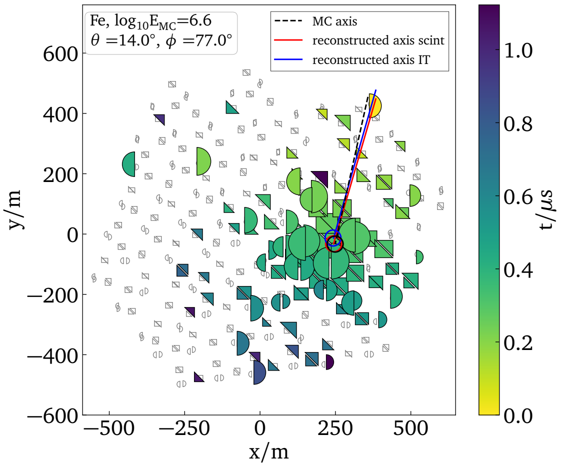

Figure 7.1: Example of the footprint of air shower initiated by iron primary of MC energy around 4 PeV and seen by IceTop (half circles) and scintillator array (triangles). The MC (black) and reconstructed by IceTop (blue) and scintillator array (red) shower core and projected axis are shown.

The reconstruction model for the scintillator array has been implemented in the RockBottom framework and the results were presented in Chapter 6. The results of these two separate reconstructions of the same simulated air showers were then combined into the discriminant analysis with the resulting parameters sensitive to the cosmic ray type. In Figure 7.1 an example of the signal footprint simulated through both detector arrays is depicted along with the core and axis reconstructed by these two arrays separately.

To assure the correctness of both reconstructions, the standard cuts on the events were applied. While for the scintillator array, the cuts are rather mild, some of the IceTop filters remove many air showers which are still quite well reconstructed with the scintillator modules. The procedure of the IceTop reconstruction was followed by the series of cleaning algorithms which are used to obtain a well-reconstructed set of IceTop simulations (described in [193, 194]). This, on one side, assures the consistency with other IceTop studies, but on the other hand significantly increases the energy threshold for this analysis. Therefore, in the future a relaxation of some of the IceTop cuts could be performed, in particular in context of a combined reconstruction at lower energies where these parallel cuts will not be needed any more. The following cuts have been applied:

- Both reconstructions converge (which includes the trigger requirements: 3 scintillator detectors and 6 HLC IceTop tanks in 3 stations, which is increased to 5 stations with HLC hits for IceTop reconstruction (see description in section 4.2)
- $1.4 \leq \beta_{\text{IceTop}} \leq 9$ and $1 \leq \beta_{\text{scint}} \leq 4.5$
- $\log_{10} S_{\text{IceTop}} \geq 0$ and $\log_{10} S_{\text{scint}} \geq -1$
- IceTop containment filter which assures that the air shower core is contained within the array without relaying on the reconstruction procedure (more details can be found in [193]) and related filters:
    - the IceTop station with the highest signal is not at the edge of the array
    - the largest signal is ≥ 6 VEM
    - the neighbouring tank of the largest signal station is ≥ 4 VEM
- To exclude poor reconstruction of small air showers, the events with less than 20% of the triggered detectors around the shower core are rejected (based only on the IceTop reconstruction).

In the following analysis only events with true core within 500 m from the array center were simulated, hence, the effect of the edge events is rather small. The release of some of the IceTop cuts was tested and it does not significantly influence the findings. The selection of the air-shower cores and directions have been applied simultaneously to both reconstructions: core within 400 m from the center and zenith angle smaller than 45°.

7.2 Mass sensitive parameters

From the analysis of the signal lateral distributions it was shown that the LDF shape, represented by the β parameter slightly differs between different primaries (see Figure 5.6). The influence of this variable in IceTop analysis has also been studied [194]. The main differences originate from the depths of the maximum of the shower development which is higher in the atmosphere for heavier primaries. The distribution of the slope parameters as a function of (here vertical) X_{max} for proton and iron air showers, for scintillators (left) and IceTop (right) is depicted in Figure 7.2. The clear relation can be seen. The separation between two types of cosmic rays is rather low, nevertheless it can be a significant input to the combined analysis. The estimates of vertical X_{max} have been taken from CORSIKA fit. The values of the fit below the observation level carry large uncertainties.

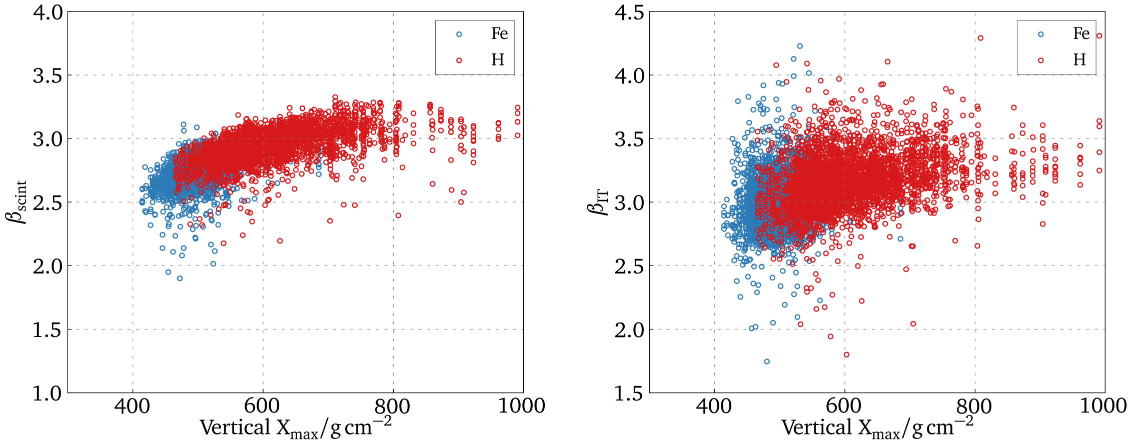

Figure 7.2: The distribution of the reconstructed LDF slopes, β, with respect to X_{max} along vertical depth for scintillator reconstruction (*left*) and IceTop (*right*) for H and Fe induced air showers in the energy range from 10^7 GeV to $10^{7.5}$ GeV and zenith angle up to 30° (scintillators). The concentration of the values along lines is connected to sampling one shower multiple times over the array, and they also indicate how differently the same shower might be reconstructed.

In Figures 7.3 the values of this slope for proton and iron induced air showers are presented, for IceTop (right) and scintillator array (left). The differences for the IceTop slope are rather small and in a statistical analysis difficult to resolve on an event-by-event basis. In the case of scintillator modules, the separation is a bit more powerful and can constitute a valuable input in the combined discrimination.

As it was mentioned above, the other key information about the air shower is a ratio between the muon and electron number or at least their relative contributions. Since neither IceTop, nor scintillators can distinguish between the particle types, an overall description of the signal distribution must be attempted to infer these contributions due to different response of detectors to those components. Thus, different ratios of reconstructed LDFs from the IceTop tanks and the scintillators were studied as a possible mass-sensitive parameter. It has been found that at some distances the separation between proton and iron samples increases, for instance at the distance around 200 m.

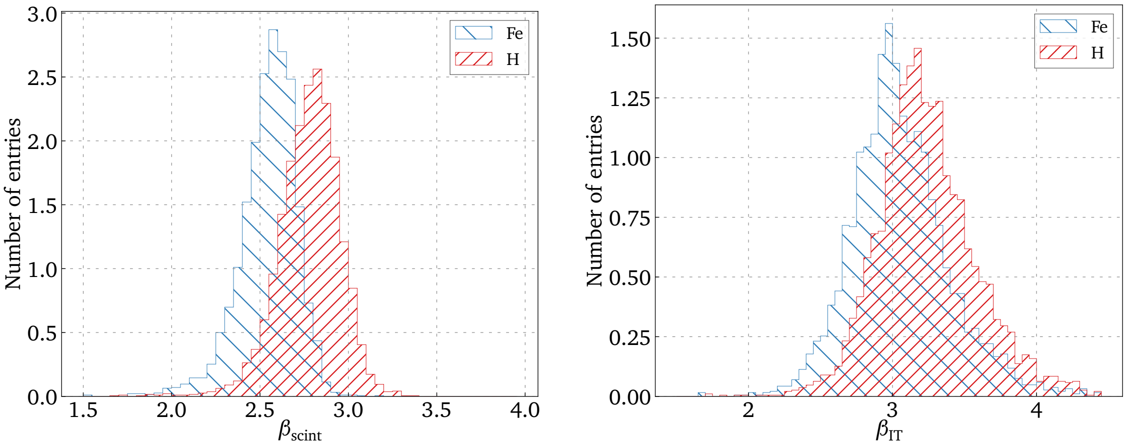

Figure 7.3: The distribution of the reconstructed LDF slopes, β, for scintillator reconstruction (left) and IceTop (right) for H and Fe induced air showers in the energy range from $10^{6.5}$ GeV to 10^{7} GeV and zenith angle up to 30° (scintillators). The separation between the two primaries is visible.

The contribution from the μ and $e^{\pm}$ (no γ) to the number of PEs generated in a given detector was analysed for both arrays as a function of the lateral distance. For this plot, no cleaning of the simulated pulses was applied, only corresponding triggering cuts and a simple transformation to VEM was used. The results shown in Figure 7.4 indicate an interplay of two effects. Namely, the scintillation detectors measure mainly the electromagnetic part close to the shower axis, while the IceTop tanks are more sensitive to muons at larger distances. However, the contribution from photons is the most significant in the tank signals in the region closer to the shower axis. The differences between $\mathrm{e}^{\pm}$ and muonic contributions for the two arrays are shown in the lower panel. Around 200 m, for this particular energy range, the values indicate an optimal relative difference, taking into account that the contributions from less dominating particles for two detector arrays are lower. A value in that range can be sensitive to the relative differences in signal distributions, emerging from the cosmic ray mass.

Therefore as parameters for a mass discrimination study, the slope parameter β as well the LDF ratio at 200 m are used in a discriminant analysis discussed in the next section. For future studies, more parameters can be included in a multi-dimensional analyses. However, because of the high correlation of the many measurable parameters which describe air-shower development, inclusion of additional parameters does not always increase the separation power.

7.3 Discriminant analysis

The power of a separation between two samples given the distributions of their parameters, can be estimated using a linear discriminant analysis, also called a Fisher discriminant analysis [195]. The main idea is to decrease the number of dimensions given by multiple parameters to one while maximising the separation. An alternative method often used in this kind of analysis is a principal component analysis. These two approaches essentially differ in a way

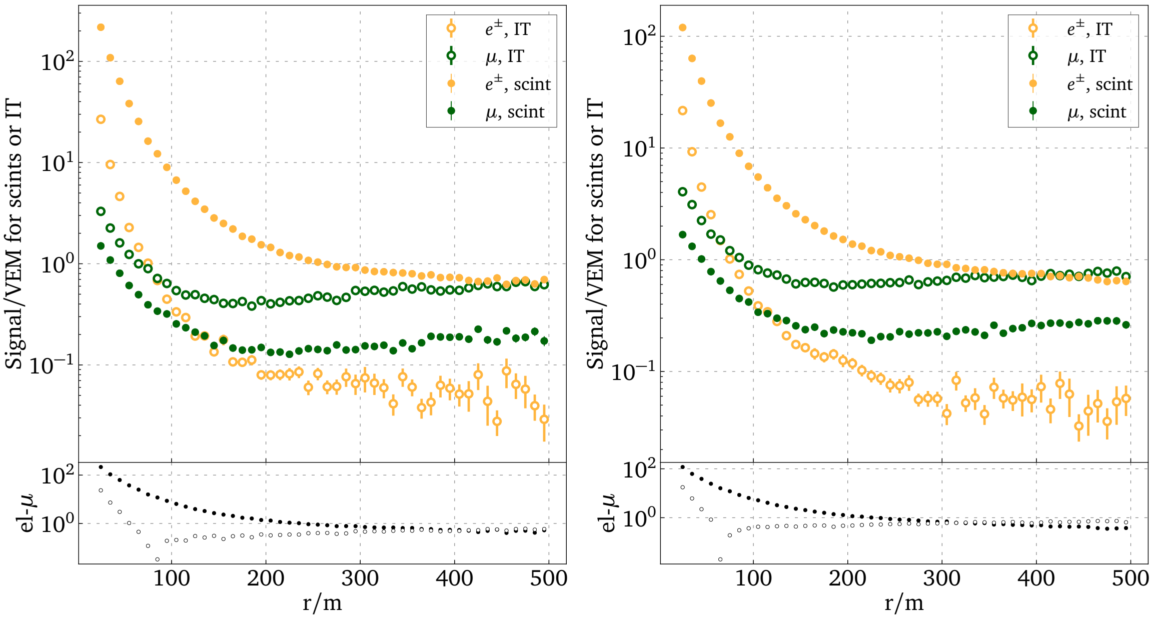

Figure 7.4: The average number of VEMs generated in tanks (IT) and scintillators (scint) after a simple transformation from the number of PEs for H (*left*) and Fe (*right*) induced air showers in the energy range from 1 to 10 PeV and zenith angle up to 30°. The differences between muonic and e$^{\pm}$ contributions are depicted for two arrays. Silent detectors are not included in the average.

of finding the discrimination values. The Fisher analysis tries to find a characteristic part of the distribution which increases the discrimination between two classes of samples, while the principal analysis looks for a general direction of separation without their classification.

The presented results of discrimination power were obtained with a linear discriminant analysis tool from the scikit-learn package [196], where all essential calculations are performed. However, an independent cross-check of these results was performed using an analytical solution [197]. It is important to notice that the linear analysis assumes a Gaussian distribution of a parameter's sampled values, which slightly deviates from the given parameter distributions. However, it still gives a good separation in the terms of the Fisher value. Moreover, the Gaussian distributions are good approximations of the actual distributions which are unknown.

Following the approach of other cosmic-ray experiments, like in the Pierre Auger Collaboration [13], the separation power in one dimension can then be quantified using a parameter called figure of merit (FOM):

$$\eta_{\mathrm{FOM}} = \frac{|\mu_H - \mu_{Fe}|}{\sqrt{\sigma_H^2 + \sigma_{Fe}^2}}, \tag{7.1}$$

where μ_H and μ_{Fe}, σ_H and σ_{Fe} are mean and standard deviations respectively for two samples, in this case proton and iron primaries.

The resulting distribution from the Fisher analysis is depicted in Figure 7.5 and 7.6 for two ranges of energies ($10^{6.5}$ GeV–10^{7} GeV and 10^{7} GeV–$10^{7.5}$ GeV respectively) and quasi-vertical showers ($\sin^2\theta < 0.25$, scintillators). The values of around 1.28 for the lower energies and 1.75 for higher energies are quite promising. It allows for obtaining light and heavy samples close to the knee region. At higher energies the separation is even more powerful and even some medium mass groups could be considered in future analyses.

The results prove that small differences in the detector-array responses can be magnified when combining two detection channels, which are differently sensitive to the air shower components. The separation shows the performance of this approach only for proton and iron primaries, allowing for separation into light and heavy elemental groups. Dissecting individual masses, especially at lower energies, will require more studies on the possible parameters and their correlations or application of more advance techniques of classification, by deep learning methods for example.

In the mass composition analysis the reconstruction characteristics, like resolution of primary energy and direction, will have to be carefully taken into account, since these resolutions are mass dependent. This can introduce additional spread of the parameters or even systematic biases.

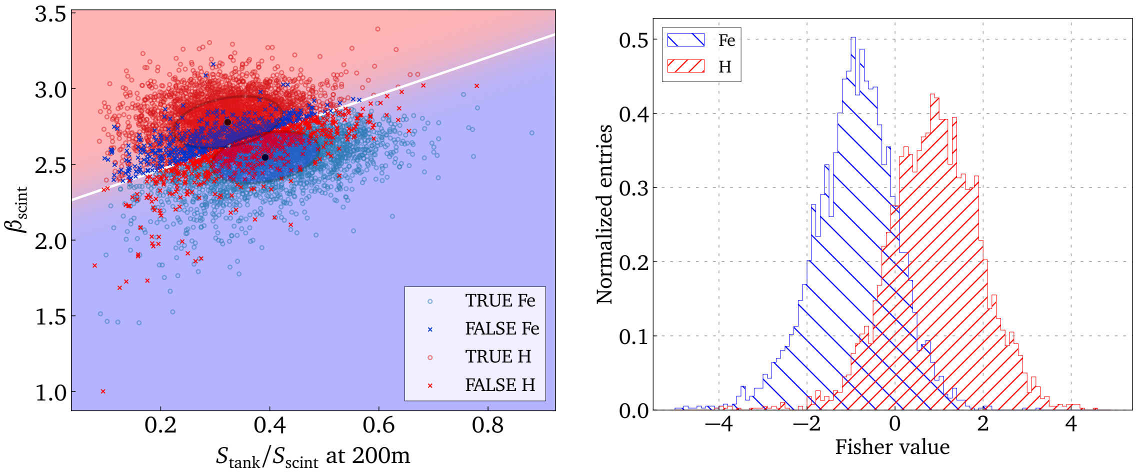

Figure 7.5: Distribution of the parameters reconstructed by IceTop and the scintillator arrays for proton and iron induced air showers (*left*) in the true energy bin of $10^{6.5}$ GeV–10^7 GeV. The ellipses indicate a 1 sigma contour of a given distribution and black dot its center. The discriminant analysis (*right*) results in a FOM of 1.28 as separation power.

7.4 Discussion

A better separation power can still be achieved in the future with a more detailed exploration of the possible parameter space for both arrays. Moreover, a combined reconstruction method could also give an improvement, once the differences and biases from two arrays are reduced by a simultaneous fit to all distributions. Optimisation of multiple spatial and temporal distributions at the same time can improve the resolutions of the underlying parameters, since IceTop and the scintillator array reconstructions show better performance for different cosmic-ray observables. In the combined minimisation of the negative log-likelihood, the weighting can be applied to magnify the importance of one distribution over the other.

The revision of the applied quality cuts given by the IceTop reconstruction is crucial for the

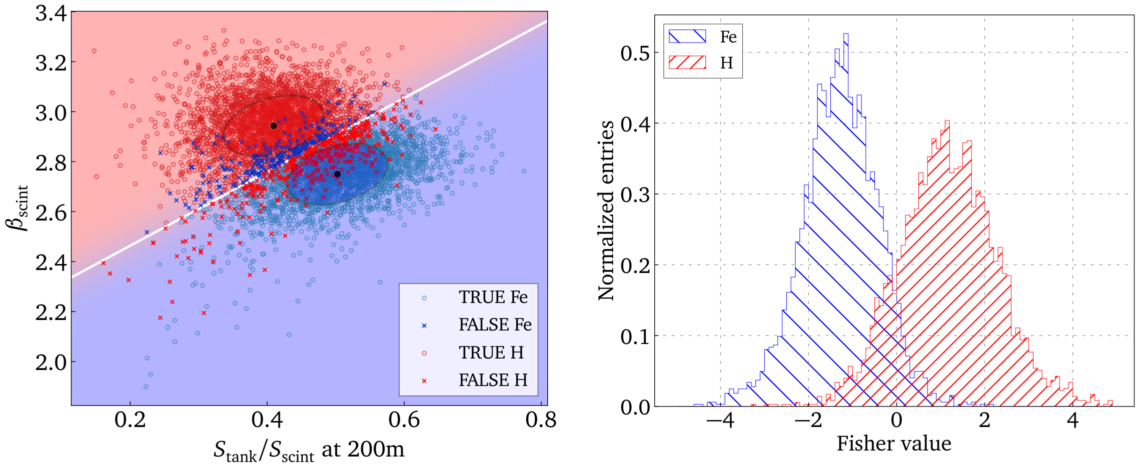

Figure 7.6: Distribution of the parameters reconstructed by IceTop and the scintillator arrays for proton and iron induced air showers (*left*) in the true energy bin of 10^7 GeV–$10^{7.5}$ GeV. The ellipses indicate a 1 sigma contour of a given distribution and black dot its center. The discriminant analysis (*right*) results in a FOM of 1.75 for as separation power.

analysis of the region below the knee in the cosmic ray spectrum. Lowering the energy of the mass-composition measurements requires some compromise in the analysis between high-purity, high-energy sample and low-multiplicity, low-energy sample of events.

Chapter summary

Due to the complementary response to secondary particles, the scintillation detectors and the IceTop tanks together can improve the mass discrimination of cosmic rays. This first analysis of the combined array shows the potential of this approach by using the slope of scintillator LDF together with the ratio of the IceTop array and the scintillator array lateral distribution functions at 200 m distance to the shower axis.

SUMMARY

Hundreds or millions of light years away from Earth, powerful astrophysical objects accelerate particles and nuclei to very high energies. Such high-energy cosmic rays travel for a long time confined - in and scattered - by magnetic fields, which limits the information about their origin we can infer at Earth. The imprints of the information of the source, acceleration and propagation of cosmic rays are encoded in changes and other features in the overall rapidly decreasing power law spectrum of the primary cosmic rays.

The explanation of the observed spectral features is not straightforward. The apparent prominent changes in the mass-composition of the flux in the energy range from 100 TeV to 1 PeV can be correlated both to the processes at the acceleration site itself, and also to the cosmic-ray propagation in the interstellar medium. As mentioned in the first chapters, significant evidence, supporting the hypothesis of a rigidity dependent softening of the flux, inspired a large amount of cosmic-ray observatories to boost their mass sensitivity to dissect the all-particle spectrum into individual elemental groups. In this view the IceCube surface array, IceTop, will also be enhanced in coming years by an array of scintillation detectors. The IceTop array suffers large measurement uncertainties due to continuous snow accumulation, what diminishes its capability for cosmic-ray mass determination on an event-by-event basis.

The goal of this dissertation was to assess how the planned enhancement of the IceTop array could boost the cosmic-ray measurements to contribute to the progress of understanding the origin of high-energy cosmic rays. The main objectives are lowering the detection threshold below PeV to have a full coverage of this particular feature in the all-particle spectrum, called the knee, and improvement of the discrimination power of the primary cosmic ray species. The technical developments and fundaments of the analysis will be beneficial for the future data analysis and validation of the applied procedures. In fact, they have been already used in the analysis of the prototype station data, proving the capabilities of the deployed scintillation detectors.

Simulations The performed simulation study required an implementation of the new detector model and an optimisation of the existing software framework. Within the IceTop group exhaustive simulations of the detector response were performed including optical simulations of its components and then parametrised for large-scale simulations. Preliminary validation of the simulation results in the context of air showers have been performed against the experimental data from the prototype station at the South Pole.

The detector response was investigated to understand the differences between scintillator panels and IceTop tanks in the context of sensitivity to the different air-shower components. The next step was to optimise the layout of the modules within the IceTop footprint to meet several goals: lowering the air-shower detection threshold for the cosmic-ray measurements, minimising the deployment efforts which are challenging in the Antarctic environment, and potentially improving the veto capabilities for the in-ice measurements.

Reconstruction The main requirement of the air-shower analysis is a robust reconstruction of the observables of incoming cosmic rays. Thus, a classical analysis was performed for this new instrument, and tuned to the particular design to obtain reliable estimates. The cost and capability of the optimised layout were validated. A very good angular resolution has been achieved in the energy range where the detector is supposed to operate for quasi-vertical showers below 2° at 1 PeV and ten times lower at 100 PeV for all simulated primary types: H, He, O, Fe, and γ. The resolution of the shower core location is at the level of 20 m at PeV and reduces to 2.5 m at 100 PeV. In addition, a reliable energy estimator was found with a small bias towards different primary types, with a resolution of around 25% for few PeV and less at higher energies for quasi-vertical showers. The influence of mis-reconstructed events was also addressed in these studies.

These efforts were accompanied by the development of the new project of the IceCube software aiming a combined reconstruction of the multiple detector arrays. The scintillator reconstruction model was successfully implemented and will contribute to further developments of this project.

Combined instrument The last step of the analysis was the verification of the general considerations about the potential of the combined instrument in improving the mass separation on an event-by-event basis. For this purpose, the different parameters sensitive to the cosmic ray's mass were evaluated and merged from two independent IceTop and scintillator reconstructions. The combination of the parameters from two arrays was used to perform the first evaluation of the cosmic ray's mass discrimination in a hybrid mode. The main motivation behind them points to the different response of the scintillators and tanks to the electromagnetic and muonic components of the air showers, as well as the sensitivity of a single array to the air shower development. The significant enhancement of the mass discrimination was achieved by applying a discriminant linear analysis for events of a primary energy above 1 PeV.

Capabilities The current situation of the high-energy cosmic ray research gives confidence that despite very different detection techniques and varying analysis tools all measurements confirm the main spectral features. The planned enhancement of IceTop will improve the situation and will give new insights in this journey towards revealing the astrophysical origin of cosmic rays.

In particular, the increased sampling of the IceTop enhancement will allow for lowering the energy threshold for a dedicated composition study. The in-fill part of IceTop made first attempts to reach the energies where the direct techniques operate, since an overlap in the flux measurements is crucial in assessing the absolute energy scale of the spectrum. In Figure 7.7 the results from the IceTop low-energy analysis is presented. The low statistics and high uncertainties make it difficult to resolve fine features of the spectrum. It is remarkable that the scintillator extension of IceTop will cover the broad band of energies from below PeV to above 100 PeV. The targeted region is marked in this Figure.

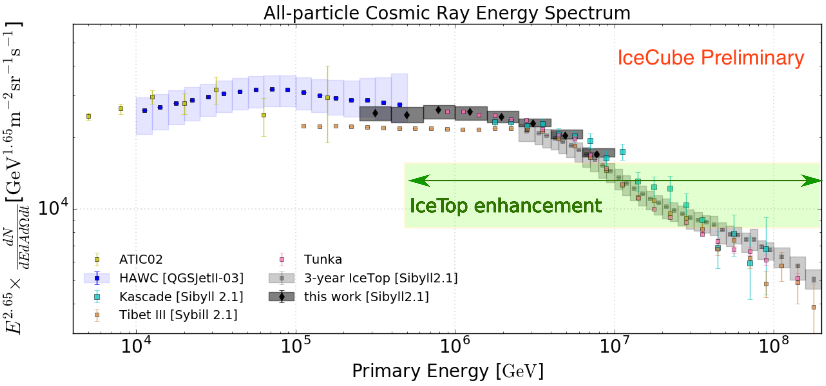

Figure 7.7: The all-particle spectrum covering high-energy cosmic rays measured by different ground and balloon based experiments. The higher energies were observed by IceTop, KASCADE and Tibet, while the lower by the IceTop in-fill array, HAWC or Tunka. The IceTop enhancement with the scintillation detectors will cover a broad range of energies from below PeV to EeV with a high capability for composition studies. Figure was adopted from [163].

The scintillator array will provide the complementary measurement of the first and second knee seen by KASCADE-Grande [85] and Tunka-133 [198] or low-energy extensions of Auger [199] and Telescope Array [200], comprehensively covering this energy region. The advantage of the new installation is the higher altitude of IceTop, which results in larger sensitivity to changes in the air-shower development. By employing hybrid detectors and utilising the measurements of the in-ice array as a 3D cosmic-ray detector it will bring even more insight into the research topic [183].

Very promising progress happens in parallel in the Northern Hemisphere. The LHAASO experiment targets even lower energies up to hundreds of GeV and plans to detect primarily γ-induced air showers [201]. However, with somewhat similar, like aforementioned, objectives for the cosmic rays, it will provide a complementary coverage of the sky with respect to the South Pole.

The IceTop enhancement will clearly take a significant step not only in the cosmic-ray measurements but in general in multi-messenger observations. On one hand the scintillator array will provide a trigger for radio antenna array detecting galactic photons, and on the other hand due to the increased coverage of the IceCube surface it will improve together with IceTop tanks the efficiency of vetoing the atmospheric background for the astrophysical neutrino measurements.

Outlook Despite broad efforts to bring this analysis from the level of idea about the possible enhancement to the actual set of estimated capabilities, there is still room for improvements and validations.

The simulation software can be further optimised in the context of transparency for the end-user as well as general technical review. Moreover, a systematic cross check with the calibration and full-operation data would be desirable. This will also verify all assumptions made in the simulations. The reconstruction procedure is highly sensitive to different changes in the parameter space. Hence, more refined studies of their influence could improve a robustness and reliability in terms of the parameter estimation. In particular, the threshold region is challenging in obtaining the stable performance of the reconstruction. At these energies, air showers leave a smaller and sparser footprint and hence a special care needs to be taken for their analysis. A larger set of simulations could bring a better understanding of the reconstruction influence on the threshold region and essential quality cuts. Finally, the mass-separation potential is probably higher since only the preliminary analysis was performed in the scope of this work. Further progress is ahead opening very new perspectives for IceTop cosmic ray measurements in particular, and high-energy astroparticle physics in general.

Appendix A

SECONDARY HADRON SPECTRA FROM CORSIKA SIMULATIONS

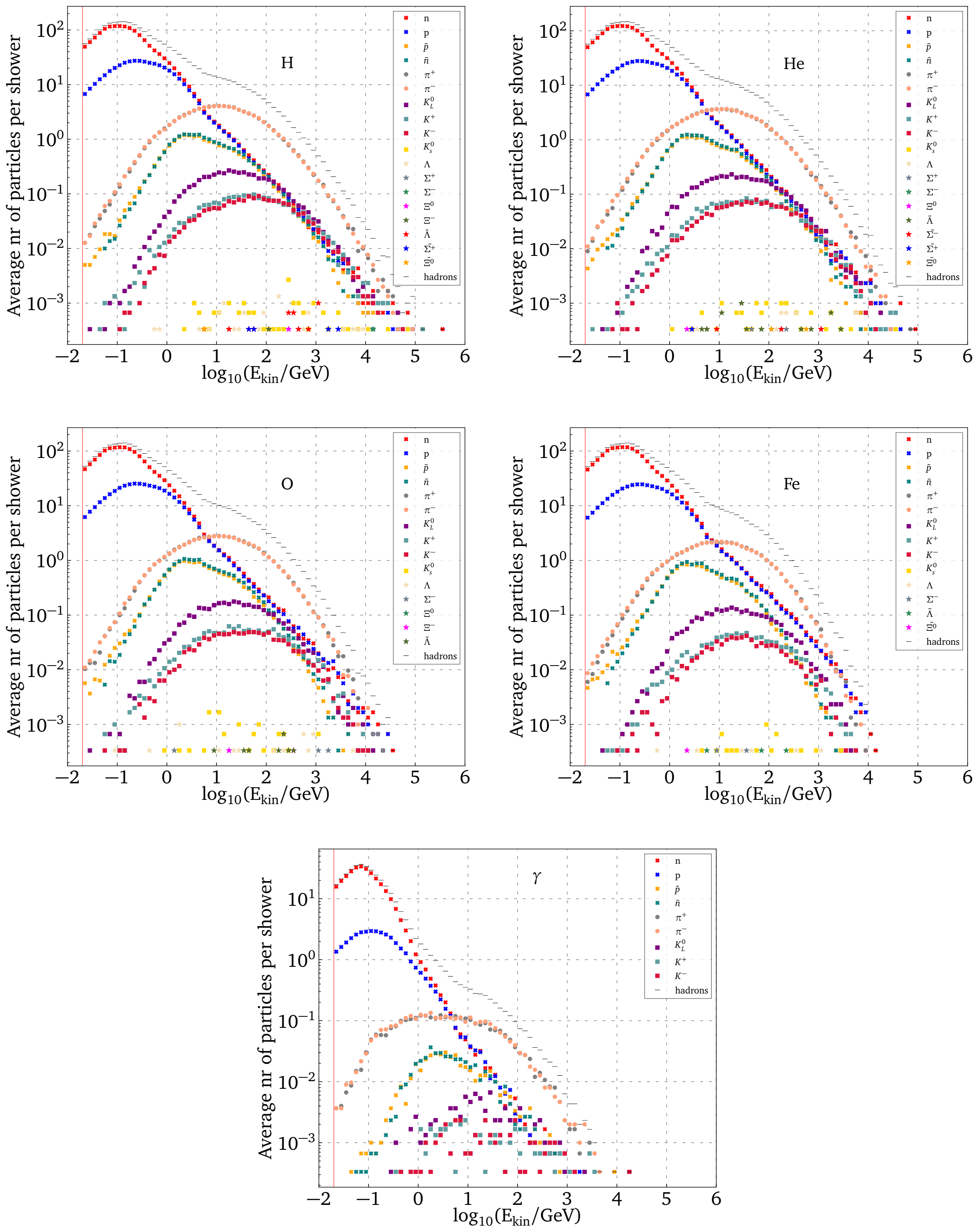

Figure A.1: Energy distribution of hadrons with single contribution for H, He, O, Fe and γ primaries with energy from 10^{14}-10^{15} eV taken at the South Pole observation level of 2842 m.

The spectra of secondary hadrons from CORSIKA simulations are depicted in Figure A.1 for H, He, O, Fe and gamma-ray induced air showers respectively. The shape of the spectra is revealed by single hadron components. At lower energies the main contribution comes from neutrons and protons. The second peak is dominated by charged pions. Fractions of anti-proton and anti-neutron are also significant. Other hadrons contribute rather insignificantly to the total spectrum at the ground.

Appendix B

THE GEANT4 RANGE-CUTS

In the Geant4 software, cuts on the particle production were introduced. The cuts refer to the minimum distance the secondary particles need to travel to be produced. All particles which cannot travel this range are not generated. The cuts can be defined differently depending on the material and for particle types: γ, e^-, e^+ and protons.

The cuts defined for the IceTop tanks, might not be suitable for the scintillation detector simulations due to its very different geometries and response. The study of the trajectories in different materials would require separate detailed studies. Thus, some arbitrary sets of ranges were analysed in terms of signal distribution, which is the most important aspect for the air shower analysis. Taking into account the thickness of the scintillator bar as of 1 cm, a reasonable assumed range is 1 mm or lower. The curves for these cuts are depicted in Figure B.1. Although there are some variations, no significant bias is visible. However, the 0.1 mm cut caused a longer computation time, in particular in case of combining scintillator and tank simulations.

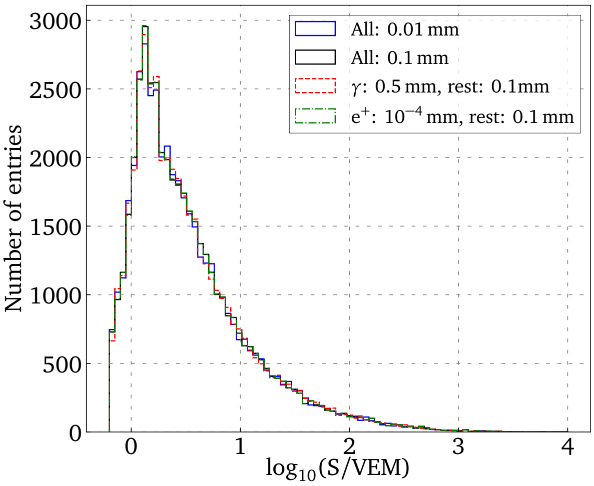

Figure B.1: Histogram of simulated signals in VEM units from 100 proton induced air showers sampled 10 times within the array. Signals are shown for 4 chosen sets of range cuts. The variations between different cuts are rather small.

Moreover, these range cuts can be expressed into the energy cuts for a given material. Assuming 0.1 mm for all particles shows that the energy limit on γs is much lower than on $e^{\pm}$ and proton. Therefore, γ range was increased in comparison to the other three types of particles. The increase of γ cut to 0.5 mm can be also seen in Figure B.1. In addition, the very low range cut on positrons was verified, as it was introduced by another group, but it gives a negligible difference with respect to the 0.1 mm cut for all particles. Therefore, 0.5 mm for photons and 0.1 mm for $e^{\pm}$ and protons are chosen for all materials. However, possibly in the future a material dependence could be studied and introduced if found to be relevant for the final energy deposition.

Appendix C

FIRST COMPARISON OF SIMULATION AND DATA

In the austral summer 2018/19 two prototype scintillator stations were installed. Data from one of them were analysed and compared with the simulation results applied to one station. The analysis was performed in the scope of bachelor thesis within our group [113]. The events detected in coincidence with IceTop were reconstructed with the IceTop giving an estimated range of their direction and energy. Using these results, the response of one station was simulated. The measured and simulated air showers were reconstructed using the simple algorithms of center of gravity and plane shower front.

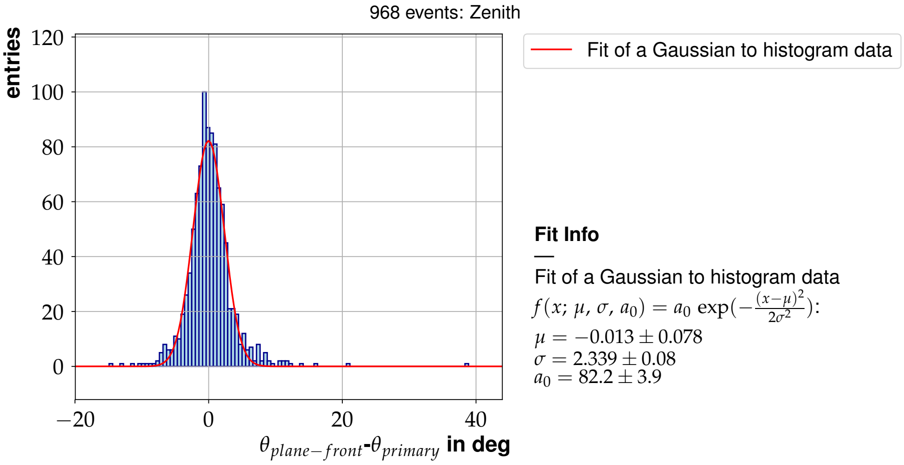

Figure C.1: Differences between zenith angles obtained from reconstruction of the measured and simulated signals of the scintillator station.

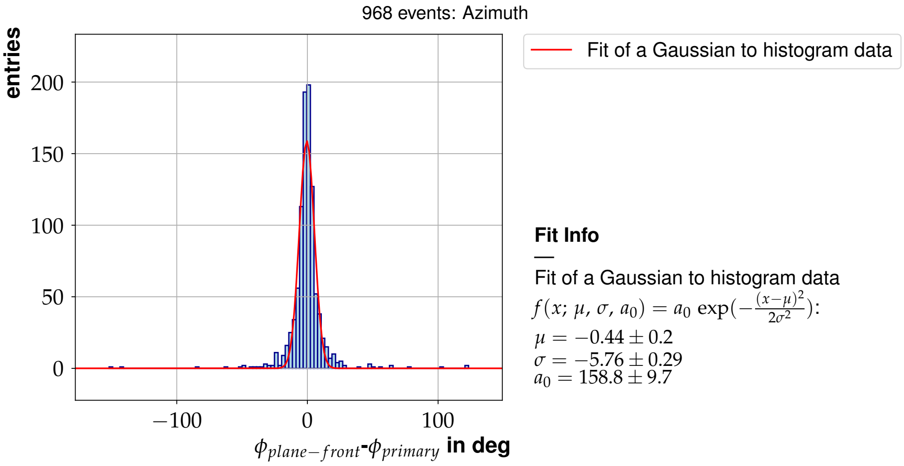

Figure C.2: Differences between azimuth angles obtained from reconstruction of the measured and simulated signals of the scintillator station.

The comparison is shown in Figure C.1 and C.2 depicting the difference between zenith and azimuth angles, respectively, reconstructed based on measured and simulated signal distributions. Each of the distributions was fitted with Gaussian and obtaining widths indicate the level of agreement between simulations and measured data. Zenith angle differs between both around 2°, while the azimuth around 6°. Including some differences in parameters between simulated and measured events this gives good agreement and indicates a capability of the scintillator reconstruction to properly infer the air shower parameters, even with this simplified method.

BIBLIOGRAPHY

[1] K.M. Schure and A.R. Bell. “Cosmic ray acceleration in young supernova remnants”. In: *Mon. Not. Roy. Astron. Soc.* 435 (2013), p. 1174. DOI: 10.1093/mnras/stt1371. arXiv: 1307.6575 [astro-ph.HE].

[2] W. Baade and F. Zwicky. “Cosmic Rays from Super-Novae”. In: *Proceedings of the National Academy of Sciences* 20.5 (1934), pp. 259–263. ISSN: 0027-8424. DOI: 10.1073/pnas.20.5.259.

[3] T K Gaisser. “The Cosmic-ray Spectrum: from the knee to the ankle”. In: *Journal of Physics: Conference Series* 47 (2006), pp. 15–20. DOI: 10.1088/1742-6596/47/1/002.

[4] G.V. Kulikov and G.B. Khristiansen. “On the Size Spectrum of Extensive Air Showers”. In: *JETP* 35 (8).3 (1959), p. 441.

[5] M. Amenomori et al. “The All-Particle Spectrum of Primary Cosmic Rays in the Wide Energy Range from 1014to 1017eV Observed with the Tibet-III Air-Shower Array”. In: *The Astrophysical Journal* 678.2 (2008), pp. 1165–1179. DOI: 10.1086/529514. URL: https://doi.org/10.1086%2F529514.

[6] M. Tanabashi and et al. (Particle Data Group). In: *Phys. Rev. D* 98 030001 ((2018) and 2019 update).

[7] Jörg R. Hörandel. “Models of the knee in the energy spectrum of cosmic rays”. In: *Astroparticle Physics* 21.3 (2004), pp. 241 –265. ISSN: 0927-6505. DOI: https://doi.org/10.1016/j.astropartphys.2004.01.004.

[8] Julia Becker Tjus and Lukas Merten. “Closing in on the origin of Galactic cosmic rays using multimessenger information”. In: *Physics Reports* 872 (Aug. 2020), pp. 1–98. DOI: 10.1016/j.physrep.2020.05.002. arXiv: 2002.00964 [astro-ph.HE].

[9] B. Peters. “Primary cosmic radiation and extensive air showers”. In: *Il Nuovo Cimento (1955-1965)* 22.4 (Nov. 1961), 800–819. DOI: 10.1007/BF02783106.

[10] Andreas Haungs et al. “Investigating the 2nd knee: The KASCADE-Grande experiment”. In: *J. Phys. Conf. Ser.* 47 (2006), p. 238. DOI: 10.1088/1742-6596/47/1/029. arXiv: astro-ph/0508286.

[11] A. Aab et al. “Large-scale Cosmic-Ray Anisotropies above 4 EeV Measured by the Pierre Auger Observatory”. In: *The Astrophysical Journal* 868.1 (2018), p. 4. DOI: 10.3847/1538-4357/aae689.

[12] A M Hillas. “Can diffusive shock acceleration in supernova remnants account for high-energy galactic cosmic rays?” In: *Journal of Physics G: Nuclear and Particle Physics* 31.5 (2005), R95–R131. DOI: 10.1088/0954-3899/31/5/r02.

[13] Alexander Aab et al. “The Pierre Auger Observatory Upgrade - Preliminary Design Report”. In: (2016). arXiv: 1604.03637 [astro-ph.IM].

[14] Chao Hou et al. “Finalized design of LHAASO electromagnetic particle detector”. In: *PoS* ICRC2019 (2020), p. 286.

[15] Charles C. H. Jui. “Results from the Telescope Array Experiment”. In: *Nucl. Part. Phys. Proc.* 273-275 (2016), pp. 440–445. DOI: 10.1016/j.nuclphysbps.2015.09.064.

[16] Matt Kauer et al. “The Scintillator Upgrade of IceTop: Performance of the prototype array”. In: *PoS* ICRC2019 (2020), p. 309. arXiv: 1908.09860 [astro-ph.HE].

[17] Katherine Rawlins. "A Function to Describe Attenuation of Cosmic Ray Air Shower Particles in Snow". In: *PoS* ICRC2015 (2016), p. 628. DOI: 10.22323/1.236.0628.

[18] D. Pacini. "La radiazione penetrante alla superficie ed in seno alle acque". In: *Nuovo Cim* 3 (1912), pp. 93–100. DOI: https://doi.org/10.1007/BF02957440.

[19] Victor F. Hess. "Über Beobachtungen der durchdringenden Strahlung bei sieben Freiballonfahrten". In: *Phys. Z.* 13 (1912), pp. 1084–1091.

[20] J. Clay and H. P. Berlage. "Variation der Ultrastrahlung mit der geographischen Breite und dem Erdmagnetismus". In: *Naturwissenschaften* 20.37 (Sept. 1932), pp. 687–688. DOI: 10.1007/BF01494405.

[21] J. Clay. "Results of the dutch cosmic ray expedition 1933 VI. The variation of the penetrative power of the radiation with magnetic latitude. The energy distribution of the particles". In: *Physica* 2.1 (1935), pp. 299 –308. ISSN: 0031-8914. DOI: https://doi.org/10.1016/S0031-8914(35)90092-1.

[22] Bothe W. and W. Kolhörster. "Das Wesen der Höhenstrahlung". In: *Phys. Z.* 56.751–777 (1929). DOI: https://doi.org/10.1007/BF01340137.

[23] Thomas H. Johnson. "The Azimuthal Asymmetry of the Cosmic Radiation". In: *Phys. Rev.* 43 (10 1933), pp. 834–835. DOI: 10.1103/PhysRev.43.834.

[24] Marcel Schein, William P. Jesse, and E. O. Wollan. "The Nature of the Primary Cosmic Radiation and the Origin of the Mesotron". In: *Phys. Rev.* 59 (7 1941), pp. 615–615. DOI: 10.1103/PhysRev.59.615.

[25] Geiger H. Bothe W. "Über das Wesen des Comptoneffekts; ein experimenteller Beitrag zur Theorie der Strahlung." In: *Z. Physik* 32 (1925), 639–663. DOI: https://doi.org/10.1007/BF01331702.

[26] Luisa Bonolisa. "Walther Bothe and Bruno Rossi: The birth and development of coincidence methods in cosmic-ray physics". In: *American Journal of Physic* 79.11 (2011), pp. 1133–1150. DOI: https://doi.org/10.1119/1.3619808.

[27] Bruno Rossi. "Method of Registering Multiple Simultaneous Impulses of Several Geiger's Counters". In: *Nature* 636 (1930). DOI: https://doi.org/10.1038/125636a0.

[28] Bruno Rossi. "Misure sulla distribuzione angolare di intensita della radiazione penetrante all'Asmara". In: *Ricerca Scientifica* 5.1 (1934), pp. 579–589.

[29] B. Falkenburg and W. Rhode. *From Ultra Rays to Astroparticles*. Springer. 2012.

[30] Pierre Auger et al. "Extensive Cosmic-Ray Showers". In: *Rev. Mod. Phys.* 11 (3-4 1939), pp. 288–291. DOI: 10.1103/RevModPhys.11.288.

[31] Carl D. Anderson. "The Apparent Existence of Easily Deflectable Positives". In: *Science* 76.1967 (1932), pp. 238–239. ISSN: 0036-8075. DOI: 10.1126/science.76.1967.238.

[32] Seth H. Neddermeyer and Carl D. Anderson. "Note on the Nature of Cosmic-Ray Particles". In: *Phys. Rev.* 51 (10 1937), pp. 884–886. DOI: 10.1103/PhysRev.51.884.

[33] J. C. Street and E. C. Stevenson. "New Evidence for the Existence of a Particle of Mass Intermediate Between the Proton and Electron". In: *Phys. Rev.* 52 (9 1937), pp. 1003–1004. DOI: 10.1103/PhysRev.52.1003.

[34] D. H. Perkins. "Nuclear Disintegration by Meson Capture". In: *Nature* 159.4030 (Jan. 1947), pp. 126–127. DOI: 10.1038/159126a0.

[35] G. P. S. Occhialini and C. F. Powell. "Nuclear Disintegrations Produced by Slow Charged Particles of Small Mass". In: *Nature* 159.4032 (Feb. 1947), pp. 186–190. DOI: 10.1038/159186a0.

[36] G. D. Rochester and C. C. Butler. "Evidence for the Existence of New Unstable Elementary Particles". In: *Nature* 160.4077 (Dec. 1947), pp. 855–857. DOI: 10.1038/160855a0.

[37] Enrico Fermi. "On the Origin of the Cosmic Radiation". In: *Phys. Rev.* 75 (1949), pp. 1169–1174. DOI: 10.1103/PhysRev.75.1169.

[38] Arno A. Penzias and Robert Woodrow Wilson. "A Measurement of excess antenna temperature at 4080-Mc/s". In: *Astrophys. J.* 142 (1965), pp. 419–421. DOI: 10.1086/148307.

[39] R.H. Dicke et al. "Cosmic Black-Body Radiation". In: *Astrophysical Journal (U.S.)* 142 (July 1965). DOI: 10.1086/148306.

[40] Kenneth Greisen. "End to the Cosmic-Ray Spectrum?" In: *Phys. Rev. Lett.* 16 (17 1966), pp. 748–750. DOI: 10.1103/PhysRevLett.16.748.

[41] G.T. Zatsepin and V.A. Kuzmin. "Upper limit of the spectrum of cosmic rays". In: *JETP Lett.* 4 (1966), pp. 78–80.

[42] G. Clark et al. "An Experiment on Air Showers Produced by High-Energy Cosmic Rays". In: *Nature* 180.4582 (Aug. 1957), pp. 353–356. DOI: 10.1038/180353a0.

[43] John Linsley, L. Scarsi, and B. Rossi. "Energy spectrum and structure of large air showers". In: *7th International Cosmic Ray Conference (ICRC 1961) Kyoto, Japan, September 04-15, 1961*. [Submitted to: J. Phys. Soc. Jap.(1962)]. 1962.

[44] John Linsley, Livio Scarsi, and Bruno Rossi. "Extremely Energetic Cosmic-Ray Event". In: *Phys. Rev. Lett.* 6.9 (May 1961), pp. 485–487. DOI: 10.1103/PhysRevLett.6.485.

[45] John Linsley. "Evidence for a Primary Cosmic-Ray Particle with Energy 10^{20} eV". In: *Phys. Rev. Lett.* 10 (4 1963), pp. 146–148. DOI: 10.1103/PhysRevLett.10.146.

[46] John Linsley. "The cosmic ray spectrum above 10^{19}-eV at Volcano Ranch and Haverah Park". In: *19th International Cosmic Ray Conference*. Feb. 1986.

[47] A. V. Glushkov et al. "Cosmic Ray Spectra Measurements at the Yakutsk EAS Array". In: *Proceedings from the 19th International Cosmic Ray Conference, Volume 2 (OG Sessions)*. 1985, p.198.

[48] R.M. Baltrusaitis et al. "The Utah Fly's Eye detector". In: *Nuclear Instruments and Methods in Physics Research Section A: Accelerators, Spectrometers, Detectors and Associated Equipment* 240.2 (1985), pp. 410 –428. ISSN: 0168-9002. DOI: https://doi.org/10.1016/0168-9002(85)90658-8.

[49] Antonella Castellina. "Highlights from the Pierre Auger Observatory". In: *PoS* ICRC2019 (2020), p. 004. eprint: 1909.10791.

[50] Shoichi Ogio. "Telescope Array Experiment". In: *European Physical Journal Web of Conferences*. Vol. 208. European Physical Journal Web of Conferences. May 2019, p. 08002. DOI: 10.1051/epjconf/201920808002.

[51] D. J. Bird et al. "Detection of a Cosmic Ray with Measured Energy Well beyond the Expected Spectral Cutoff due to Cosmic Microwave Radiation". In: *Astrophysical Journal* 441 (Mar. 1995), p. 144. DOI: 10.1086/175344. arXiv: astro-ph/9410067 [astro-ph].

[52] T. Doi et al. “Characteristics of Giant Air Showers of Energies Around 50 EeV Observed by AGASA”. In: *International Cosmic Ray Conference*. Vol. 2. International Cosmic Ray Conference. Jan. 1995, p. 764.

[53] John N. Bahcall and Raymond Davis. “Solar Neutrinos: A Scientific Puzzle”. In: *Science* 191.4224 (1976), pp. 264–267. ISSN: 0036-8075. DOI: 10.1126/science.191.4224.264.

[54] F. Reines et al. “Evidence for High-Energy Cosmic-Ray Neutrino Interactions”. In: *Phys. Rev. Lett.* 15 (9 1965), pp. 429–433. DOI: 10.1103/PhysRevLett.15.429.

[55] C.V. Achar et al. “Detection of muons produced by cosmic ray neutrinos deep underground”. In: *Physics Letters* 18.2 (1965), pp. 196 –199. ISSN: 0031-9163. DOI: 10.1016/0031-9163(65)90712-2.

[56] M Aglietta et al. “On the Event Observed in the Mont Blanc Underground Neutrino Observatory during the Occurrence of Supernova 1987 a”. In: *Europhysics Letters (EPL)* 3.12 (1987), pp. 1315–1320. DOI: 10.1209/0295-5075/3/12/011.

[57] M.G. Aartsen et al. “Multimessenger observations of a flaring blazar coincident with high-energy neutrino IceCube-170922A”. In: *Science* 361.6398 (2018), eaat1378. DOI: 10.1126/science.aat1378.

[58] M.G. Aartsen et al. “IceCube Search for Neutrinos Coincident with Compact Binary Mergers from LIGO-Virgo’s First Gravitational-Wave Transient Catalog”. In: (Apr. 2020). arXiv: 2004.02910 [astro-ph.HE].

[59] Thomas K. Gaisser, Ralph Engel, and Elisa Resconi. *Cosmic Rays and Particle Physics*. 2nd ed. Cambridge University Press, 2016. ISBN: 9780521016469, 0521016460.

[60] Roberta Sparvoli. “Direct cosmic ray measurements at the 36th ICRC”. In: *ICRC 2019* (2019). URL: https://www.icrc2019.org/uploads/1/1/9/0/119067782/sparvoli_rapporteur_crd.pdf.

[61] Peter K. F. Grieder. *Extensive Air Showers - High Energy Phenomena and Astrophysical Aspects*. Springer, 2010.

[62] A. Bridgeman. “Determining the Mass Composition of Ultra-high Energy Cosmic Rays Using Air Shower Universality”. PhD Thesis. Karlsruhe Institute of Technology, 2018. DOI: 10.5445/IR/1000085504.

[63] H. J. Bhabha and W. Heitler. “The passage of fast electrons and the theory of cosmic showers”. In: *Proc. R. Soc. Lond. A* 159.898 (1937), pp. 432–458. DOI: 10.1098/rspa.1937.0082.

[64] L. Landau and G. Rumer. “The Cascade Theory of Electronic Showers”. In: *Proceedings of the Royal Society of London Series A* 166.925 (May 1938), pp. 213–228. DOI: 10.1098/rspa.1938.0088.

[65] J. Nishimura and K. Kamata. “The Lateral and Angular Distribution of Cascade Showers”. In: *Progress of Theoretical Physics* 5.5 (Sept. 1950), pp. 899–901. ISSN: 0033-068X. DOI: 10.1143/ptp/5.5.899.

[66] Jun Nishimura and Koichi Kamata. “On the Theory of Cascade Showers, I”. In: *Progress of Theoretical Physics* 7.2 (Feb. 1952), pp. 185–192. ISSN: 0033-068X. DOI: 10.1143/ptp/7.2.185.

[67] Koichi Kamata and Jun Nishimura. “The Lateral and the Angular Structure Functions of Electron Showers”. In: *Progress of Theoretical Physics Supplement* 6 (Feb. 1958), pp. 93–155. ISSN: 0375-9687. DOI: 10.1143/PTPS.6.93.

[68] J. Nishimura. “Theory of Cascade Showers”. In: *Kosmische Strahlung II / Cosmic Rays II*. Ed. by K. Sitte. Berlin, Heidelberg: Springer Berlin Heidelberg, 1967, pp. 1–114. ISBN: 978-3-642-46079-1. DOI: {10.1007/978-3-642-46079-1_1}.

[69] K. Greisen. “The Extensive Air Showers”. In: *Prog. Cosmic-ray Physics*. Ed. by J.G Wilson. Vol. III. 1956. Chap. 1, pp. 19–37.

[70] K Greisen. “Cosmic Ray Showers”. In: *Annual Review of Nuclear Science* 10.1 (1960), pp. 63–108. DOI: 10.1146/annurev.ns.10.120160.000431.

[71] Walter Heitler. *The quantum theory of radiation*. 3. ed. The international series of monographs on physics. Oxford: Clarendon Pr., 1954.

[72] J. Matthews. “A Heitler model of extensive air showers”. In: *Astroparticle Physics* 22.5 (2005), pp. 387 –397. ISSN: 0927-6505. DOI: https://doi.org/10.1016/j.astropartphys.2004.09.003.

[73] Tanguy Pierog. “Air Shower Simulation with a New Generation of post-LHC Hadronic Interaction Models in CORSIKA”. In: *PoS* ICRC2017 (2018), p. 1100. DOI: 10.22323/1.301.1100.

[74] J. V. Jelley et al. “Radio Pulses from Extensive Cosmic-Ray Air Showers”. In: *Nature* 205.4969 (Jan. 1965), pp. 327–328. DOI: 10.1038/205327a0.

[75] Franz Daniel Kahn, I. Lerche, and Alfred Charles Bernard Lovell. “Radiation from cosmic ray air showers”. In: *Proceedings of the Royal Society of London. Series A. Mathematical and Physical Sciences* 289.1417 (1966), pp. 206–213. DOI: 10.1098/rspa.1966.0007.

[76] G.A. Askar’yan. “Excess negative charge of an electron-photon shower and its coherent radio emission”. In: *Sov. Phys. JETP* 14.2 (1962), pp. 441–443.

[77] G. A. Askar’yan. “Coherent Radio Emission from Cosmic Showers in Air and in Dense Media”. In: *Soviet Journal of Experimental and Theoretical Physics* 21 (Sept. 1965), p. 658.

[78] Frank G. Schröder. “Radio detection of cosmic-ray air showers and high-energy neutrinos”. In: *Progress in Particle and Nuclear Physics* 93 (Mar. 2017), pp. 1–68. DOI: 10.1016/j.ppnp.2016.12.002. arXiv: 1607.08781 [astro-ph.IM].

[79] H. E. Bergeson, J. C. Boone, and G. L. Cassiday. “The Fly’s Eye. A Novel Technique for Sensing Extensive Air Showers”. In: *International Cosmic Ray Conference*. Vol. 8. International Cosmic Ray Conference. Aug. 1975, p. 3059.

[80] Bruce R. Dawson. “The importance of atmospheric monitoring at the Pierre Auger Observatory”. In: *European Physical Journal Web of Conferences*. Vol. 144. European Physical Journal Web of Conferences. Jan. 2017, p. 01001. DOI: 10.1051/epjconf/201714401001.

[81] Hans Peter Dembinski et al. “Data-driven model of the cosmic-ray flux and mass composition from 10 GeV to 10^{11} GeV”. In: *PoS* ICRC2017 (2018). [35,533(2017)], p. 533. DOI: 10.22323/1.301.0533. arXiv: 1711.11432 [astro-ph.HE].

[82] Thomas K. Gaisser. “Spectrum of cosmic-ray nucleons, kaon production, and the atmospheric muon charge ratio”. In: *Astroparticle Physics* 35.12 (2012), pp. 801 –806. ISSN: 0927-6505. arXiv: 1111.6675 [astro-ph.HE].

[83] Karl-Heinz Kampert and Michael Unger. “Measurements of the cosmic ray composition with air shower experiments”. In: *Astroparticle Physics* 35.10 (May 2012), pp. 660–678. DOI: 10.1016/j.astropartphys.2012.02.004. arXiv: 1201.0018 [astro-ph.HE].

[84] Andreas Haungs, Heinigerd Rebel, and Markus Roth. “Energy spectrum and mass composition of high-energy cosmic rays”. In: *Reports on Progress in Physics* 66.7 (2003), pp. 1145–1206. DOI: 10.1088/0034-4885/66/7/202.

[85] W. D. Apel et al. “Ankle-like feature in the energy spectrum of light elements of cosmic rays observed with KASCADE-Grande”. In: *Phys. Rev. D* 87 (8 2013), p. 081101. DOI: 10.1103/PhysRevD.87.081101.

[86] Andreas Haungs. “Cosmic Rays from the Knee to the Ankle”. In: *Phys. Procedia* 61 (2015), pp. 425–434. DOI: 10.1016/j.phpro.2014.12.094. arXiv: 1504.01859 [astro-ph.HE].

[87] Esteban Roulet. “Large-scale anisotropies above 0.03 EeV measured by the Pierre Auger Observatory”. In: *PoS* ICRC2019 (2020), p. 408.

[88] The Tibet AS γ Collaboration. “Large-scale Cosmic Ray Anisotropy with Tibet air shower array”. In: *PoS* ICRC2019 (2020), p. 488.

[89] W. Gao and on behalf of the LHAASO Collaboration. “The large-scale anisotropy of cosmic rays observedwith the partial LHAASO-KM2A array”. In: *PoS* ICRC2019 (2020), p. 263.

[90] Y. Guo et al. “The Cosmic-ray Anisotropy Observed by YBJ-HAExperiment”. In: *PoS* ICRC2019 (2020), p. 354.

[91] P. K. Mohanty and the GRAPES-3 Collaboration. “Observation of cosmic ray anisotropy with GRAPES-3 Experiment”. In: *PoS* ICRC2019 (2020), p. 354.

[92] Chandra X ray: NASA/CXC/B.Gaensler et al; ROSAT X-ray: NASA/ROSAT/Asaoka & Aschenbach; Optical: DSS. https://chandra.harvard.edu/photo/2006/ic443/more.html.

[93] C. D. Dermer et al. “On the Physics Connecting Cosmic Rays and Gamma Rays: Towards Determining the Interstellar Cosmic Ray Spectrum”. In: *arXiv e-prints*, arXiv:1303.6482 (Mar. 2013), arXiv:1303.6482. arXiv: 1303.6482 [astro-ph.HE].

[94] W.B. Atwood et al. “The Large Area Telescope on the Fermi Gamma-ray Space Telescope Mission”. In: *Astrophys. J.* 697 (2009), pp. 1071–1102. DOI: 10.1088/0004-637X/697/2/1071. arXiv: 0902.1089 [astro-ph.IM].

[95] M. Ackermann et al. “Detection of the Characteristic Pion-Decay Signature in Supernova Remnants”. In: *Science* 339.6121 (2013), pp. 807–811. ISSN: 0036-8075. DOI: 10.1126/science.1231160.

[96] F. Reines. “Neutrino Interactions”. In: *Annual Review of Nuclear and Particle Science* 10 (Jan. 1960), pp. 1–26. DOI: 10.1146/annurev.ns.10.120160.000245.

[97] M.G. Aartsen et al. “The IceCube Neutrino Observatory: Instrumentation and Online Systems”. In: *JINST* 12.03 (2017), P03012. DOI: 10.1088/1748-0221/12/03/P03012. arXiv: 1612.05093 [astro-ph.IM].

[98] R. Abbasi et al. “The Design and Performance of IceCube DeepCore”. In: *Astropart. Phys.* 35 (2012), pp. 615–624. DOI: 10.1016/j.astropartphys.2012.01.004. arXiv: 1109.6096 [astro-ph.IM].

[99] A.U. Abeysekara et al. “All-Sky Measurement of the Anisotropy of Cosmic Rays at 10 TeV and Mapping of the Local Interstellar Magnetic Field”. In: *Astrophys. J.* 871.1 (2019), p. 96. DOI: 10.3847/1538-4357/aaf5cc. arXiv: 1812.05682 [astro-ph.HE].

[100] M.G. Aartsen et al. “Neutrino emission from the direction of the blazar TXS 0506+056 prior to the IceCube-170922A alert”. In: *Science* 361.6398 (2018), pp. 147–151. ISSN: 0036-8075. DOI: 10.1126/science.aat2890.

[101] Francis Halzen. “Neutrinos Associated with Cosmic Rays”. In: *Journal of Physics: Conference Series* 337 (2012), p. 012050. DOI: 10.1088/1742-6596/337/1/012050.

[102] Claire Guépin et al. “Ultra-high-energy cosmic rays and neutrinos from tidal disruptions by massive black holes (Corrigendum)”. In: *Astronomy & Astrophysics* 636, C3 (Apr. 2020), p. C3. DOI: 10.1051/0004-6361/201732392e.

[103] V. N. Zirakashvili and V. S. Ptuskin. “Supernova Remnants as Sources of Cosmic Rays and Nonthermal Emission”. In: *Physics of Atomic Nuclei* 82.6 (Feb. 2020), pp. 816–821. DOI: 10.1134/S1063778819660530.

[104] M. G. Aartsen et al. “Cosmic ray spectrum and composition from PeV to EeV using 3 years of data from IceTop and IceCube”. In: *Phys. Rev. D* 100.8, 082002 (Oct. 2019), p. 082002. DOI: 10.1103/PhysRevD.100.082002. arXiv: 1906.04317 [astro-ph.HE].

[105] Javier G. Gonzalez. “Measuring the Muon Content of Air Showers with IceTop”. In: *EPJ Web Conf.* 99 (2015), p. 06002. DOI: 10.1051/epjconf/20159906002. arXiv: 1501.03415 [astro-ph.HE].

[106] Frank G. Schröder. “Science Case of a Scintillator and Radio Surface Array at IceCube”. In: *PoS* ICRC2019 (2020), p. 418. DOI: 10.22323/1.358.0418. arXiv: 1908.11469 [astro-ph.HE].

[107] Samridha Kunwar et al. “The IceTop Scintillator Upgrade”. In: *PoS* ICRC2017 (2018), p. 401. DOI: 10.22323/1.301.0401.

[108] Markus Ahlers and Kohta Murase. “Probing the Galactic origin of the IceCube excess with gamma rays”. In: *Phys. Rev. D* 90.2, 023010 (July 2014), p. 023010. DOI: 10.1103/PhysRevD.90.023010. arXiv: 1309.4077 [astro-ph.HE].

[109] A. Horneffer et al. “Radio Detection of Cosmic Rays with Lopes”. In: *International Journal of Modern Physics A* 21 (Jan. 2006), pp. 168–181. DOI: 10.1142/S0217751X0603357X.

[110] P. A. Bezyazeekov et al. “Measurement of cosmic-ray air showers with the Tunka Radio Extension (Tunka-Rex)”. In: *Nuclear Instruments and Methods in Physics Research A* 802 (Dec. 2015), pp. 89–96. DOI: 10.1016/j.nima.2015.08.061. arXiv: 1509.08624 [astro-ph.IM].

[111] Tim Huege and Pierre Auger Collaboration. “Radio detection of cosmic rays with the Auger Engineering Radio Array”. In: European Physical Journal Web of Conferences 210, 05011 (Oct. 2019), p. 05011. DOI: 10.1051/epjconf/201921005011. arXiv: 1905.04986 [astro-ph.IM].

[112] A. Aab et al. “Observation of inclined EeV air showers with the radio detector of the Pierre Auger Observatory”. In: *J. Cosmol. Astropart. Phys.* 2018.10, 026 (Oct. 2018), p. 026. DOI: 10.1088/1475-7516/2018/10/026. arXiv: 1806.05386 [astro-ph.IM].

[113] Fiona Ellwanger. “Capabilities of the KIT/DESY scintillator station at the South Pole”. Bachelor Thesis. Karlsruhe Institute of Technology, 2019.

[114] D. G. Michael et al. "The Magnetized steel and scintillator calorimeters of the MINOS experiment". In: *Nucl. Instrum. Meth.* A596 (2008), pp. 190–228. DOI: `10.1016/j.nima.2008.08.003`. arXiv: `0805.3170 [physics.ins-det]`.

[115] Anna Pla-Dalmau. "Extruded plastic scintillator for the MINOS calorimeters". In: *Frascati Phys. Ser.* 21 (2001), pp. 513–522.

[116] Alexander Streich. "Scintillator Surface Detector for the Upgrade of the Pierre Auger Observatory". Master Thesis. Karlsruhe Institute of Technology, 2017.

[117] Marie Oehler. "Characterization of SiPMs for the Surface Array Enhancement of IceCube". Master Thesis. Karlsruhe Institute of Technology, 2018.

[118] T. Karg et al. "Introducing TAXI: a Transportable Array for eXtremely large area Instrumentation studies". In: *arXiv e-prints*, arXiv:1410.4685 (Oct. 2014), arXiv:1410.4685. arXiv: `1410.4685 [astro-ph.IM]`.

[119] M. Renschler. "First measurements with prototype radio antennas for the IceTop detector array". In: *36th International Cosmic Ray Conference (ICRC2019)*. Vol. 36. International Cosmic Ray Conference. July 2020, p. 401. arXiv: `1908.10565 [astro-ph.IM]`.

[120] Peter Streinmüller. "Development of Radio Front-End Electronics For a Prototype Radio Station at the South Pole". Master Thesis. Karlsruhe Institute of Technology, 2019.

[121] Marie Oehler. Private communication.

[122] Glenn F. Knoll. *Radiation detection and measurement, Third edition*. John Wiley &Sons, Inc., 2000.

[123] Igor Yashin et al. "Scintillation hodoscope for muon diagnostics". In: *31st International Cosmic Ray Conference, ICRC 2009* (Jan. 2009).

[124] Vladimir Lenok. Private communication.

[125] D. Heck et al. In: *Report FZKA 6019* (1998). URL: `https://publikationen.bibliothek.kit.edu/270043064`.

[126] Pierog T. Heck D. *Extensive Air Shower Simulation with CORSIKA: A User's Guide Version 7.7100*. 2019.

[127] Sam De Ridder and Tom Feusels. "Seasonal variation of the muon multiplicity in cosmic rays at South Pole". In: *Proceedings, 33rd International Cosmic Ray Conference (ICRC2013): Rio de Janeiro, Brazil, July 2-9, 2013*. 2013, p. 0763.

[128] Thomas K. Gaisser. *Cosmic Rays and Particle Physics*. Great Britain, Cambridge: Cambridge University Press, 1990.

[129] Stephan Meighen-Berger, Anatoli Fedynitch, and Matthias Huber. "EmCa – Electromagnetic-Cascades Simulation Package". In: (2019). arXiv: `1907.06924 [astro-ph.HE]`.

[130] W R Nelson, H Hirayama, and D W.O. Rogers. "EGS4 code system". In: (Dec. 1985).

[131] A. B. Migdal. "Bremsstrahlung and Pair Production in Condensed Media at High Energies". In: *Phys. Rev.* 103 (6 1956), pp. 1811–1820. DOI: `10.1103/PhysRev.103.1811`.

[132] Klein S.R. et al. *A Measurement of the LPM Effect*. SLAC-PUB-6378. 1993.

[133] A Ferrari et al. CERN-2005-10 (2005), INFN/TC_05/11, SLAC-R-77.

[134] T. T. Böhlen et al. “The FLUKA Code: Developments and Challenges for High Energy and Medical Applications”. In: *Nucl. Data Sheets* 120 (2014), pp. 211–214. DOI: 10.1016/j.nds.2014.07.049.

[135] Felix Riehn et al. “A new version of the event generator Sibyll”. In: *PoS* ICRC2015 (2016), p. 558. DOI: 10.22323/1.236.0558. arXiv: 1510.00568 [hep-ph].

[136] S. Agostinelli et al. “GEANT4: A Simulation toolkit”. In: *Nucl. Instrum. Meth.* A506 (2003), pp. 250–303. DOI: 10.1016/S0168-9002(03)01368-8.

[137] Geant4 Collaboration. *Guide For Physics Lists Release 10.5*. Mar. 2019.

[138] R. Abbasi et al. “IceTop: The surface component of IceCube”. In: *Nucl. Instrum. Meth.* A700 (2013), pp. 188–220. DOI: 10.1016/j.nima.2012.10.067. arXiv: 1207.6326 [astro-ph.IM].

[139] F. Kislat et al. “IceTop tank simulation using g4-tankresponse”. Internal note. July 2012.

[140] Gabriele Cosmo, CERNIT. *Detector Description – basic concepts*. URL: {https://geant4.web.cern.ch/sites/geant4.web.cern.ch/files/geant4/collaboration/workshops/users2002/talks/lectures/geobasics.pdf} (visited on 03/15/2020).

[141] Xavier Bertou et al. “Calibration of the surface array of the Pierre Auger Observatory”. In: *Nucl. Instrum. Meth.* A568 (2006), pp. 839–846. DOI: 10.1016/j.nima.2006.07.066.

[142] Arne Van Overloop. “Simulation of IceTop VEM calibration and the dependency on the snow layer”. In: *Proceedings, 32nd International Cosmic Ray Conference (ICRC 2011): Beijing, China, August 11-18, 2011*. Vol. 1. 2011, pp. 97–101. DOI: 10.7529/ICRC2011/V01/0899.

[143] IceCube Collaboration. Private communication.

[144] A. Pla-Dalmau, A. D. Bross, and V. V. Rykalin. “Extruding plastic scintillator at Fermilab”. In: *2003 IEEE Nuclear Science Symposium. Conference Record (IEEE Cat. No.03CH37515)*. Vol. 1. 2003, 102–104 Vol.1. DOI: 10.1109/NSSMIC.2003.1352007.

[145] G. Ros et al. “On the design of experiments based on plastic scintillators using Geant4 simulations”. In: (2018). [Radiat. Phys. Chem.153,140(2018)]. DOI: 10.1016/j.radphyschem.2018.09.021. arXiv: 1804.08975 [astro-ph.IM].

[146] Kim Youngju et al. “A TiO_2-Coated Reflective Layer Enhances the Sensitivity of a CsI:Tl Scintillator for X-ray Imaging Sensors”. In: *J. Opt. Soc. Korea* 18.3 (2014), pp. 256–260. URL: http://www.osapublishing.org/josk/abstract.cfm?URI=josk-18-3-256.

[147] J. B. Birks. “Scintillations from Organic Crystals: Specific Fluorescence and Relative Response to Different Radiations”. In: *Proc. Phys. Soc.* A64 (1951), pp. 874–877. DOI: 10.1088/0370-1298/64/10/303.

[148] Erik Dietz-Laursonn. “Detailed Studies of Light Transport in Optical Components of Particle Detectors”. Dissertation. RWTH Aachen University, 2016.

[149] D. Beznosko et al. “FNAL-NICADD extruded scintillator”. In: (2005).

[150] Joaquin Masias et al. “Using a portable muon detector for radioactive source measurements and identification”. In: (2019). DOI: 10.1016/j.nima.2019.162588. arXiv: 1903.04562 [physics.ins-det].

[151] Matthias Plum. Private communication.

[152] Kuraray. *Wavelength shifting fibers Y11*. 2019. URL: http://kuraraypsf.jp/psf/ws.html (visited on 11/20/2019).

[153] E. Dietz-Laursonn et al. "GODDeSS: a Geant4 extension for easy modelling of optical detector components". In: *JINST* 12.04 (2017), P04026–P04026. DOI: 10.1088/1748-0221/12/04/p04026.

[154] Eljen Technology. *Optical Cement EJ-500*. 2019. URL: {https://eljentechnology.com/products/accessories/ej-500} (visited on 11/22/2019).

[155] Agnieszka Leszczyńska and Matthias Plum. "Simulation and Reconstruction Study of a Future Surface Scintillator Array at the IceCube Neutrino Observatory". In: *PoS* ICRC2019 (2020), p. 332. DOI: 10.22323/1.358.0332. arXiv: 1909.02258 [astro-ph.IM].

[156] Anna Pla-Dalmau. Private communication.

[157] P. Doll et al. "Muon tracking detector for the air shower experiment KASCADE". In: *Nucl. Instrum. Meth.* A488 (2002), pp. 517–535. DOI: 10.1016/S0168-9002(02)00560-0.

[158] Darko Veberic. Private communication.

[159] J.E. Moyal. "XXX. Theory of ionization fluctuations". In: *The London, Edinburgh, and Dublin Philosophical Magazine and Journal of Science* 46.374 (1955), pp. 263–280. DOI: 10.1080/14786440308521076.

[160] Tim Niggemann et al. "G4SiPM: A novel silicon photomultiplier simulation package for Geant4". In: *Nucl. Instrum. Meth.* A787 (2015), pp. 344–347. DOI: 10.1016/j.nima.2015.01.067.

[161] Chris Wendt. Private communication.

[162] Matt Kauer. *muDAQ/scint South Pole Update*. IceCube Fall meeting. Oct. 2018.

[163] Ramesh Koirala and Thomas K. Gaisser. "Low Energy Cosmic Ray Spectrum from 250 TeV to 10 PeV using IceTop". In: *PoS* ICRC2019 (2020), p. 318. DOI: 10.22323/1.358.0318. arXiv: 1908.07143 [astro-ph.HE].

[164] Aswathi Balagopal V. "A Quest for PeVatrons Employing Radio Detection of Extensive Air Showers". PhD thesis. Karlsruher Institut für Technologie (KIT), 2019. 129 pp. DOI: 10.5445/IR/1000091377.

[165] Communication with IceTop Enhancement Working Group.

[166] PyIK The Python Instrument Kit. https://github.com/HDembinski/pyik.

[167] Edwin B. Wilson. "Probable Inference, the Law of Succession, and Statistical Inference". In: *Journal of the American Statistical Association* 22.158 (1927), pp. 209–212. DOI: 10.1080/01621459.1927.10502953.

[168] W. D. Apel et al. "Comparison of measured and simulated lateral distributions for electrons and muons with KASCADE". In: *Astropart. Phys.* 24 (2006), pp. 467–483. DOI: 10.1016/j.astropartphys.2005.10.001. arXiv: astro-ph/0510810 [astro-ph].

[169] T Teshima et al. "Properties of 10^9-10^{10} GeV extensive air showers at core distances between 100 and 3000 m". In: *Journal of Physics G: Nuclear Physics* 12.10 (1986), pp. 1097–1113. DOI: 10.1088/0305-4616/12/10/017.

[170] M Nagano et al. “Energy spectrum of primary cosmic rays above 1017.0eV determined from extensive air shower experiments at Akeno”. In: *Journal of Physics G: Nuclear and Particle Physics* 18.2 (1992), pp. 423–442. DOI: 10.1088/0954-3899/18/2/022.

[171] M. G. Aartsen et al. “Measurement of the cosmic ray energy spectrum with IceTop-73”. In: *Phys. Rev.* D88.4 (2013), p. 042004. DOI: 10.1103/PhysRevD.88.042004. arXiv: 1307.3795 [astro-ph.HE].

[172] Jean-Noel Capdevielle and Fabrice Cohen. “The relation between the lateral profile of giant extensive air showers and the age parameter”. In: *J. Phys.* G31 (2005), pp. 507–524. DOI: 10.1088/0954-3899/31/5/018.

[173] M. Nagano et al. “Comparison of AGASA data with CORSIKA simulation”. In: *Astroparticle Physics* 13.4 (July 2000), pp. 277–294. DOI: 10.1016/S0927-6505(99)00128-0. arXiv: astro-ph/9912222 [astro-ph].

[174] A.A. Lagutin et al. “Electron lateral distribution in air showers: Scaling formalism and its implications”. In: *J. Phys. G* 28 (2002), pp. 1259–1274. DOI: 10.1088/0954-3899/28/6/309.

[175] S Klepser. “Reconstruction of Extensive Air Showers and Measurement of the Cosmic Ray Energy Spectrum in the Range of 1-80PeV at the South Pole”. PhD Thesis. Humboldt-Universität zu Berlin, 2008. DOI: 10.18452/15790.

[176] Daniel Foreman-Mackey et al. “emcee: The MCMC Hammer”. In: *Publ. Astron. Soc. Pac.* 125 (2013), pp. 306–312. DOI: 10.1086/670067. arXiv: 1202.3665 [astro-ph.IM].

[177] Talianna Christina Schmidt. “Measurement of the Flux of Ultra High Energy Cosmic Rays using very inclined Extensive Air Showers measured at the Pierre Auger Observatory”. PhD Thesis. Karlsruhe Institute of Technology, 2010. DOI: 10.5445/IR/1000017923.

[178] M. Ave et al. “The accuracy of signal measurement with the water Cherenkov detectors of the Pierre Auger Observatory”. In: *Nucl. Instrum. Meth. A* 578 (2007), pp. 180–184. DOI: 10.1016/j.nima.2007.05.150.

[179] F. Kislat. “Study of charge and time fluctuations of signals in the IceTop detector”. Diplomarbeit. Humboldt-Universität zu Berlin, 2007.

[180] David Schmidt. “Sensitivity of AugerPrime to the masses of ultra-high-energy cosmic rays”. PhD Thesis. Karlsruhe Institute of Technology, 2019.

[181] Timo Karg. Private communication.

[182] Javier Gonzalez. “Studying Cosmic Ray Composition with IceTop using Muon and Electromagnetic Lateral Distributions”. In: *PoS* ICRC2015 (2016), p. 338. DOI: 10.22323/1.236.0338.

[183] Xinhua Bai and Emily Dvorak. “A Three-dimensional Reconstruction of Cosmic Ray Events in IceCube”. In: *PoS* ICRC2019 (2020), p. 244.

[184] Johannes J. Möller et al. “Compositional optimization of hard-magnetic phases with machine-learning models”. In: *Acta Materialia* 153 (2018), pp. 53 –61. ISSN: 1359-6454. DOI: https://doi.org/10.1016/j.actamat.2018.03.051.

[185] A. M. Hillas et al. “Measurement of Primary Energy of Air Showers in the Presence of Fluctuations.” In: *12th International Cosmic Ray Conference (ICRC12), Volume 3*. Vol. 3. International Cosmic Ray Conference. Jan. 1971, p. 1001.

[186] Fabian Kislat. “Measurement of the energy spectrum of cosmic rays with the 26 station configuration of the IceTop detector”. PhD thesis. Humboldt-Universität zu Berlin, Mathematisch-Naturwissenschaftliche Fakultät I, 2012. DOI: 10.18452/16443.

[187] Bakhtiyar Ruzybayev. “Measurement of Cosmic Ray Energy Spectrum with IceTop”. PhD thesis. University of Delaware, 2012.

[188] K. Rawlins. “Cosmic ray spectrum and composition from three years of IceTop and IceCube”. In: *J. Phys. Conf. Ser.* 718.5 (2016), p. 052033. DOI: 10.1088/1742-6596/718/5/052033.

[189] Ewa M. Holt, Schröder Frank G., and Andreas Haungs. “Enhancing the cosmic-ray mass sensitivity of air-shower arrays by combining radio and muon detectors”. In: *Eur. Phys. J.* C79.5 (2019), p. 371. DOI: 10.1140/epjc/s10052-019-6859-4. arXiv: 1905.01409 [astro-ph.HE].

[190] A. Tapia et al. “The lateral shower age parameter as a estimator of chemical composition”. In: *33rd International Cosmic Ray Conference*. Sept. 2013, p. 0251. arXiv: 1309.3536 [astro-ph.HE].

[191] Alexander Aab et al. “Prototype muon detectors for the AMIGA component of the Pierre Auger Observatory”. In: *JINST* 11.02 (2016), P02012. DOI: 10.1088/1748-0221/11/02/P02012. arXiv: 1605.01625 [physics.ins-det].

[192] P. Doll et al. “Muon tracking detector for the air shower experiment KASCADE”. In: *Nucl. Instrum. Meth. A* 488 (2002), pp. 517–535. DOI: 10.1016/S0168-9002(02)00560-0.

[193] Tom Feusels. “Measurement of cosmic ray composition and energy spectrum between 1 PeV and 1 EeV with IceTop and IceCube”. PhD Thesis. Universitet Gent, 2014.

[194] Sam De Ridder. “Sensitivity of IceCube Cosmic Ray measurements to the hadronic interaction models”. PhD Thesis. Ghent University, 2018. URL: https://biblio.ugent.be/publication/8609789/file/8609790.

[195] Ronald Aylmer Fisher. “The use of multiple measurements in taxonomic problems”. In: *Annals Eugen.* 7 (1936), pp. 179–188. DOI: 10.1111/j.1469-1809.1936.tb02137.x.

[196] F. Pedregosa et al. “Scikit-learn: Machine Learning in Python”. In: *Journal of Machine Learning Research* 12 (2011), pp. 2825–2830.

[197] Alan Coleman. Private communication.

[198] N. M. Budnev et al. “The primary cosmic-ray energy spectrum measured with the Tunka-133 array”. In: *Astroparticle Physics* 117, 102406 (Jan. 2020), p. 102406. DOI: 10.1016/j.astropartphys.2019.102406.

[199] A. Coleman and for the Pierre Auger Collaboration. “Measurement of the Cosmic Ray Flux near the Second Knee with the Pierre Auger Observatory”. In: *PoS* ICRC2019 (2020), p. 225.

[200] R. U. Abbasi et al. “The Cosmic Ray Energy Spectrum between 2 PeV and 2 EeV Observed with the TALE Detector in Monocular Mode”. In: *The Astrophysical Journal* 865.1, 74 (Sept. 2018), p. 74. DOI: 10.3847/1538-4357/aada05. arXiv: 1803.01288 [astro-ph.HE].

[201] G. Di Sciascio. “The LHAASO experiment: from Gamma-Ray Astronomy to Cosmic Rays”. In: *Nucl. Part. Phys. Proc.* 279-281 (2016). Ed. by Gabriella Cataldi, Ivan De Mitri, and Daniele Martello, pp. 166–173. DOI: `10.1016/j.nuclphysbps.2016.10.024`. arXiv: `1602.07600 [astro-ph.HE]`.

ACKNOWLEDGEMENT

It has always been clear to me that any effort made by human beings has never been made by individuals. Behind every success are other, often invisible faces. With this little page I would like to shed at least some light on all those without whom this work would never have been done.

Therefore I express my large gratitude to ...
... Prof. Ralph Engel and Prof. Florian Bernlochner — referees of this work, for their support and expertise insight into this work ...
... Andreas Haungs — supervisor of this work, for his constant support and input, answering my questions and doubts (even late in the evening and early in the morning), encouragement to pursue my ideas, never give up and believe in my scientific skills. Clearly this would never happen without his understanding. For his laugh – it has always made me feel comfortable that the situation is not as bad as I think it is. Thank you for everything ...
... Prof. Paweł Możejko — supervisor of my bachelor and master thesis, for his support in these first years of my scientific path and creating my scientific curiosity ...
... Prof. Bogusław Zwięgliński — supervisor of my summer internship, his words about physics convinced me that this is the right way to proceed even if not the easiest one...
... Javier Gonzalez and Timo Karg — for their inestimable introduction into the world of the IceCube software ...
... Jürgen Oehlschläger — for his enormous help in the production of CORSIKA simulations, storage management, ingenuity in quality assurance of the files and for his every-day coffee ...
... Sabine Bucher — for all administrative work, remembering about things I should remember about making my life so much easier, especially in difficult moments ...
... Doris Wochele — for her guidance in my first steps in the computing world, understanding and rescuing from lack of computation nodes, for our afternoon's discussions and for her attitude to life ...
... Matthias — for his help with Geant4 issues and great work in scintillator simulations ...
... Alan — for his great help in improving my work, co-operation in the RockBottom project and for his extensive help in improving my English ...
... Dennis — for his comprehensive answers to questions related to cosmic rays and the IceCube software, for his unique character ...
... Vova — for his support and patience every day, invaluable help (from technical to scientific), input and discussions in many stages of this work, in particular in these last months and weeks...
... Aswathi — for being my first guide into IKP, for her input and every-day support ...
... Marie — for all her warm support and conversations about our ups and downs, you have been a light to me ...
... Fiona — for being an amazing student, inspiring me to be a better advisor ...
... members of IceCube@KIT, CosmicRay@KIT, IceTop group and IceCube collaboration — for fruitful discussions and meetings and pushing this field of research further ...

The warmest thanks go to my family …
… my parents — Urszula and Stanisław — you were always source of my strength, my courage and you gave me everything I could ever ask for, you believe in my the most when I lose all hope …
… my brother — Jakub – you are my little star on the sky, you smile and care makes me happy every day, your support in this difficult time was precious …
… Dorota and Henryk — my aunt and uncle, you made my life in Germany so much easier, I could have always counted on your support …
… Maciek — clearly you are like my family, my best friend for years, thank you for being there for me …
… all my family members who encouraged me to pursue this work and who prayed for me so strong that I could feel it every day.

Thank you

ERKLÄRUNG

Eggenstein-Leopoldshafen, den 10.05.2020

Erklärung der selbständigen Anfertigung meiner Dissertationsschrift

Hiermit versichere ich, dass ich die Dissertationsschrift mit dem Titel

Potential of the IceTop Enhancement with a Scintillation Detector Array

selbständig und ohne unerlaubte fremde Hilfe verfasst habe. Dabei habe ich keine anderen, als die von mir angegebenen Hilfsmittel benutzt.

Agnieszka Stanisława Leszczyńska